

# **Ribonucleoprotein Structure in Pathogenic Orthobunyaviruses**

Francis Raymond Hopkins

Submitted in accordance with the requirements for the degree of Doctor of Philosophy

The University of Leeds

The Astbury Centre for Molecular Biology

April 2020

The candidate confirms that the work submitted is his own and that appropriate credit has been given where reference has been made to the work of others.

This copy has been supplied on the understanding that it is copyright material, and that no quotation from the thesis may be published without consent.

©The University of Leeds and Francis Raymond Hopkins

## Acknowledgements

Firstly, I would like to thank my supervisors John and Ed for all of their help and guidance over the course of the PhD. To John in particular, your enthusiasm for these viruses always kept things going, even when getting a structure of such bendy filaments seemed like a lost cause to me. I would also like to give enormous thanks to Juan, who became a sort of adopted supervisor, and who is largely responsible for how well the EM turned out in the end.

Thank you to current and former members of the Barr and Edwards Groups for the companionship and help in the lab for the last four years, and to everyone else in Garstang 8.61 and 8.53. Thanks as well to ABSL and all of its staff for help with making grids and using the microscopes, and to the BBSRC for funding the project.

Thank you to Dr Peter Sun at NIH for offering me an internship in his lab and the opportunity to live and work in the USA for three months, and to everyone who made it such an amazing time; particularly Malcolm, Matt, Austin and Caroline.

To the friends I've made in the last few years, thank you for all of the good times. Huge amounts of love go to the DTMFs; it was nice always having someone to drink beer with, regardless of time or location... Thank you particularly to Jack for two years of unrelenting domestic bliss, to Britt for the adventures in America, and to Georgia, not least because if I didn't mention you here I'd never hear the end of it.

To Janne, meeting you was honestly the best part of this whole thing. Thank you for everything ♥.

To my mum and sisters, thank you for all the love and support over the years.

Finally, to Dad. I know how proud you were when I started this journey, so this thesis is dedicated to you. I only wish you were still here to read it.

## Abstract

The orthobunyavirus genus within the *Bunyavirales* order contains many pathogens of humans and livestock. Their genome consists of three segments of negative-sense, single-stranded RNA and these are encapsidated with polymers of nucleocapsid protein (NP) which binds RNA in a sequence-independent manner to form ribonucleoproteins (RNPs). Formation of RNPs protects the viral genome from the host immune system and has roles in transcription, viral RNA replication and the correct packaging of segments into new virions. Thus, the RNP is an attractive target for the development of antivirals, which is of particular importance as no specific therapies exist for any of the human pathogens of the genus.

Within the field there are currently two different hypotheses on the overall structure of the RNP filament, and establishing a definitive model has been hampered by the extreme flexibility and heterogeneity of the filaments. This project aimed to accurately describe the architecture of the orthobunyavirus RNP and produce a model which illuminates its gross structural features, and mechanisms of assembly and RNA binding.

Infectious Bunyamwera virus (BUNV) was propagated and purified by ultracentrifugation, allowing the extraction and purification of RNPs from virions, which were then visualized by negative stain electron microscopy (EM). An ensemble of microscopy methods encompassing negative stain EM, single particle cryo-EM and cryo-electron tomography was employed to overcome the extreme heterogeneity of the filaments, and to produce several models of the RNP that permitted the fitting of NP crystal structures and clearly exhibited a helical architecture. This structural information will aid in the development of small molecules which inhibit formation of the orthobunyavirus RNP and which could be investigated further for their therapeutic potential.

# Contents

<b>Acknowledgements.....</b>	<b>ii</b>
<b>Abstract.....</b>	<b>iii</b>
<b>Contents.....</b>	<b>iv</b>
<b>List of figures.....</b>	<b>ix</b>
<b>List of tables.....</b>	<b>xi</b>
<b>Abbreviations.....</b>	<b>xii</b>
<b>1 Introduction.....</b>	<b>1</b>
1.1 Negative strand RNA viruses and the <i>Bunyavirales</i> order.....	1
1.2 <i>Bunyavirales</i> and disease.....	3
1.3 Bunyamwera virus of the <i>Orthobunyavirus</i> genus, <i>Peribunyaviridae</i> family.....	3
1.4 Reassortment as a mechanism of orthobunyavirus emergence.....	6
1.5 Orthobunyavirus vectors.....	7
1.6 General structural characteristics of the orthobunyaviruses.....	8
1.7 Orthobunyavirus segment coding strategy.....	10
1.8 Orthobunyavirus multiplication cycle.....	10
1.8.1 Overview.....	10
1.8.2 Cell entry.....	12
1.8.3 mRNA transcription.....	13
1.8.4 Genome replication.....	16
1.8.5 Viral factories.....	18
1.9 Structural aspects of viral proteins.....	19
1.9.1 RNA-dependent RNA polymerase (RdRp).....	19

1.9.2	Glycoproteins.....	23
1.9.3	Nucleocapsid protein (NP).....	24
1.10	Other viral NP structures.....	30
1.10.1	Bunyavirales.....	30
1.10.2	Influenza virus and mononegavirales NP.....	35
1.11	Oligomerisation of orthobunyaviral NP.....	35
1.12	Ribonucleoproteins (RNPs).....	37
1.12.1	Orthobunyavirus RNP structure.....	37
1.12.2	Other bunyaviral RNPs.....	40
1.12.3	Non-bunyaviral RNPs.....	43
1.13	Transmission electron microscopy (TEM).....	44
1.13.1	Principles of TEM.....	44
1.13.2	Electron detection.....	46
1.13.3	Negative staining.....	47
1.13.4	Cryo-EM.....	48
1.13.5	Cryo-electron tomography (Cryo-ET).....	49
1.13.6	Tilt series.....	50
1.13.7	Tomogram reconstruction and sub-tomogram averaging (STA).....	50
1.14	Aims of the project.....	53
<b>2</b>	<b>Materials and methods.....</b>	<b>54</b>
2.1	Tissue culture and virological techniques.....	54
2.1.1	Cell and virus stocks.....	54
2.1.2	Virus propagation.....	54
2.1.3	Virus purification.....	55

2.1.4	Plaque assay.....	56
2.2	RNP purification.....	57
2.3	Protein analysis.....	58
2.3.1	SDS-PAGE.....	58
2.3.2	Coomassie stain.....	59
2.3.3	Western blot.....	59
2.4	Reconstituting RNPs.....	60
2.4.1	Recombinant protein expression.....	60
2.4.2	Synthesis of BUNV genomic RNA.....	61
2.5	Negative stain EM.....	62
2.5.1	Grid preparation and image acquisition.....	62
2.5.2	Image processing.....	63
2.6	Cryo-EM.....	65
2.6.1	Grid preparation.....	65
2.6.2	Data collection.....	65
2.6.4	Analysis of 3D models.....	66
<b>3</b>	<b>Isolation and initial characterisation of the architecture of BUNV RNPs.....</b>	<b>67</b>
3.1	Chapter introduction .....	67
3.2	BUNV RNP purification .....	71
3.2.1	Optimising BUNV virion purification .....	72
3.2.2	Releasing RNPs from BUNV virions.....	76
3.2.2.1	Sucrose.....	76
3.2.2.2	Detergent.....	77
3.2.2.3	Freeze-thawing.....	78

3.2.3	Initial cryo-EM .....	80
3.2.4	RNP purification by continuous density gradient ultracentrifugation.....	82
3.2.5	Optimum buffer conditions for EM analysis of RNPs.....	83
3.2.6	Optimising concentration of RNPs.....	86
3.3	Analysis of negatively stained BUNV RNPs.....	88
3.3.1	Class averages of RNP filaments.....	88
3.3.2	Filament characteristics.....	91
3.3.3	Class averages of bends within RNP filaments.....	93
3.3.4	Class averages of a potential viral polymerase.....	94
3.3.5	Heating RNPs alters their conformation.....	95
3.4	Recombinant RNPs.....	97
3.5	Discussion.....	99
<b>4</b>	<b>Determining a three dimensional model of highly flexible BUNV RNPs.....</b>	<b>106</b>
4.1	Chapter introduction.....	106
4.2	Initial 3D analysis of negative stain data.....	109
4.3	Cryo-ET of BUNV RNPs.....	111
4.3.1	Cryo-ET tilt series acquisition.....	111
4.3.2	Sub-tomogram averaging (STA).....	114
4.4	3D model of BUNV RNPs from negative stain data.....	117
4.4.1	3D analysis of negative stain data with a reference from cryo-ET.....	117
4.4.2	Helical symmetry.....	120
4.5	Cryo-EM of BUNV RNPs.....	127

4.5.1	Cryo-EM data collection.....	127
4.5.2	3D analysis of cryo-EM data.....	129
4.5.3	Cryo-EM with phase plate.....	131
4.6	Discussion.....	135
4.6.1	Strategies for EM analysis of highly flexible filaments .....	135
4.6.2	Longitudinal NP interactions to stabilise the RNP helix.....	137
4.6.3	RNA binding in the context of a helical RNP.....	139
4.6.4	Future directions for cryo-EM analysis of orthobunyavirus RNPs.....	140
4.6.5	Insights from phase plate data acquisition.....	140
<b>5</b>	<b>Concluding remarks .....</b>	<b>144</b>
<b>6</b>	<b>References .....</b>	<b>148</b>

## List of figures

- 1.1 Orthobunyavirus virion schematic
- 1.2 Orthobunyavirus replication cycle
- 1.3 Bunyavirus replication and transcription
- 1.4 Orthobunyavirus genome replication schematic
- 1.5 LACV polymerase crystal structure
- 1.6 Bunyaviral glycoprotein structures
- 1.7 Orthobunyavirus NP structures
- 1.8 Non-orthobunyavirus NP structures
- 1.9 Oligomeric states of orthobunyavirus NP
- 1.10 Orthobunyavirus RNPs
- 1.11 Non-orthobunyavirus viral RNPs
- 1.12 Schematic of a TEM
- 1.13 The missing wedge problem
- 1.14 Tomogram reconstruction and STA
  
- 2.1 EM data processing work flow
  
- 3.1 Proposed models of NP organisation within orthobunyavirus RNPs
- 3.2 BUNV purification by PEG precipitation
- 3.3 BUNV purification by sucrose cushion
- 3.4 Lysing BUNV virions with sucrose
- 3.5 Lysing BUNV virions with detergent
- 3.6 Lysing BUNV virions by freeze-thawing

- 3.7 Initial cryo-EM
- 3.8 RNP purification by density gradient ultracentrifugation
- 3.9 Effects of buffer condition on BUNV RNP conformation
- 3.10 Optimising RNP concentration
- 3.11 Autopicking of BUNV RNPs
- 3.12 2D classification of BUNV RNPs
- 3.13 Initial characterisation of BUNV RNPs
- 3.14 2D classification of BUNV RNP corners
- 3.15 2D classification of large, unknown particles
- 3.16 Effects of heating on BUNV RNPs
- 3.17 Reconstituting RNPs from recombinant NP
- 3.18 Polymerases of negative RNA viruses
  
- 4.1 Structures of flexible protein filaments determined by cryo-EM
- 4.2 Initial 3D analysis of negatively stained RNPs
- 4.3 Raw micrographs from within tilt series
- 4.4 Reconstructed tomograms of purified BUNV RNPs
- 4.5 Placing model points for STA
- 4.6 STA of BUNV RNPs
- 4.7 First 3D classification of negative stain data
- 4.8 Second 3D classification of negative stain data
- 4.9 3D refinement of negatively stained RNPs
- 4.10 Helical reconstruction of BUNV RNPs from negative stain data
- 4.11 Testing a range of parameters for helical reconstruction
- 4.12 Ideal helices

- 4.13 A helical model of BUNV RNPs
  - 4.14 2D cryo-EM of BUNV RNPs
  - 4.15 3D analysis of BUNV RNP cryo-EM data
  - 4.16 2D analysis of BUNV RNP phase plate data
  - 4.17 Classification of RNP particles with a cylindrical reference
  - 4.18 3D analysis of BUNV RNP phase plate data and fitting of crystal structures
  - 4.19 Longitudinal NP interactions in the BUNV RNP
- 
- 5.1 3D structural data on BUNV RNPs

## List of tables

- 1 Bunyavirales taxonomy

## Abbreviations

AINV	Aino virus
AKAV	Akabane virus
BaMV	Bamboo mosaic virus
BATV	Batai virus
BUEV	Buenaventura virus
BUNV	Bunyamwera virus
CCD	Charge coupled device
CCHFV	Crimean-Congo hemorrhagic fever virus
CDC	Centers for Disease Control and Prevention
cRNA	complementary RNA (complementary to viral genome)
Cryo-EM	Cryo-electron microscopy
Cryo-ET	Cryo-electron tomography
CVV	Cache Valley virus
DED	Direct electron detector
DQE	Detective quantum efficiency
EFSA	European Food Safety Authority
eIF4G	Eukaryotic initiation factor 4G
EMDB	Electron Microscopy Data Bank
GPC	Glycoprotein precursor
GRAV	Granada virus
HAZV	Hazara virus
HTNV	Hantaan virus
IAV	Influenza A virus
IBV	Influenza B virus
ICTV	International Committee on the Taxonomy of Viruses
ICV	Influenza C virus
IDV	Influenza D virus
IFN	Interferon
INGV	Ingwavuma virus
INKV	Inkoo virus

JCV	Jamestown Canyon virus
LACV	La Crosse virus
LASV	Lassa virus
LCMV	Lymphocytic choriomeningitis virus
LEAV	Leanyer virus
MACV	Machupo virus
MAPS	Monolithic active pixel sensor
mRNA	Messenger RNA
MS	Mass spectrometry
NMR	Nuclear magnetic resonance
NP	Nucleocapsid protein
NRIV	Ngari virus
NSm	Non-structural medium
NSs	Non-structural small
NTR	Non-translated region (interchangeable with UTR)
ORF	Open reading frame
OROV	Oropouche virus
PABP	poly(A)-binding protein
PDB	Protein Data Bank
PepMV	Pepino mosaic virus
PKR	Protein kinase R
RdRp	RNA-dependent RNA polymerase
RMSD	Root mean square deviation
RNP	Ribonucleoprotein
RSV	Respiratory syncytial virus
RVFV	Rift valley fever virus
SATV	Sathuperi virus
SBV	Schmallenberg virus
SDS-PAGE	Sodium dodecyl sulfate polyacrylamide gel electrophoresis
SFTSV	Severe fever with thrombocytopenia syndrome virus (now renamed Huaiyangshan banyangvirus)
SHAV	Shamonda virus
SIMV	Simbu virus

SNR	Signal-to-noise ratio
SNV	Sin Nombre virus
SPA	Single particle analysis
SSHV	Snowshoe hare virus
STA	Sub-tomogram averaging
TAHV	Tahyna virus
TBK1	Tank binding kinase 1
TEM	Transmission electron microscope/microscopy
TMV	Tobacco mosaic virus
TOSV	Toscana virus
UTR	Untranslated region (interchangeable with NTR)
vRNA	Viral RNA (viral genomic RNA)
VSV	Vesicular stomatitis virus

# Chapter 1

## Introduction

### 1.1 Negative strand RNA viruses and the *Bunyvirales* order

All negative sense single stranded RNA viruses possess several distinctive characteristics including a protein-enwrapped genome known as a ribonucleoprotein (RNP), and a virion-associated polymerase that transcribes this RNP into coding sense mRNAs upon entry into new cells. Negative-sense single-stranded RNA viruses are the fifth of seven groups defined by the Baltimore virus classification system, which categorises viruses based on the nucleic acid composition of their genome, and their strategy of gene expression (Baltimore, 1971). Using the alternative virus classification system adopted by the International Committee on the Taxonomy of Viruses (ICTV) (Abudurexiti et al., 2019), negative-sense single-stranded RNA viruses form a single phylum, the *Negarnaviricota*. Within this, the *Polyploviricotina* subphylum contains those viruses which encode their genomes on multiple segments of RNA. The polyploviricotina are divided into two monotypic classes; the *Insthoviricetes* class contains those viruses with six to eight genome segments such as the important pathogens of the influenza genera. The *Ellioviricetes* class contains the *Bunyvirales* order of viruses, which have between two and eight genome segments. Members of the *Bunyvirales* are found across the globe, with viruses isolated from as far north as the Seward Peninsula of Alaska (Ballinger et al., 2014) and as far south as Macquarie Island, approximately 800 miles north of the

Antarctic continent (Major et al., 2009). Recent metagenomics analysis has dramatically increased the number of named isolates that belong to this group and, as a consequence, the ICTV has recently expanded the taxonomic divisions within the order. The *Bunyvirales* order currently includes around 500 named isolates within almost 300 species, making this one of the largest taxonomic groupings in existence. The order is divided into a total of 12 families entirely on the basis of genetic relatedness, with five of these, namely the *Arenaviridae*, *Hantaviridae*, *Nairoviridae*, *Peribunyaviridae* and *Phenuiviridae* families, containing serious pathogens of humans and other animals. However, it is clear that this virus family tree is far from complete and, given the pace of new virus identification which is being driven by metagenomics (Wolf, Y. I. et al., 2018), this classification scheme should be considered to be in a state of flux, and future changes are certain.

- Family:** *Arenaviridae*
- Family:** *Cruliviridae*
- Family:** *Fimoviridae*
- Family:** *Hantaviridae*
- Family:** *Leishbuviridae*
- Family:** *Myoviridae*
- Family:** *Nairoviridae*
- Family:** *Peribunyaviridae*
  - Genus:** *Herbevirus*
  - Genus:** *Orthobunyavirus*
  - Genus:** *Pacuvirus*
  - Genus:** *Shangavirus*
- Family:** *Phasmaviridae*
- Family:** *Phenuiviridae*
- Family:** *Tospoviridae*
- Family:** *Wupedeviridae*

**Table 1:** *Bunyvirales* taxonomy. The 12 families which constitute the *Bunyvirales* order, and the four genera which constitute the *Peribunyaviridae* family.

## 1.2 Bunyaviruses and disease

As described above, five families within the *Bunyavirales* order are the causative agents of disease in animals and humans, and in many cases the associated diseases are of the utmost severity. Fully one third of all the hazard group 4 viruses are *Bunyavirales* members (Health and Safety Executive, 2013) capable of causing haemorrhagic fevers for which no preventative or therapeutic strategies are available. These include the arenavirus, Lassa virus (LASV), as well as the nairovirus, Crimean-Congo haemorrhagic fever virus (CCHFV). Many *Bunyavirales* members are also hazard group 3 pathogens, associated with fatal human disease such as lymphocytic choriomeningitis virus (LCMV) and the hantavirus, Hantaan virus (HTNV). A number of serious animal pathogens also exist within the order such as the phenuivirus, Rift Valley fever virus (RVFV) and the peribunyavirus, Schmollenberg virus (SBV), which can affect commercial livestock. Together with the commercial crop-infecting members of the *Tospoviridae* family, these viruses can cause significant economic impacts.

## 1.3 Bunyamwera virus of the *Orthobunyavirus* genus, *Peribunyaviridae* family

The *Peribunyaviridae* family contains four genera, namely Herbevirus, Orthobunyavirus, Pacuvirus and Shangavirus. The largest of these by some margin is the orthobunyavirus, genus with around 90 named species that are in turn divided into twenty different serogroups based on their serologic relatedness of both complement fixing antibodies and neutralizing antibodies. Serological relatedness can vary within a group, such that an isolate may be more related to one serogroup or another, depending on the assay used, and this issue stems from the ability of segmented viruses to reassort, described in section 1.4. orthobunyaviruses are the

only group within the *Peribunyaviridae* family that are associated with animal or human disease.

Orthobunyaviruses were first discovered when a novel infectious agent was isolated from a pool of *Aedes* mosquitoes near the town of Bunyamwera in the Semliki Forest region of western Uganda in 1943 (Smithburn et al., 1946). This virus subsequently became known as Bunyamwera virus (BUNV) and although not initially associated with human disease, it is now known to be the causative agent of Bunyamwera fever, for which symptoms include mild encephalitis, the appearance of a rash and occasional neurological impairment (Dutuze et al., 2018). BUNV became the 'type species' of the Orthobunyavirus genus, and also the prototypic member of the *Bunyavirales* order as a whole. Given the now apparent diversity that exists within this order, the relevance of such a general prototype is debatable. Other orthobunyaviruses that cause mild febrile disease in humans include Oropouche virus (OROV) (Sakkas et al., 2018) and Cache Valley virus (CVV) (Nguyen et al., 2013).

More serious pathogens within the orthobunyaviruses can be found within the California serogroup. The most well studied of these is La Crosse virus (LACV) which was first isolated from a fatal case of meningoencephalitis in the United States in 1960 (Thompson, W. H. et al., 1965). Symptoms are usually 'flu-like' and include fever, headache, vomiting and fatigue but serious neurological symptoms can arise and in rare cases these can be fatal. According to the Centers for Disease Control and Prevention (CDC) 736 cases of LACV were reported between 2009 and 2018, resulting in nine deaths, however, the number of annual LACV cases is likely to be highly under-reported as most people have such mild symptoms that they do not seek medical attention. Indeed, antibody surveillance suggests that 5000 to 15000 people are infected annually with LACV in the state of Indiana alone (Grimstad et al., 1984). Other clinically relevant members of the California serogroup include Jamestown

Canyon (JCV), Snowshoe hare (SSHV), Inkoo (INKV) and Tahyna (TAHV) viruses which have all been found to cause encephalitis in humans with various incidence rates (Atkinson & Hewson, 2018; Drebot, M., 2015; Evans et al., 2019; Hubálek, 2008).

Currently there are no treatments available which specifically target any of the human pathogenic orthobunyaviruses, although the inhibitory activity of broad-spectrum antivirals such as ribavirin and T-705 (favipiravir) against various bunyaviruses including orthobunyaviruses has been demonstrated (Cassidy & Patterson, 1989; Gowen et al., 2007). Shortly after the SBV outbreak in 2011 several prototype inactivated-virus based vaccines were developed by growing SBV on different cell substrates before inactivation with binary ethylenimine. These elicited protective antibody responses in sheep when tested (Wernike et al., 2013) and it was later shown that a single immunisation with one of these vaccines completely prevented viral replication in sheep (Hechinger et al., 2014). As of the end of 2019 a range of different recombinant subunit, DNA and genetically modified live-virus vaccines have been developed and tested with varying degrees of success. Three licensed vaccines are available, all based on inactivated-virus. These are Bovilis SBV (MSD Animal Health), Zulvac SBV (Zoetis) and SBV vax (Merial) (Endalew et al., 2019). Studies are ongoing into the use of attenuated viral vaccines against other orthobunyaviruses, and the effectiveness of a trivalent inactivated-virus vaccine has been demonstrated in animal models, which is designed to protect against the orthobunyaviruses Akabane virus (AKAV) and Aino virus (AINV) as well as the reovirus; Chuzan virus (Kim, Y.-H. et al., 2011).

## **1.4 Reassortment as a mechanism of orthobunyavirus emergence**

As segmented viruses, members of the orthobunyavirus genus are capable of reassortment, which is a process that can occur when two or more genetically-related viruses infect the same host cell. Nascent virions can package a combination of segments from one or other of the infecting parental viruses, creating new progeny that are genetically-distinct from either progenitor virus, and these are known as reassortants. One possible outcome of such events is the acquisition of new properties linked to the new genetic make-up of the reassortants, and one such property is a change in disease-causing potential. Combined with the increasing geographical range of their insect vectors due to climate change, this makes the orthobunyaviruses a potential source of emerging viral pathogens. This is of concern in the United Kingdom as increasing temperatures drives the expansion into the country of non-native insects, which in turn carry non-endemic orthobunyaviruses.

One of the most dangerous human pathogens within the orthobunyavirus genus is Ngari virus (NRIV) which was associated with an outbreak of haemorrhagic fever throughout Kenya, Tanzania and Somalia in 1997 and 1998 responsible for approximately 250 deaths. This outbreak was initially mistaken for RVFV before being attributed to a newly identified orthobunyavirus named Garissa virus (Bowen et al., 2001). Through later genetic analyses it was found that Garissa virus was actually an isolate of the already identified NRIV, which is a reassortant containing the S and L segments of BUNV but the M segment of Batai virus (BATV) (Briese et al., 2006; Gerrard et al., 2004). This example illustrates the potential for reassortment events to generate new and deadly orthobunyaviruses.

In 2011 a novel orthobunyavirus was detected in German cattle near the village of Schmollenberg, after which it was named (SBV), and was found to be related to Simbu serogroup viruses (Hoffmann, B. et al., 2012). By 2013 the European Food Safety Authority confirmed that SBV had been detected across mainland Europe from Spain to Poland and as far north as Scandinavia (European Food Safety Authority, 2013) and during that year cases were reported in Greece and Russia (Lievaart-Peterson et al., 2015). Economic impacts stemmed from loss of newborn sheep, reduced milk yield in cattle and reduced trade as the import of cattle and beef from affected areas was banned by other countries. Sequence analysis revealed SBV was a reassortant virus containing the S and L segments of Shamonda virus (SHAV) and the M segment of Sathuperi virus (SATV) (Yanase et al., 2012) although this conclusion has been disputed by others (Goller et al., 2012). As with NRIV this illustrates the capacity for reassortant orthobunyaviruses to be particularly pathogenic. Other orthobunyaviruses are pathogenic in ruminant animals and affect commercial livestock across multiple continents, including the previously mentioned AKAV (Kurogi et al., 1975) and CVV (Edwards, J. F. et al., 1989).

## **1.5 Orthobunyavirus vectors**

As arboviruses, the geographic range of orthobunyaviruses is determined largely by which areas are habitable to their insect hosts. The habitable range of insects is in turn dependent on climate and for many species, is changing rapidly as global temperatures increase, and this is already implicated in the increase in prevalence of arboviral disease globally (Gould & Higgs, 2009). In the UK a particular facet of this threat from invasive species of mosquito and tick which have already moved into mainland Europe (Baylis, 2017), with modelling of worse-case scenarios suggesting transmission of Dengue virus in the UK during summertime by the end of this century (Liu-Helmersson et al., 2016).

The orthobunyavirus replication cycle within the insect host is less well studied than within the mammalian host, but the virus has to contend with a very different cellular environment. Studies have shown that BUNV infection of viral cells involves the formation of very different viral superstructures within the Golgi (López-Montero & Risco, 2011) and infection in insect cells is persistent, unlike the lytic infections which occur in mammalian cells (Borucki et al., 2002).

## **1.6 General structural characteristics of the orthobunyaviruses**

Orthobunyavirus virions are pleiomorphic, roughly spherical and measure around 100 nm in diameter. They consist of a host-derived lipid membrane coated in a shell of glycoprotein spikes and contain three discrete molecules of negative-sense, single-stranded RNA that are known as segments (figure 1.1). The orthobunyaviral genome segments are named small (S), medium (M) and large (L); a designation based on their observed relative sedimentation characteristics during the initial biophysical characterization of the genomes of BUNV (Kascsak & Lyons, 1977) and the closely related LACV (Obijeski et al., 1976). The correlation of these sedimentation characteristics with their respective nucleotide lengths was confirmed by subsequent sequence determination, first of the BUNV genome (Elliott, 1989a; Elliott, 1989b; Lees et al., 1986), and then of the LACV genome (Akashi & Bishop, 1983; Grady et al., 1987; Roberts et al., 1995). Sequence analysis of orthobunyavirus segments reveals that all possess a short stretch of nine nucleotides at their extreme 3' and 5' termini that are highly conserved and complementary. These sequences are predicted to allow some degree of inter-terminal base-pairing, potentially allowing the linear RNA strands to adopt closed circular forms, and this suggestion is supported by direct visualization of purified RNPs by electron microscopy, as well as

biochemical and genetic evidence.

As described above, orthobunyaviral RNAs are not naked, but instead are protein-enwrapped to form RNPs, and they exist in this form throughout all stages of the viral life cycle, encompassing virus entry, gene expression and virion assembly. The virion-associated negative sense RNA (vRNA) segments act as templates for transcription to generate a single mRNA, and also RNA replication, to generate a complimentary RNA copy, known as the cRNA or anti-genome. While the vRNA and cRNAs are the same nucleotide length, the length of corresponding mRNAs are less well defined, exhibiting heterogeneity at both 5' and 3' ends; The mRNA 5' ends possess a non-viral sequence that comprises a 12-17 nucleotide-long capped oligoribonucleotide, derived from host cell mRNAs, whereas the mRNA 3' end is poorly defined (Jin, H. & Elliott, 1993). In contrast to the vRNA and cRNA replication products, viral mRNAs remain unencapsidated and do not form a viral RNP.

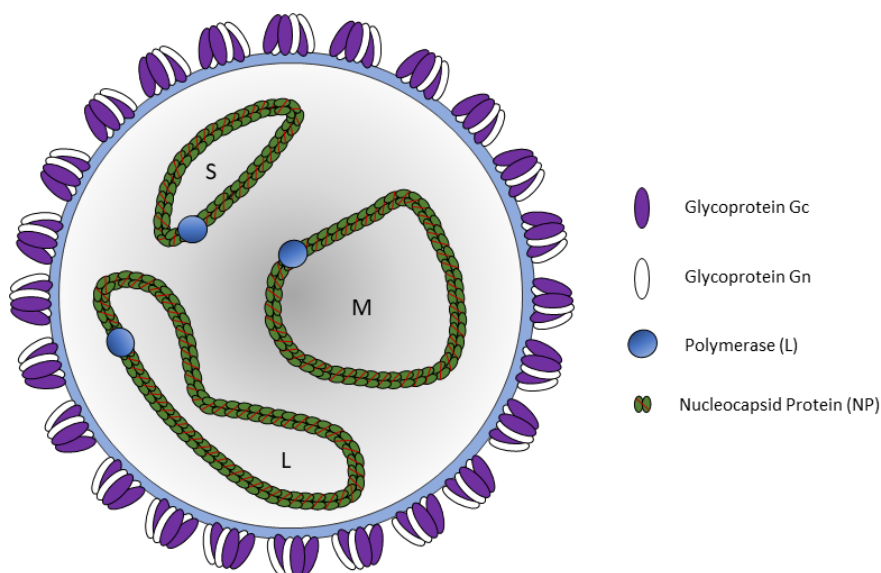


**Figure 1.1:** Schematic of an orthobunyavirus virion and its protein components. A host-derived lipid membrane is studded with glycoprotein trimers of heterodimers, and RNPs are composed from NP and the viral polymerase. S, M and L refer to the small, medium and large RNA segments respectively.

## 1.7 Orthobunyavirus segment coding strategy

All orthobunyaviruses studied to date have a common gene expression strategy, in which each of the three segments is transcribed to yield a single mRNA. The S mRNA encodes the nucleocapsid protein (NP) that binds the vRNA and cRNA templates to form RNPs, the M mRNA encodes a polyprotein precursor (GPC) that is subsequently cleaved into amino- and carboxy-terminal proteins (Gn and Gc) that form the virion glycoprotein spikes, whereas the L mRNA encodes the RNA-dependant RNA polymerase (RdRp).

For many, but not all, orthobunyaviruses these same mRNAs also encode non-structural proteins; the non-structural small segment (NSs) protein is expressed from a second open reading frame (ORF) on the S mRNA, accessed through by-pass of the first NP initiation codon by 'leaky scanning', whereas a non-structural medium segment (NSm) protein is cleaved from the GPC during its proteolytic processing. NSs has roles in blocking various host innate immune responses, whereas the role of NSm is less clear, although involvement in establishment of viral factories has been proposed (Fontana et al., 2008).

## 1.8 Orthobunyavirus multiplication cycle

### 1.8.1 Overview

The stages in the replication cycle of an orthobunyavirus will be explained in turn in more detail but a brief overview follows here, which is also illustrated in figure 1.2. Orthobunyaviruses are transmitted to their mammalian host via bites from infected insect vectors. Following attachment to host cell receptors and entry to the cell by endocytosis, the virus fuses with the endosome membrane to release its RNPs. The viral RdRp uses host-derived primers to transcribe the viral genome

segments into mRNA for subsequent translation of viral proteins, and the M-segment-encoded polyprotein is co-translationally cleaved to produce functional glycoproteins. RNA replication takes place to produce complementary RNA (cRNA) which is encapsidated by NP to make templates for new genomic RNPs. Virus assembly takes place in viral factories within the Golgi apparatus, following localisation of NP and the insertion of heterodimeric glycoproteins into the Golgi membrane. Cytoplasmic vesicles containing nascent viruses are trafficked to the cell

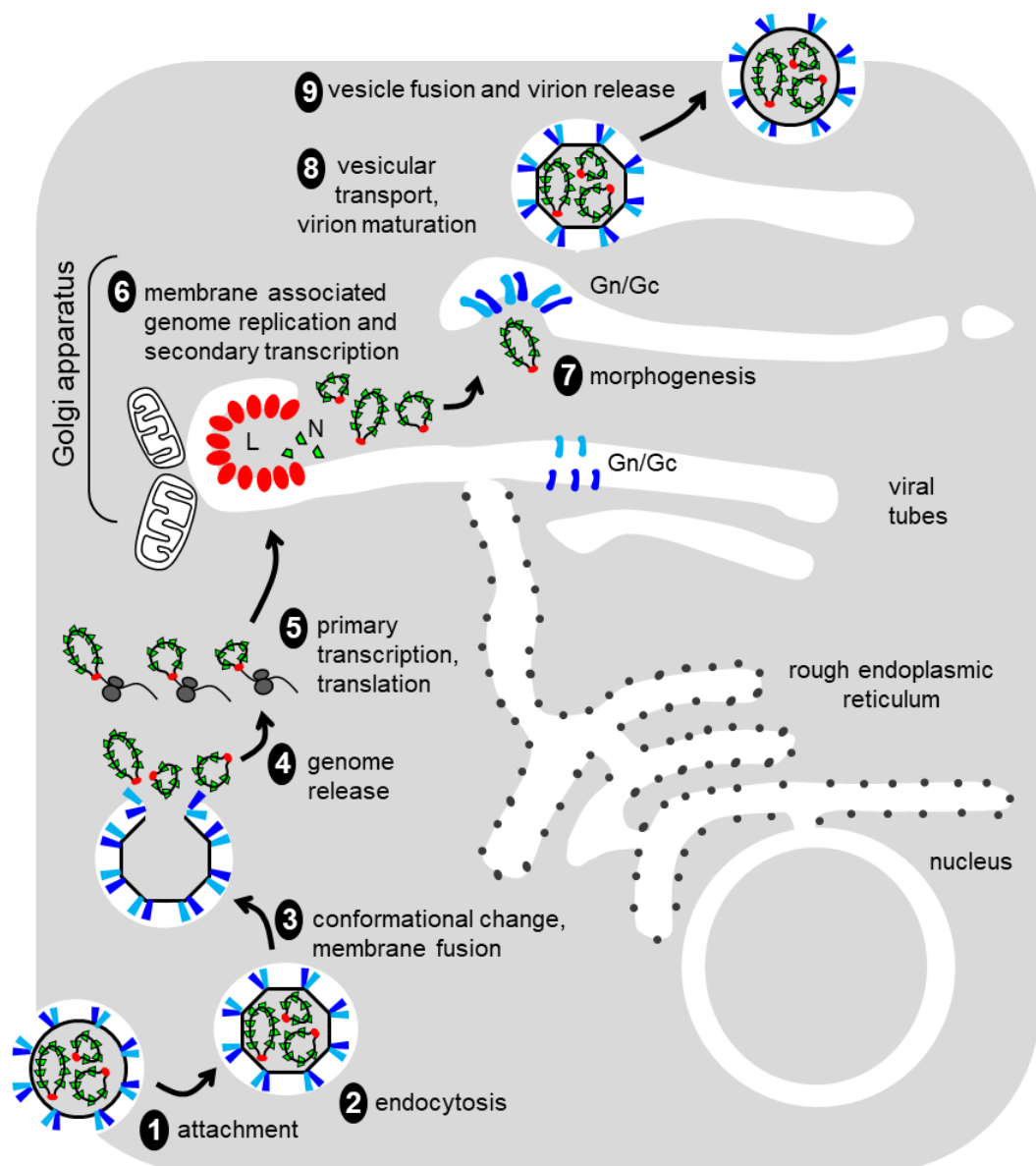


**Figure 1.2:** General orthobunyavirus replication cycle, illustrating cell entry, transcription and translation, genome replication, virion assembly, maturation and egress. Each stage is described in more detail in section 1.8. Reproduced from Howley & Knipe, 2020. *Fields Virology: Emerging Viruses*, 7<sup>th</sup> Ed. (LWW).

surface and fuse with the plasma membrane to release mature virions. Some members of the phleboviruses and hantaviruses have also been described to bud directly from the host cell plasma membrane, which may also be a possible alternative route of egress for orthobunyaviruses (Anderson Jr & Smith, J. F., 1987; Ravkov et al., 1997).

### **1.8.2 Cell entry**

Upon entering the mammalian host the first cells encountered by a virus are epidermal macrophages (Albornoz et al., 2016) and a number of C-type lectins; innate immune receptors expressed by macrophages, have been shown to interact with LACV on the surface of the cell (Hofmann et al., 2013; Monteiro et al., 2019). It has been demonstrated with LACV, AKAV and OROV that the initial entry of the virus into the cell involves the hijacking of clathrin mediated endocytosis (Albornoz et al., 2016; Santos, R. I. M. et al., 2008).

Following endocytosis, the virus-containing vesicles fuse with other endocytic compartments to form an early endosome, which then undergoes a process of maturation. This maturation is accompanied by a decrease in pH and orthobunyaviruses exhibit a dependence on this acidification for successful cell entry (Jacoby et al., 1993; Santos, R. I. M. et al., 2008), likely because a resulting conformational change in the viral glycoproteins facilitates fusion of the viral and host cell membranes and the release of RNPs into the cytoplasm. Evidence for the importance of this acidification process in orthobunyavirus infection is provided by the observation that inhibiting endosomal acidification with ammonium chloride (NH<sub>4</sub>Cl) blocks infection with BUNV (Hover et al., 2018).

In addition to pH, intra-endosomal potassium ion concentrations are also an important factor in orthobunyavirus entry. The activity of potassium ion channels within endosomal membranes, and accompanying potassium ion influx have both been shown to be required for the release of BUNV RNPs from endosomes (Hover et

al., 2018). Potassium ion influx has also been shown to be essential for Hazara virus (HAZV) entry and cryo-EM has elucidated a possible mechanism for this; potassium ions induce a large conformational change in the glycoproteins on the virion surface, which causes them to adopt an elongated conformation, and interact with lipid membranes. The extended form likely allows the exposure of a hydrophobic peptide on the glycoprotein spike that mediates the membrane interactions (Punch et al., 2018). Due to its role in maintaining potassium ion homeostasis, the levels of cellular cholesterol are another factor that correlates with the efficiency of the infection of these viruses (Charlton et al., 2019).

### **1.8.3 mRNA transcription**

After fusion of the virus with the endosome and release of the three virion-associated vRNPs into the host cytoplasm, the initial RNA synthesis event that occurs is primary transcription to produce viral mRNAs for subsequent translation into viral proteins. The *cis*-acting signals that direct the RdRp to initiate mRNA transcription from the vRNA template are entirely contained within the segment NTRs and comprise the nine highly conserved nucleotides at the vRNA 3' end, as well as additional nucleotides proximal to both 3' and 5' termini (Barr et al., 2005). The finding that nucleotides located at both 3' and 5' NTRs are required to promote transcription further strengthens the proposal that orthobunyaviral vRNA segments are functional in a circular form.

Orthobunyaviral mRNAs contain a short stretch of between 10-14 non-templated nucleotides at their 5' end (Bishop et al., 1983) and more detailed examination suggested these sequences were derived from host cell mRNAs (Patterson & Kolakofsky, 1984) possibly using a cap-snatching mechanism similar to that described for influenza virus. The influenza cap snatching mechanism involves the binding of a capped cellular mRNA by the viral polymerase, followed by its endonucleolytic cleavage close to its 5' end and the subsequent use of this capped

oligoribonucleotide as a primer for the initiation of transcription (Dias et al., 2009; Plotch et al., 1981; Serna Martin et al., 2018; Yuan et al., 2009). Experiments with LACV demonstrated that purified virus exhibited endonuclease activity, suggested to result from the virion-associated RdRp (Patterson et al., 1984) and recombinant expression systems later demonstrated that the orthobunyaviral polymerase contained the necessary endonuclease domain for the cap snatching activity (Jin, H. & Elliott, 1993). More recent structural work has elucidated some of the mechanisms of how the orthobunyaviral polymerase facilitates cap-snatching. A detailed discussion of the structure of the orthobunyaviral polymerase will follow in 1.9.1 but an observation from the BUNV polymerase structure that is important to understand mRNA transcription is the proximity of the product exit tunnel to the polymerase endonuclease domain, which is responsible for cap-snatching (Gerlach et al., 2015). The authors propose that during transcription the cap-snatched primer enters the polymerase through the product exit tunnel and leaves by the same route. A similar mechanism of template entry through the product exit channel has been demonstrated in IAV transcription (Reich et al., 2014).

BUNV mRNAs do not possess a 3' poly(A) tail and the presence of the intact S-segment untranslated-region (UTR) has been shown to possess translation enhancing properties (Blakqori et al., 2009), although the mechanism of such enhancement is unknown. Knockdown of poly(A) binding protein (PABP) did not affect viral mRNA translation which, combined with the observation that BUNV infected cells display reduced PABP expression, suggests that BUNV targets PABP to reduce translation of cellular mRNAs. At the same time the virus facilitates the translation of its own mRNAs in a PABP-independent manner, that possibly involves eukaryotic initiation factor 4G (eIF4G) and stem loop structures that have been predicted to form in the 3' UTR (Blakqori et al., 2009).

The viral mRNAs are also truncated at their 3' end relative to the S segment vRNA template and detailed analysis of the BUNV genomic S segment 5' UTR identified two sequences of nucleotides responsible for transcription termination. These two sequences had a pentanucleotide repeat in common that was also present in the BUNV L segment 5' UTR and also S segments 5' UTRs of other orthobunyaviruses (Barr et al., 2006). A later study using recombinant viruses identified one of these sequences in particular responsible for transcription termination (Blakqori et al., 2012). Its presence in multiple different orthobunyaviral genomic segments illustrates a degree of conservation of this sequence across the genus, but its absence in some sequences suggests that alternative transcription termination sequences may also exist.

Treating infected cells with translation-inhibitors, such as cycloheximide abrogates the production of viral mRNAs (Abraham & Pattnaik, 1983; Patterson & Kolakofsky, 1984). A model was proposed in which transcription is inhibited by base-pairing between the nascent RNA and its template (Raju & Kolakofsky, 1987). In a subsequent study, model BUNV genome segments containing premature stop-codons were used to demonstrate that transcription termination signals are ignored by a transcribing polymerase because the translating ribosomes on the nascent mRNA somehow interfere with polymerase activity, possibly by physically interacting with stalled polymerases, and blocking transcription termination (Barr, 2007).

### 1.8.4 Genome replication

In response to currently undefined circumstances, following the onset of RNA synthesis the activity of the RdRp switches from primary transcription to RNA replication. RNA replication differs from transcription in several fundamental ways including independence of a host-derived capped oligonucleotide as primer, a lack of response of the RdRp to vRNA transcription termination signals and the encapsidation of the nascent cRNA replication product by NP. As for primary transcription, the *cis*-acting signals required for RNA replication reside entirely within the NTRs, and functional analysis of these sequences has shown involvement of the terminal conserved sequences as well as a requirement for inter-terminal base pairing (Barr et al., 2005). Another similarity with primary transcription is the requirement for ongoing protein synthesis (Patterson & Kolakofsky, 1984)

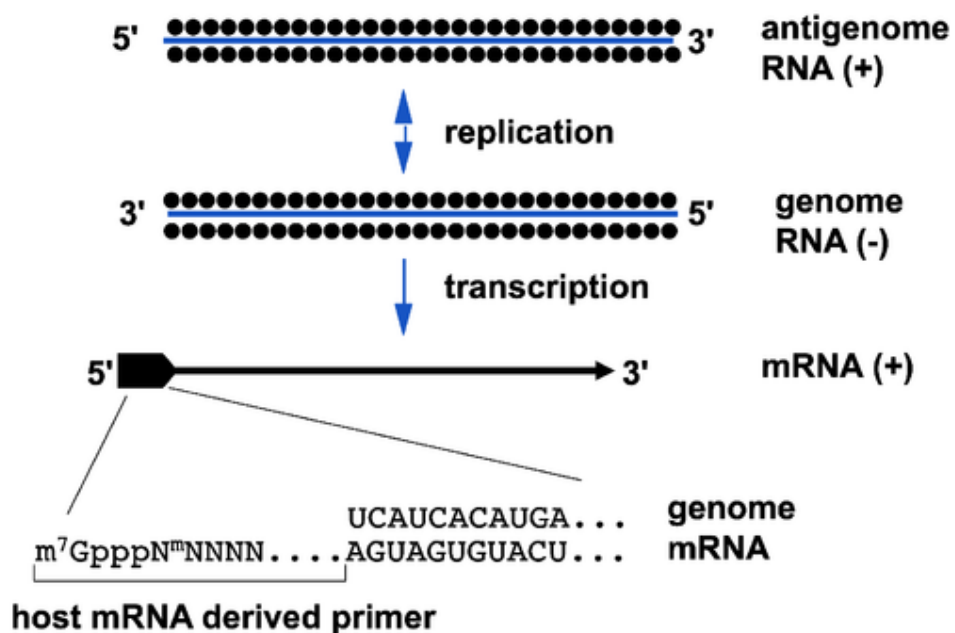


**Figure 1.3:** Replication and transcription in bunyaviruses. Genomic and anti-genomic RNA exist as RNPs, encapsidated by NP. Segments are shown as linear but are likely circularised for transcription and replication. Viral mRNAs are truncated at their 3 end and contain a host-derived cap at their 5' end. Viral mRNAs are not encapsidated by NP. Reproduced from Howley & Knipe, 2020. Fields Virology: Emerging Viruses, 7<sup>th</sup> Ed. (LWW).

The solution of the LACV polymerase structure (described in section 1.9.1) has led to considerable insight into fundamental stages in bunyaviral RNA synthesis including vRNA promoter recognition, template entry and exit, nucleotide polymerization, and mRNA priming. This information has subsequently allowed the construction of a new model for orthobunyaviral RNA replication (figure 1.4). Critical in developing this model was the finding that the RdRp has template entry and exit tunnels in close proximity to each other (Gerlach et al., 2015) that likely permit template RNA to dissociate from NP, enter the interior of the polymerase, and leave via the exit tunnel where it reassociates with NP. Thus, RNA replication can take place with little disruption to the integrity of the viral RNP.

The product RNA exits on the other side of the polymerase to the sites of template entry and exit. For replication of RNPs the product RNA must be encapsidated to form complementary RNPs. The authors propose that an apo polymerase binds to the emerging newly polymerized RNA to aid in its encapsidation by NP to form the nascent RNP, and that dimerization of the polymerase is essential for this. This model is supported by observations of the structurally similar influenza A virus (IAV) polymerase, that requires a second, *trans*-acting polymerase for genome replication (York et al., 2013) and it was recently shown that dimerization of the two polymerases is essential for IAV genome replication (Fan et al., 2019). A more detailed description of insights into genome replication gained from the LACV crystal structure will follow in section (1.9.1)

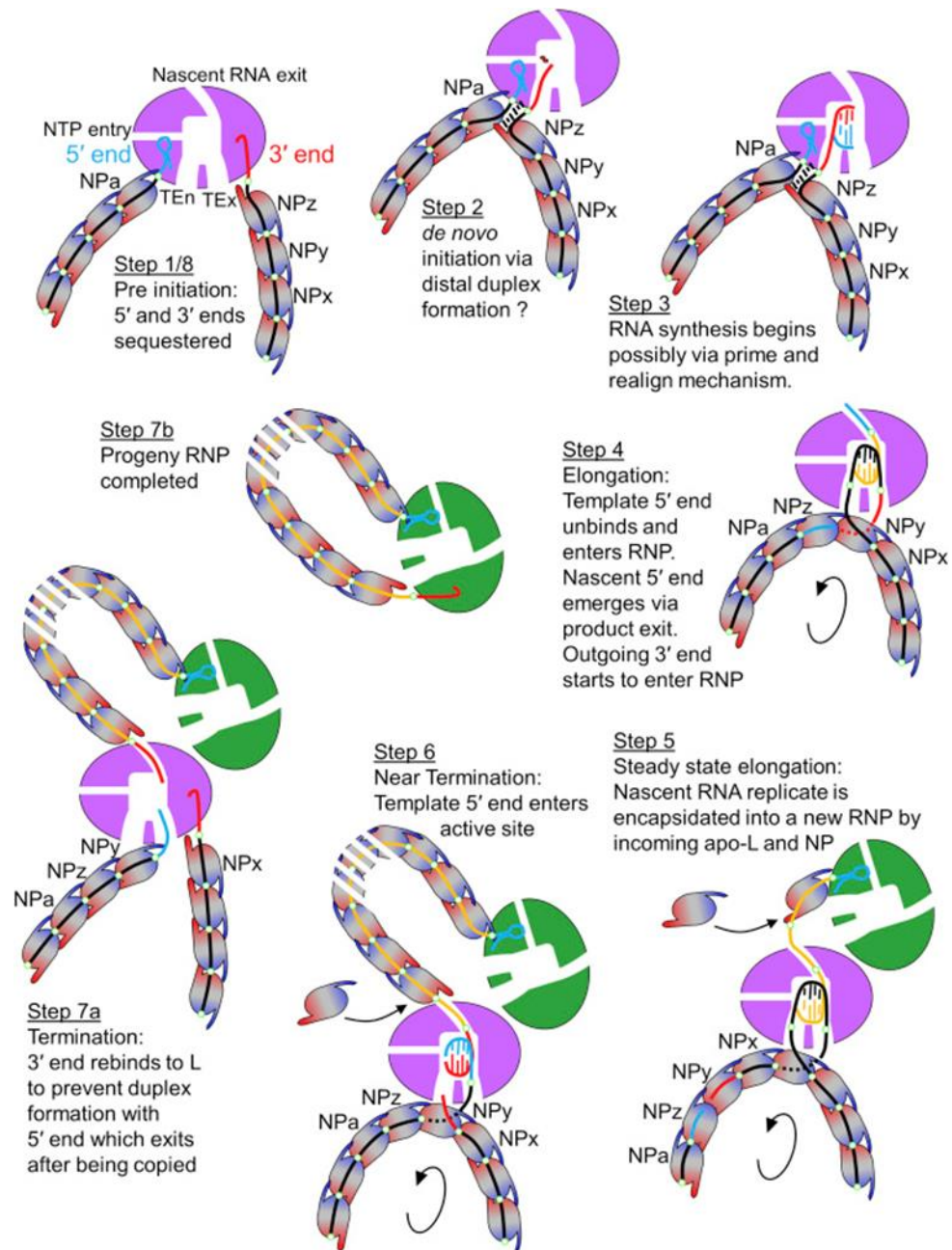


**Figure 1.4:** Schematic for RNP replication, describing initiation, elongation, transcription and the role of a second *trans*-acting polymerasae. Described in detail in section 1.9.1. Reproduced from (Gerlach et al., 2015).

### 1.8.5 Viral factories

Transcription and replication, as well as subsequent translation and assembly activities, are thought to occur within membrane-associated viral replication factories, similarly to flaviviruses (Paul & Bartenschlager, 2015). EM has shown these

replication factories to be tubular structures that form after the rearrangement of the normal architecture of the Golgi apparatus, and comprise viral NP and Nsm and host-cell-derived proteins such as actin and myosin I, with tube assembly being sensitive to drugs affecting actin polymerization. (Fontana et al., 2008; Salanueva et al., 2003). After assembly, viruses traverse the stacks of the Golgi apparatus and continue to undergo structural maturation, as their glycoproteins undergo conformational changes in response to changing glycosylation states and the acquisition of endo- $\beta$ -*N*-acetylglucosaminidase H (endo-H) resistance, before exiting the Golgi in vesicles and undergoing a final maturation stage as they transit to the cell surface for exocytosis (Novoa et al., 2005).

## **1.9 Structural aspects of viral proteins**

### **1.9.1 RNA-dependent RNA polymerase (RdRp)**

The viral polymerase copies the negative-sense vRNA as a template to generate positive-sense mRNAs or cRNA anti-genomes, which in turn act as replication intermediates for the generation of further vRNA strands. The only orthobunyavirus polymerase structural information available to date is for LACV, for which both a crystal structure and EM density map are available (Gerlach et al., 2015). These data show that LACV polymerase conforms to the characteristic 'palm and fingers' structure common to other RNA viruses of both positive and negative sense, and which has been particularly well studied in the closely related influenza virus (Fan et al., 2019; Pflug et al., 2014; Reich et al., 2014). When LACV polymerase is aligned to the trimeric influenza RdRp, the LACV central core maps to the influenza PB1 domain, the LACV N-terminal region maps to the influenza PA domain, and the LACV C-terminal region maps to the influenza PB2 domain, although the C-terminal ~500 residues were not represented in the LACV structure.

The LACV polymerase N-terminal region contains the endonuclease domain responsible for cap-snatching, which had previously been characterised (Reguera et al., 2010) and is structurally similar to that found in influenza (Dias et al., 2009; Yuan et al., 2009). Similar cap-snatching domains have also been identified in the polymerases of members of other major families of the *Bunyavirales* such as the nairoviruses (Devignot et al., 2015; Holm et al., 2018), arenaviruses (Morin, B. et al., 2010; Reguera, Gerlach, Rosenthal et al., 2016; Wallat et al., 2014), hantaviruses (Fernández-García et al., 2016; Reguera, Gerlach, Rosenthal et al., 2016) and phleboviruses (Holm et al., 2018).

The solution of the LACV RdRp crystal structure led to models of its interactions with the RNP during genome replication. The 3' vRNA is bound across the surface of the N-terminal region of the RdRp and held in place with a 'clamp', and a large number of hydrogen bonds between protein and RNA indicate the sequence specificity of this binding. The 5' vRNA forms a stem-loop held together by two base-pairing interactions, which binds to the side of the RdRp and forms a large number of hydrogen bonds, also indicating sequence specificity. Upon 5' vRNA binding the RdRp undergoes conformational changes to promote its binding to the RNA, and also to stabilise its active site. The number of hydrogen bonds forming between the vRNA ends and their binding sites, and sequence specificity required for this, provides a structural understanding for why orthobunyaviral UTRs have such high sequence conservation.

Holding the 3' and 5' vRNA ends separately on opposite sides of the RdRp could be compatible with the formation of an intact RNP. However, the 3' vRNA would have to translocate into the template entry channel for RNA replication to commence, and as of yet there is no information available on the conformational change this would require, and how such movement occurs in the context of an NP enwrapped RNP. As replication progresses the 5' vRNA also translocates away from the RdRp

and into associated NP. In the internal chamber of the protein a duplex of template and product is formed which then splits between two exit channels, leading to the template and product exiting on opposite sides of the RdRp, and avoiding interaction with each other. The template exits in close proximity to where it enters and is likely able to reassociate with NP with minimum disruption to the RNP and minimum exposure of unencapsidated RNA nucleotides. The internal template channel can accommodate around 20 nucleotides and since NP binds ~10 nucleotides and ~10 nucleotides from the 5' and 3' vRNA ends bind the RdRp, this model predicts that no unencapsidated RNA is exposed. The orthobunyaviral polymerase has been shown to associate with NP during the formation of RNPs (Eifan & Elliott, 2009; Shi, X. et al., 2006), and such an interaction would aid in stabilising the replication complex described in this model, however little information is available on the nature of this

interaction, particularly for orthobunyaviruses.

In the described model of orthobunyaviral genome replication the nascent RNA is assembled into a new RNP by interacting with NP and an apo RdRp. This would be likely to involve dimerisation of the RdRp, which has not yet been observed for orthobunyaviruses. More structural information is available for the influenza virus polymerase which, due to the structural similarity, is likely to also be relevant to the mechanism of orthobunyavirus polymerase action. Influenza virus polymerase transcribes genomic vRNA into capped, poly-adenylated mRNA for protein synthesis, as well as copying the genomic RNA template into a complementary RNA to serve as a replication intermediate for production of further genomic RNA copies (Fodor, 2013). Isolation of one such complementary RNP showed that a *trans*-acting polymerase is required to activate replication and produce more genomic RNPs

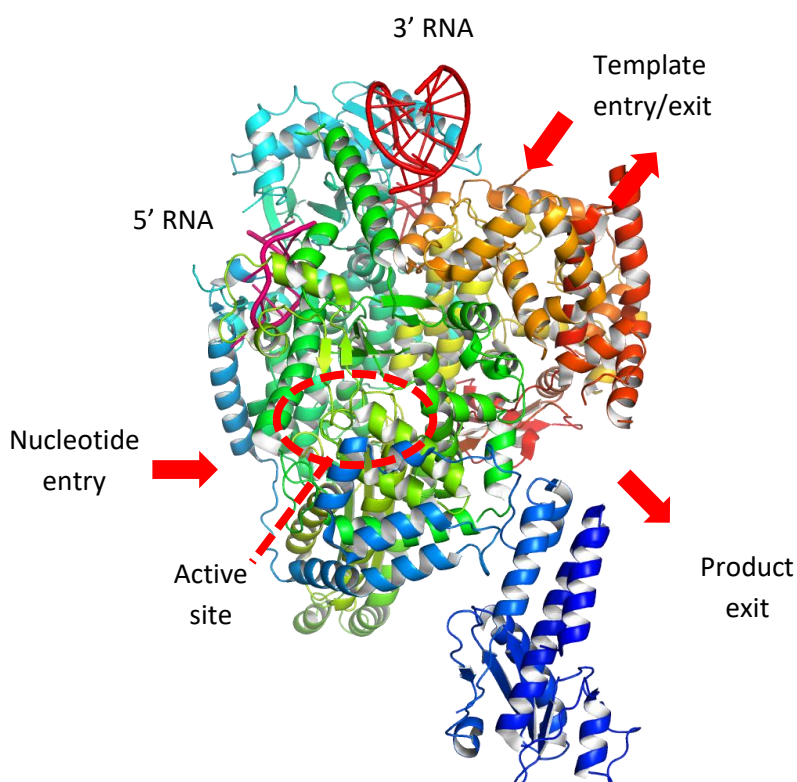


**Figure 1.5:** Crystal structure of the polymerase of LACV, bound to 3' and 5' viral RNA. Bound RNA is indicated, as are the entry and exit sites of template and product. Adapted from (Gerlach et al., 2015), PDB: 5AMQ.

(York et al., 2013), in agreement with previous work which demonstrated the potential of the influenza virus polymerase heterotrimer to oligomerise (Jorba et al., 2008) and a model of cRNA replication by trans-acting polymerase (Jorba et al., 2009). Recent work has shown that this *trans*-acting polymerase acts through dimerisation, which induces a conformational change in the priming loop to realign the template RNA (Fan et al., 2019).

### 1.9.2 Glycoproteins

The orthobunyavirus M segment contains a single ORF which encodes a polyprotein of Gn, NSm and Gc, in that order (Fazakerley et al., 1988). This is cleaved by host proteases such as signal peptidase and signal peptide peptidase (Shi, X. et al., 2016) to form the two glycoproteins, Gc and Gn as well as the non-structural protein NSm. These proteins then form heterodimers (Lappin et al., 1994), which localise to the Golgi apparatus. For orthobunyaviruses and phleboviruses it has been shown that Gn alone but not Gc alone localises to the Golgi so heterodimerisation is required for correct retention of glycoproteins in the Golgi for viral assembly (Melin et al., 1995; Shi, X. et al., 2004). Similarly, hantavirus glycoproteins require heterodimerisation for correct Golgi localisation, but neither Gn or Gc can localise to the Golgi on their own (Deyde et al., 2005). Available crystal structures of non-orthobunyavirus Gc all display it in a trimeric post-fusion form (figure 1.6A) (Guardado-Calvo et al., 2017; Guardado-Calvo et al., 2016; Halldorsson et al., 2016; Willensky et al., 2016) and it has been demonstrated that during orthobunyavirus assembly Gn-Gc heterodimers trimerise to form hexameric spikes with a tripodal structure (Bowden et al., 2013). These spikes are embedded in the host derived lipid membrane surrounding the virion and form locally ordered patches which display three-fold symmetry (figure 1.6B). This model of the glycoprotein spike structure was recapitulated when the glycoproteins of BUNV, LACV, OROV and SBV were crystallised and the resulting atomic models were docked into the EM map of the

BUNV spike (Hellert et al., 2019) (figure 1.6C). The overall lattice arrangement of glycoproteins has also been studied in other *Bunyavirales*. Hantavirus glycoproteins display 4-fold symmetry and form patches of local order, but areas of membrane are also found to lack spikes (Battisti et al., 2011; Huiskonen et al., 2010). Phleboviral glycoproteins exhibit another conformation again, forming an icosahedrally symmetrical lattice around the entire virion (Freiberg et al., 2008; Huiskonen et al., 2009; Överby et al., 2008; Sherman et al., 2009).

The glycoprotein spikes interact with the host cell to mediate virus entry (Albornoz et al., 2016). There is also evidence that following endocytosis of the virus the conditions within the endosome trigger large conformational changes in the glycoprotein spikes and mediate membrane fusion and release of RNPs (Halldorsson et al., 2018; Punch et al., 2018). This large conformational change in glycoprotein to mediate membrane fusion is seen in many other viruses such as influenza virus (Blijleven et al., 2016). The glycoprotein heterodimer contains a trans-membrane region which crosses the viral lipid envelope and protrudes into the virion. It is hypothesised that across the *Bunyavirales* these cytoplasmic tails interact with NP and act as a surrogate for the matrix proteins found in other negative RNA viruses, to facilitate RNP packaging into nascent virions (Strandin et al., 2013). Interactions between glycoproteins and NP have been demonstrated for hantaviruses (Hepojoki et al., 2010), phleboviruses (Överby et al., 2007; Piper et al., 2011) and tospoviruses (Ribeiro et al., 2009; Snippe et al., 2007).

### **1.9.3 Nucleocapsid protein (NP)**

Orthobunyavirus NP is a globular protein of approximately 25 kDa encoded by the genomic S segment. In 2013, the crystal structures of the NP of four orthobunyaviruses from different serogroups were published, revealing the overall structural organization of the protein and how this relates to its RNA binding and homotypic assembly functions (figure 1.7A) (Ariza et al., 2013; Dong, H., Li, P.,

Böttcher et al., 2013; Dong, H., Li, P., Elliott et al., 2013; Li, B. et al., 2013; Niu et al., 2013; Reguera et al., 2013). NP has a central core domain comprised of N- and C-terminal lobes between which runs a positively charged groove that is involved in RNA binding. Extending from either side of the globular core are C- and N-terminal arms, which are connected to the core by a highly flexible linker and which facilitate the binding of neighbouring NP monomers to one another (Elliott, 2014). These two features of RNA binding and oligomerisation allow NP to assemble onto and encapsidate the viral genome and form RNPs, which is likely to be important for protection of the RNA from the host immune system and aiding in its packaging into nascent virions. Despite low sequence homology the published orthobunyaviral NP structures were very similar, illustrating the common mechanisms of RNA binding and oligomerisation across the genus.

Two of the NP crystal structures published in 2013 are of BUNV NP bound to RNA (Ariza et al., 2013; Li, B. et al., 2013), both of which crystallised as a tetramer with 4-fold symmetry (figure 1.7B). As with the other orthobunyavirus NP structures, both of these structures show that the globular core is divided into N- and C-terminal lobes either side of an RNA-binding groove. However, the two structures differ slightly

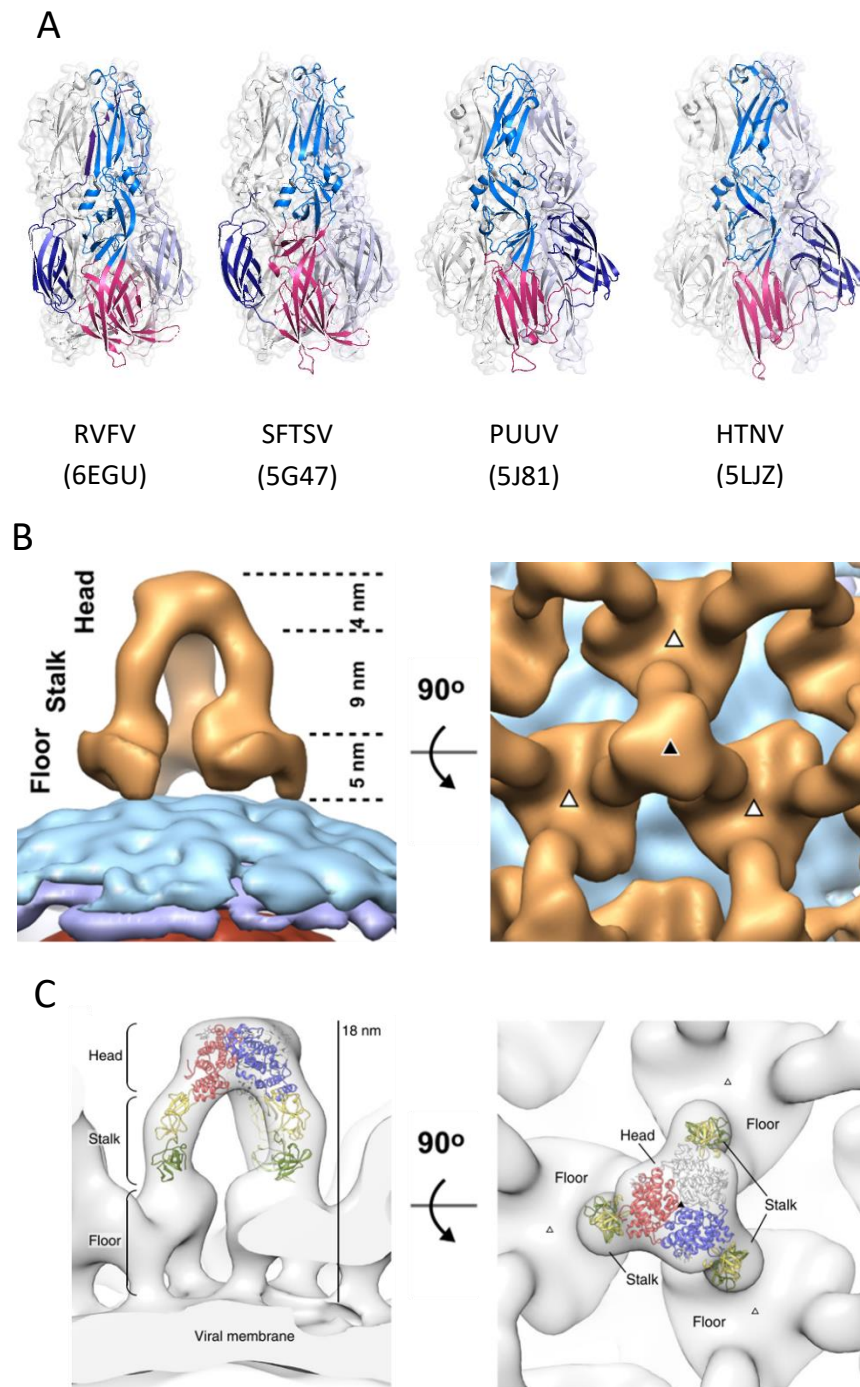


**Figure 1.6:** Bunyaviral glycoprotein structure. **(A)** Crystal structures of Gc from the phleboviruses, RVFV and Huaiyangshan banyangvirus (formerly SFTSV), and the orthohantaviruses HTNV and Puumala virus (PUUV). PDB accession numbers underneath their respective structures. **(B)** Glycoprotein spike structure of BUNV determined by cryo-ET shows a tripodal architecture, adapted from (Bowden et al., 2013). **(C)** The crystal structure of orthobunyaviral Gc was solved and could be docked into the tripodal spike model from (B), adapted from (Hellert et al., 2019).

in their exact arrangement of helices, and whether they are all  $\alpha$ -helices or some  $3_{10}$  helices, but generally there is agreement that the C-lobe is composed entirely of helices and the N-lobe is formed from approximately four helices and two  $\beta$ -strands. There is also agreement that the RNA-binding groove of each BUNV NP monomer has the capacity to bind 10 nucleotides, with NP tetramers binding 44 nucleotides, in close agreement with previous results (Mohl & Barr, 2009). These structures show that the BUNV NP RNA-binding groove is lined with many residues with positively-charged side chains that interact with the RNA phosphate backbone (Ariza et al., 2013; Li, B. et al., 2013) and the importance of these interactions was shown by reduced binding affinity when these residues were substituted with alanines (Ariza et al., 2013). The generation of temperature-sensitive mutants in this paper also identified a mutant with a 10 residue NP C-terminal extension that could still replicate.

One of the studies into BUNV NP described above also presented a structure of apo NP from SBV (Ariza et al., 2013), which showed that this NP has an extremely similar structure to that of BUNV but only has 2-fold symmetry, and its oligomerisation arms adopt different conformations within the tetramer compared to those of BUNV. Two further structures of SBV NP were also published; one apo and one RNA-bound (Dong, H., Li, P., Böttcher et al., 2013; Dong, H., Li, P., Elliott et al., 2013). The overall structures of NP were in close agreement with each other and the available BUNV NP structures (Ariza et al., 2013; Li, B. et al., 2013). However, the apo tetramer adopts a different conformation in which two C-terminal arms extend out into the solvent. Interestingly, the apo protein was crystallized as a hexamer with 3-fold symmetry, possibly as a consequence of the purification procedure used, which involved denaturation and refolding.

Two interesting suggestions were made by (Dong, H. et al.). The first is that the N-terminal oligomerisation arm may play a role in RNA binding and protection. As it bridges the gap between two monomers it effectively shields the RNA in this

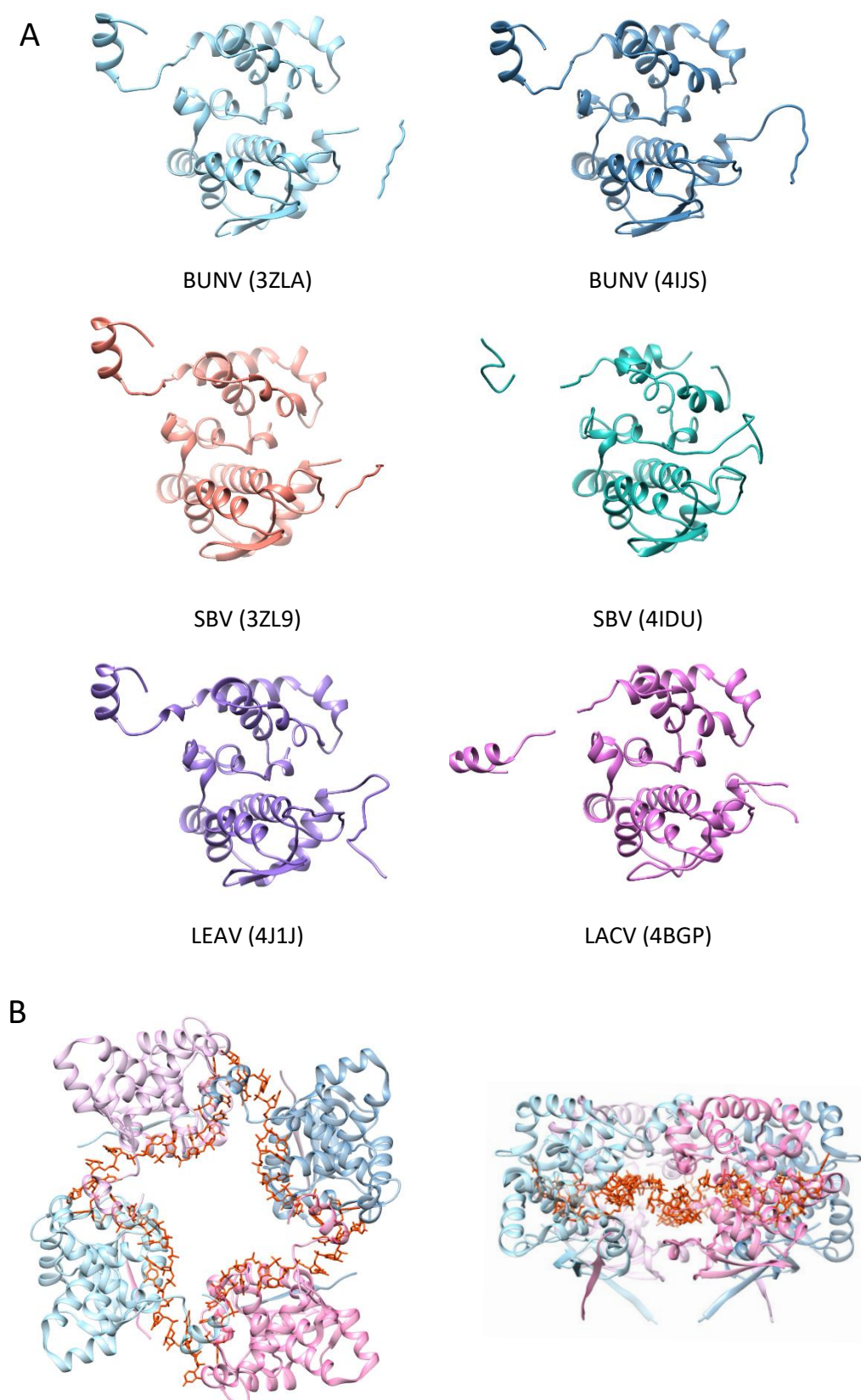


**Figure 1.7:** Crystal structures of orthobunyavirus NP. (A) Available structures of monomeric orthobunyavirus NP. Virus and PDB accession code are indicated below each respective structure. (B) RNA-bound BUNV NP tetramer (3ZLA), illustrating oligomerisation and the RNA binding groove. RNA = orange sticks.

gap from the outside of the tetramer. The second observation is that one of the N-terminal arms within the tetramer adopts a different conformation to the other three; facing more away from the RNA-binding groove in the apo structure and not resolving at all in the RNA-bound structure.

The structure of LACV and Leanyer virus (LEAV) NP were both solved and shown to be highly similar to the NP of BUNV and SBV; both had a globular core composed predominantly of  $\alpha$ -helices and both had C- and N-terminal lobes between which approximately 11 RNA bases were bound in a groove. LACV NP was crystallised as both an apo monomer and an RNA-bound tetramer (Reguera et al., 2013). It was observed that in the tetramer a 2-fold symmetry was adopted and the different pairwise equivalent NPs exhibited different conformation of their C-terminal arm. Of particular note, LACV tetramers treated with RNase and thiocyanate crystallised as a helix, solved at low resolution. The LEAV NP structure was determined bound to both RNA and single-stranded DNA (Niu et al., 2013) and of interest, the oligomerisation arms adopted the same conformation across all four subunits of the tetramer.

Overall, the published crystal structures of orthobunyavirus NP show that they crystallise preferentially as a tetramer. They all have a globular domain of similar structure, although the exact arrangement of helices differs, with a positively charged RNA binding groove containing essential charged residues. When examined together the structures also illustrate the dynamism and flexibility of the oligomerisation-mediating C- and N-terminal arms. Almost all of the structural models for orthobunyaviral NP have much higher RMSD values (root-mean-square deviation, a measure of how closely two superimposed proteins can be aligned) when comparing the arms to the core domains and in some of the models not all of the arms can be resolved due to their flexibility, or they are only partially resolved. The C-terminal arm can also accommodate the addition of more amino acids while

retaining its function. This flexibility permits the different orientations of the arms, which must be required for the formation of different oligomers seen by mass spectrometry and negative-stain EM (Li, B. et al., 2013; Murillo et al., 2018; Shepherd et al., 2014) and which must also be required to form filaments which are themselves flexible to facilitate processes such as transcription, replication and packaging into virions

## 1.10 Other viral NP structures

### 1.10.1 *Bunyavirales*

Four different crystal structures have been published for the NP of the nairovirus CCHFV, which exhibits a very different structure to NP from orthobunyaviruses (Carter et al., 2012; Guo et al., 2012; Wang, Y. et al., 2012). CCHFV NP has a single globular core domain built from residues from both C- and N-terminal portions of the protein. It does not possess flexible terminal oligomerisation arms, but instead it has one large arm-like domain extending away from the globular domain, so the protein resembles a 'bat' with a head and a handle (figure 1.8A-B). When comparing the different published structures of apo monomeric NP (Carter et al., 2012; Guo et al., 2012) the handle domain adopts very different positions, with a lateral shift of approximately 40 Å, which implies a high degree of flexibility, likely to be important for oligomerisation. Both structures also identified regions of positive charge on the head domain, which are potential sites of RNA binding.

Another group presented the crystal structure of oligomeric CCHFV NP. Along one crystal axis it formed an end-to-end trimeric arrangement, clearly illustrating the binding sites of one monomer to the next. Along a different crystal axis it formed an anti-parallel superhelix, mediated by the 'handle' of one monomer contacting the base of the 'head' of its neighbour. Upon incubation with short RNAs the superhelix

was broken and monomeric NP was crystallised with a different conformation of its handle, further illustrating the flexibility of this oligomerisation domain (Wang, Y. et al., 2012). A crystal structure is also available for the NP of HAZV, a very close structural analogue of CCHFV that is not associated with human disease, and thus amenable to study at a lower containment level. HAZV NP is structurally similar to all of the available CCHFV structures, and exhibits the same head-to-tail binding of monomers, and similarly located patches of positive electrostatic potential where RNA may bind (Surtees et al., 2015).

The first crystal structure solved of any *Bunyavirales* member NP was that of the phlebovirus RVFV. The RVFV NP was solved as an RNA-free monomer and exhibited the same bi-lobed, globular core that is typical of the orthobunyaviruses. However the RVFV NP structure lacked a distinct and continuous groove or patch of positive charge that could indicate a site of RNA binding and it also lacked any protrusions that might function as oligomerisation arms (Raymond et al., 2010). A subsequent structure was solved of RVFV NP in a hexameric ring form, and in which the N-terminal arm was extended and in contact with the adjacent NP monomer, mediating oligomerisation. Comparison between monomer and hexamer forms showed this N terminal arm blocked the RNA binding groove in the monomer, but in the multimer this arm was repositioned to reveal a cleft lined with positively charged residues, confirmed by mutagenesis to be essential for RNA binding (Ferron et al., 2011). These data allowed the proposal of a model for RNP formation in which the repositioning of this helix was proposed to act as a 'gate' and for which RNA binding and multimerization to form the growing RNP strand were mechanistically linked (Raymond et al., 2012).

Several crystal structures of another phlebovirus, Toscana virus (TOSV) NP, recapitulated the findings of RVFV, with this phlebovirus NP forming hexameric rings (Baklouti et al., 2017; Olal et al., 2014). Of significant interest, some of these

structures revealed a mechanism by which RNA binding triggers a displacement in the planar hexameric ring of NP to generate a helical structure (Olal et al., 2014). The structures of NP from SFTS, Buenaventura and Granada viruses (SFTSV, BUEV, GRAV) also confirmed the location of the RNA binding groove in phleboviral NP and their ability to crystallise as tetramers, pentamers and hexamers (Jiao et al., 2013).

Structural analyses of the NP of orthohantaviruses established that they, like other members of the *Bunyavirales* order, have a globular core formed from two lobes with an RNA binding groove between them and have two distinct arms that mediate oligomerisation (Arragain et al., 2019; Guo et al., 2016; Olal & Daumke, 2016). They are also readily able to form helices with a cryo-EM derived structure showing a helix with 3 monomers per turn and a crystal structure showing a helix with 6 monomers per turn.

The structure of the NP of the bi-segmented arenavirus LASV is very similar to that of CCHFV NP (Carter et al., 2012) and has been shown to trimerise by a series of head-to-tail interactions much like that described for CCHFV (Brunotte et al., 2011). The structural similarities of the arenaviral NPs with that of the nairoviruses is consistent with their recent re-classification into the *Bunyavirales* order, and confirms the deep evolutionary roots of both bi- and tri-segmented bunyaviruses. The arenavirus NP has two distinct lobes either side of a deep RNA binding groove like many other bunyaviruses (Hastie et al., 2011; Qi, X. et al., 2010). Comparison of crystal structures of LASV NP with and without bound RNA have revealed a plausible explanation for how initially-translated monomeric NP is unable to bind RNA, whereas NP in its multimeric state is competent for RNA binding. This switch in RNA binding activity depends on the repositioning of a single helix, proposed to act as an RNA-binding 'gate', opening up a continuous positively charged patch on the NP surface.

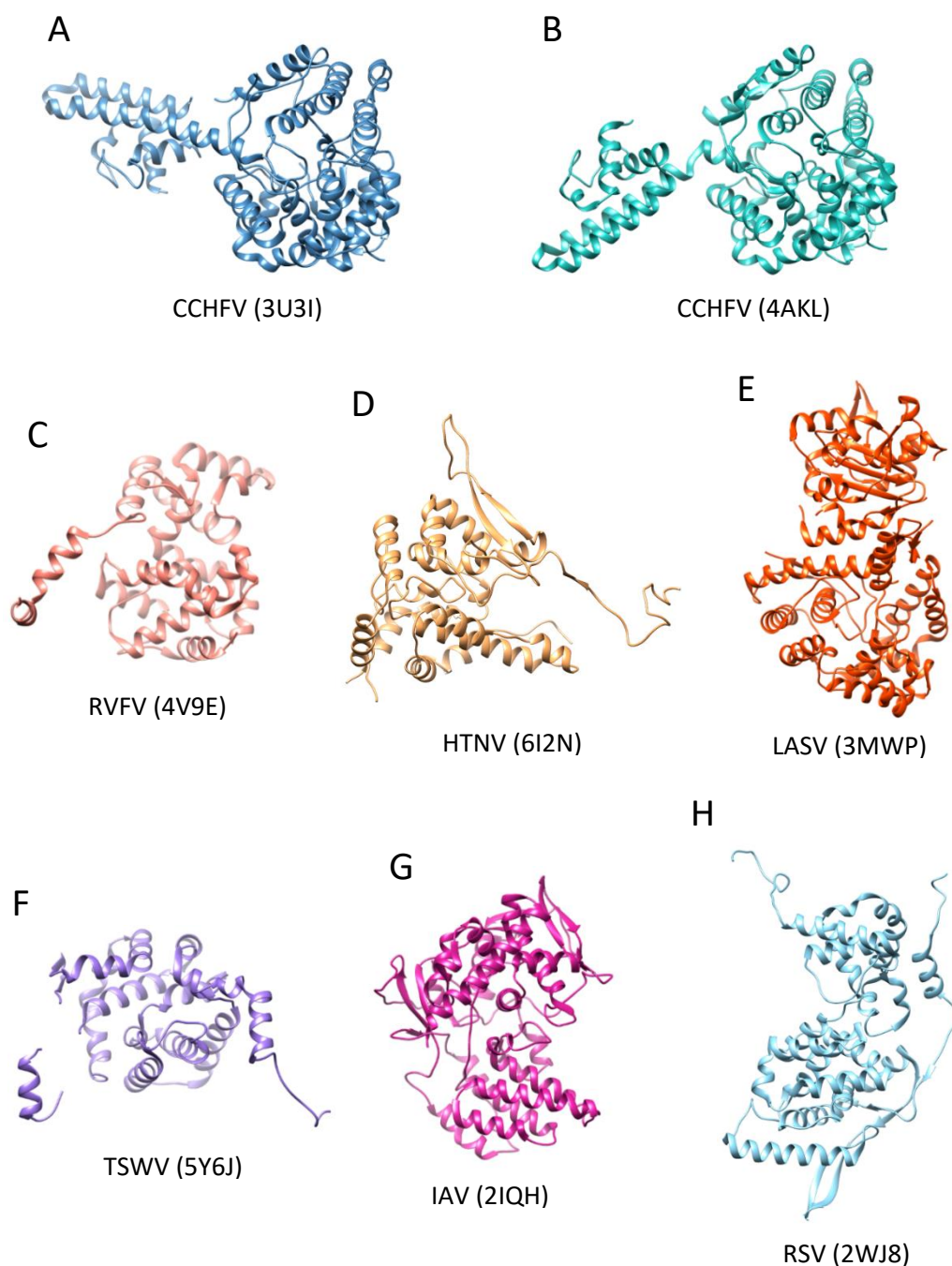


**Figure 1.8:** NP crystal structures from negative RNA viruses outside of the orthobunyavirus genus. (A) and (B) are different structures of the orthonairovirus, CCHFV. (C) The phlebovirus, RVFV. (D) The orthohantavirus, HTNV. (E) The arenavirus, LASV. (F) The tospovirus, TSWV. (G) The orthomyxovirus, IAV. (H) The pneumovirus, RSV. Viruses and PDB accession codes are illustrated below their respective structures.

It is noticeable that NP from the five families of human-pathogenic *Bunyvirales* members are either of a relatively small size (orthobunyaviruses and phenuiviruses) or relatively large size (arenaviruses, hantaviruses and nairoviruses)

and it is becoming apparent that these larger NPs also possess additional functions. For the arenavirus NP, in addition to possessing the canonical RNA binding and oligomerisation functions, it also acts as an exoribonuclease, specific for dsRNA, and is reported to bind methylated cap structures that are required for arenavirus transcription (Qi, X. et al., 2010). While the functional role of this cap binding activity within the arenavirus life cycle remains elusive, the exonuclease activity acts as a potent down regulator of the host innate immune response, interfering with RIG-I surveillance, interferon (IFN)-I production and NK cell activation (Jiang et al., 2013; Pythoud et al., 2012; Reynard et al., 2014; Russier et al., 2014; West et al., 2014). Hantavirus NP has also been found to downregulate the host innate immune response by interfering with TANK binding kinase 1 (TBK1), an activator of the IFN response (Cimica et al., 2014), and by preventing phosphorylation of protein kinase R (PKR), which shuts off host cell translation in response to viral infection (Goodbourn et al., 2000; Ravkov et al., 1997).

CCHFV NP has been found to facilitate translation of viral mRNA transcripts dependent on the 5' UTR sequence of the mRNA, but independent of its 3' UTR sequence. A model is proposed in which NP mediates an interaction between the viral mRNA and eIF4G to engage the ribosome on the mRNA. The lack of a poly(A) tail on CCHFV mRNAs prevents their circularisation, as happens for cellular mRNAs, and this major structural difference likely allows NP-mediated translation to select for viral mRNAs specifically (Jeeva et al., 2017). A very similar mechanism of NP-augmented translation of viral mRNA has also been described for hantaviruses, based on studies of Sin Nombre virus (SNV). However, this mechanism is more direct and involves NP binding to the 5' UTR of the viral mRNA, or to ribosomal protein S19. Homotypic NP interactions then occur between mRNA-bound NP and S19-bound NP and this brings the ribosome and RNA together for initiation of translation (Ganaie et al., 2014; Haque & Mir, 2010).

### 1.10.2 Influenza virus and *Mononegavirales* NP

Structural information is available for many other negative RNA viruses from outside of the *Bunyavirales* group, and such data from the segmented influenza viruses and non-segmented *Mononegavirales* is perhaps the most relevant here. IAV NP has a tail loop to mediate oligomerisation, as well as a groove lined with basic residues, which are conserved across Influenza A, B and C viruses (IBV, ICV) and which is likely to be the site of RNA binding (Ye et al., 2006). IBV NP was found to be structurally similar, and exhibits the same RNA binding groove and oligomerisation-mediating loops (Ng et al., 2012), and the recently identified influenza D virus (IDV) was found to possess the same overall structure, although its oligomerisation loop is at the C-terminus, rather than the N-terminus where it is found in IAV and IBV (Donchet et al., 2019).

Other examples of NP structures come from the *Mononegavirales*, which are non-segmented single-strand RNA viruses. Although the folds within these proteins differ from any NP from the *Bunyavirales*, the overall structure is similar, with the proteins formed predominantly from  $\alpha$ -helices, and containing two lobes, an RNA binding groove and oligomerisation arms at its termini (Albertini et al., 2006; Green et al., 2006; Kirchdoerfer et al., 2019; Rudolph et al., 2003; Sugita et al., 2018; Tawar et al., 2009).

## 1.11 Oligomerisation of orthobunyaviral NP

When overexpressed, NP of various orthobunyaviruses exists in a range of oligomeric states, both in solution and in their crystal structures. It is unclear what the physiological relevance of these oligomers is and, as will be described in section 1.12.1, no observed orthobunyaviral RNPs exhibit a width greater than that of a tetramer. However, the oligomeric promiscuity of orthobunyaviral NP may be relevant

to the assembly and disassembly of RNPs and in the assembly of associated structures such as tubular virus factories in the Golgi apparatus (section 1.8.5).

The EM-derived class averages of BUNV NP show that it can assemble into tetramers, pentamers and hexamers (Li, B. et al., 2013). Analysis by mass spectrometry (MS) confirmed that BUNV N could form these oligomeric species, as well as trimers, when bound to RNA, but that the apo protein was monomeric. (Shepherd et al., 2014). The same MS study also found that SBV N can exist as a monomer, tetramer or pentamer when RNA-free, but can adopt a range of oligomeric states between trimer and dodecamer when RNA-bound, in agreement with the hexameric crystal structure (Dong, H., Li, P., Elliott et al., 2013) For OROV larger oligomers have also been observed by EM, which the authors state correspond to heptamers and octamers (Murillo et al., 2018). In the crystallographic studies of LACV NP a large, helical oligomer was observed, which is relevant to the following section

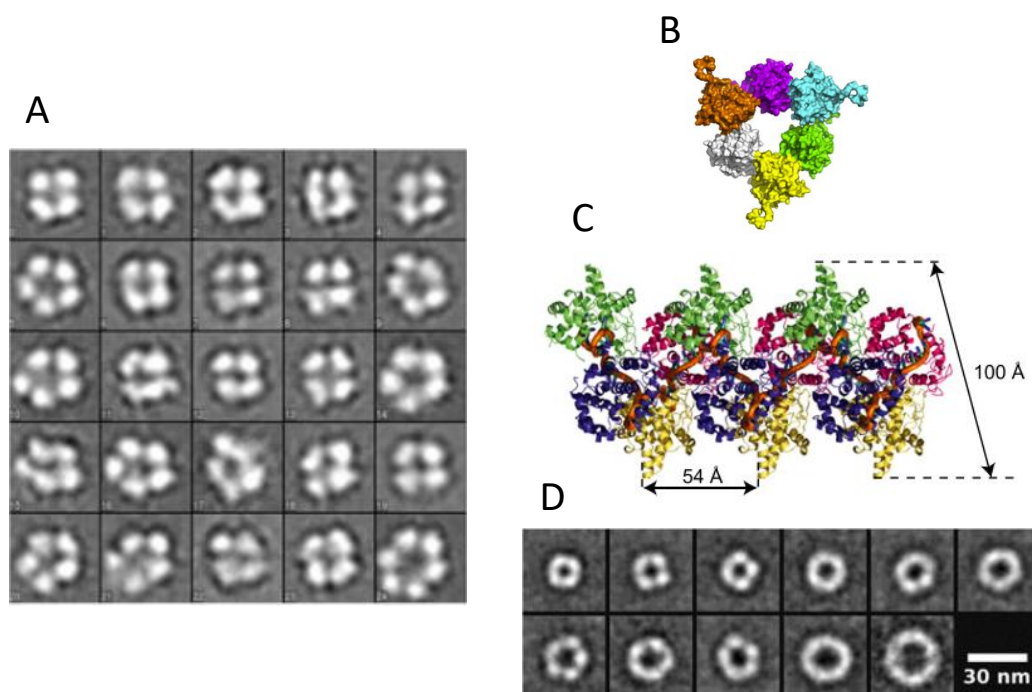


**Figure 1.9:** Oligomeric states observed for orthobunyavirus NP. (A) Class averages of BUNV NP in solution, adapted from (Li, B. et al., 2013). (B) Hexameric form of crystallised SBV NP, adapted from (Dong, H., Li, P., Böttcher et al., 2013). (C) 4<sub>1</sub> helical form of LACV NP, adapted from (Reguera et al., 2013) (D) Class averages of OROV NP in solution, adapted from (Murillo et al., 2018).

(1.12.1) and its discussion of the helical nature of orthobunyavirus RNPs. The wide range of oligomers that bunyaviral NP can form illustrates the wide range of conformations that NP oligomerisation arms can adopt. This in turn speaks to the great degree of flexibility within the oligomerisation domains and the great flexibility that NP oligomers exhibit, which is likely to be an essential characteristic for their transition from monomers or planar oligomeric rings, to higher order RNPs.

## 1.12 Ribonucleoproteins (RNPs)

### 1.12.1 Orthobunyavirus RNP structure

Negative stain micrographs have been published of the virion-derived RNPs of several different orthobunyaviruses and other members of the *Bunyavirales*, illustrating the gross, overall morphology of these complexes and highlighting the differences within and between genera. Higher resolution cryo-EM derived structures are available of the RNPs of other negative sense RNA viruses such as IAV and the *Mononegavirales*.

The published micrographs of orthobunyavirus RNPs led to conflicting hypotheses on their overall architecture. Two such studies, one in support of each hypothesis, present RNPs of BUNV. The first study isolated and purified RNPs from BUNV virions and from the resulting micrographs concluded that BUNV RNPs are circularised and have a helical conformation and a constant width of 10 nm, corresponding to the width of two NP monomers, or one side of a tetramer (Ariza et al., 2013). This led the authors to conclude that the BUNV RNP is helical and consists of a repeating, four monomer unit with a positively charged RNA binding groove running through the length of its interior, protecting the negative sense RNA segment. At the same time, a second group published a micrograph displaying BUNV virions spilling their RNPs following membrane disruption and concluded that the RNPs were

5 nm in width, corresponding to a single NP monomer (Li, B. et al., 2013). The authors proposed that the overall architecture of the RNP has a much looser, flexible ‘beads on a string’ architecture built from monomeric NP, in which NP molecules contact others solely through their flexible terminal arms. However, a closer inspection and the use of ImageJ to measure the scale bar and then the width of the RNP actually produces a value of 8 nm. This figure was provided earlier as the length of one side of the crystallised BUNV NP tetramer, which puts the micrograph at odds with the author’s interpretations and more in agreement with the opposing hypothesis.

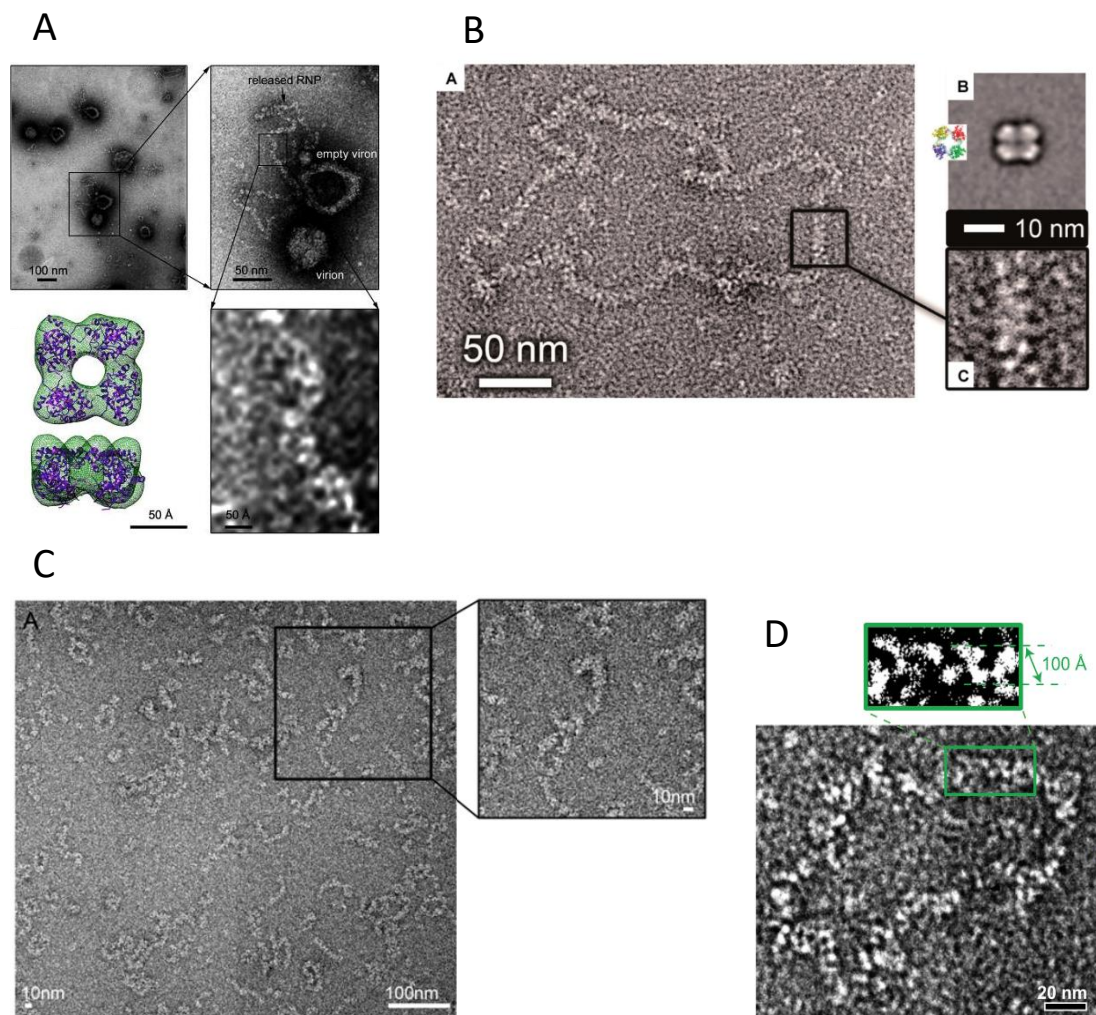


**Figure 1.10:** Available micrographs of negatively stained orthobunyavirus RNPs. (A) and (B) RNPs released from BUNV virion, adapted from (Ariza et al., 2013; Li, B. et al., 2013). (C) RNPs reconstituted from recombinant LEAV NP, adapted from (Niu et al., 2013). (D) RNPs released from LACV virions, adapted from (Reguera et al., 2013). In all figures insets show detail of filament morphology.

Micrographs of LEAV RNPs were also presented and stated to support the 'beads on a string' model, with 'beads' of monomeric NP threaded onto the viral RNA (Niu et al., 2013). The RNPs presented here were derived from bacterially expressed LEAV NP and so their biological relevance is not certain; they were assembled with an absence of circularised viral RNA and host cell proteins, which may be important for correct RNP assembly. As in (Li, B. et al., 2013) the authors state that the RNPs have adopted a 'beads on a string' architecture but again, from a closer inspection of the micrographs and their scale bars, these RNPs are roughly 10 nm wide; the width of an NP tetramer. Indeed, an alternating pattern of monomers implying a helical arrangement are apparent in some LEAV RNPs, as previously visualized for BUNV (Ariza et al., 2013) and in apparent disagreement with the authors' interpretation.

One paper described a more sophisticated model of orthobunyavirus RNP structure based on RNPs purified from virions and analysed by negative staining (Reguera et al., 2013). This paper proposed that the overall structure of LACV RNPs is a helix with a four monomer repeating unit, similar to that described for BUNV (Ariza et al., 2013). Additionally however, a supercoiled form of the LACV RNP was described, which may represent a condensed form that is required for packaging of the three LACV segments into a single virion. Conversely, they also observed uncoiling of the ~10 nm wide RNPs to what could be described as a 'beads on a string' architecture upon heating to 37°C. This unwinding at a physiologically relevant temperature could suggest a mechanism in which the RNP unwinds to adopt a highly flexible conformation, perhaps to facilitate access of the RdRp during transcription and replication.

The various structural states of the orthobunyavirus RNPs observed and described to date raise several questions: First, it remains to be determined whether the ~10 nm wide RNPs extracted from virions are in fact helical. Second, there is no information regarding the structural basis for the transition between compact and

flexible states, as well as the biochemical trigger required for this transition to occur. In addition, it is unknown whether the different models described above represent functional RNP conformations required for different stages of the viral replication cycle. Although some doubts arise concerning the stated widths of supposed 'beads on a string' shaped RNPs, this model of the orthobunyavirus RNP cannot be discounted. As described above, a compact helical RNP may undergo a transition to a looser architecture such as 'beads on a string' to facilitate polymerase access to the RNA, and the micrographs of LACV RNPs at 37°C clearly show what appears to be the wider RNP transitioning to a narrower, looser state.

### 1.12.2 Other bunyaviral RNPs

The highest resolution structural information of bunyaviral RNPs comes from a cryo-EM derived model of the RNP of HTNV, which was derived from recombinantly expressed NP in complex with RNA, and formed a highly ordered, helical structure (Arragain et al., 2019). The helix has 3.6 subunits per turn, in keeping with previous findings that hantavirus NP trimerises (Alfadhli et al., 2001; Kaukinen et al., 2004). Within the helix each NP monomer interacts with six others. Direct neighbours bind each other through interactions of the C- and N-terminal arms with the core of neighbouring proteins. The C-terminal arm buries in a hydrophobic pocket on one neighbour, and the N-terminal arm forms a three-stranded  $\beta$ -sheet with two  $\beta$ -strands on the other neighbour. The other homotypic NP interactions act across more distant monomers. Taking a hypothetical monomer in the helix as  $NP_x$ , then  $NP_{x+2}$  and  $NP_{x+3}$  have their own interaction with each other through their C-termini, and a  $\beta$ -hairpin on  $NP_x$  acts as a 'clamp' to secure this interaction. These inter-NP interactions along the long axis of the RNP filament are likely to be important for maintenance of the helix, and would need to be disrupted for polymerase access to the RNA, as the authors propose in their model of HTNV replication and transcription. The high resolution of

this RNP structure, and resulting insight into how a helical conformation is stabilised, may help to understand how a possible helical orthobunyaviral RNP is maintained.

In contrast to the helical HTNV RNP, other structural information on bunyaviral RNPs is of a low resolution. Other data on hantavirus RNPs, which was recapitulated by the helical model, comes from cryo-ET of intact hantavirus particles. Dense rods were visualised within virions which were attributed to RNPs, and which clearly exhibited a straight and rigid structure that would be compatible with a helical shape (Battisti et al., 2011; Huiskonen et al., 2010).

EM analysis of RNPs from other segmented RNA viruses has revealed a range of different architectures, from the completely unstructured 'beads on a string' arrangements, to rigid and helical architectures. RNPs from the phlebovirus RVFV are string-like and highly disordered, exhibiting no discernible helical architecture (Raymond et al., 2010). Interestingly, RNase treatment of these RNPs and heating to 37°C released oligomeric rings of tetrameric, pentameric and hexameric NP. Additionally, incubating recombinantly expressed RVFV NP with in vitro transcribed RNA produced RNPs that looked very similar to those purified from virus. Similarly disordered RNPs with no helical characteristics could be reconstituted from another phlebovirus, TOSV (Baklouti et al., 2017; Olal et al., 2014). However, crystal structures reveal that for TOSV, RNA binding by NP hexamers causes monomers to shift relative to each other at the 5' RNA end. This essentially creates a small 'step' up, which when extended gives rise to a left-handed helix. This is a likely mechanism of RNP formation, but this would give rise to a more ordered, helical RNP than those observed by EM (Olal et al., 2014).

RNPs from within virions of the orthonairovirus CCHFV can exhibit both a very disordered conformation like RVFV, but also a more rigid helical structure, as shown in the two panels in figure 1.11B (Wang, X. et al., 2016). This potentially represents similar findings to those from LACV, of a clear transition between more and less ordered RNP conformations that possibly function at different stages of the viral multiplication cycle. Further evidence for a helical structure of CCHFV RNPs comes from X-Ray crystallography and the observation that conformational changes in CCHFV NP facilitate the formation of superhelices which can then dimerise to form an antiparallel double helix (Wang, Y. et al., 2012).

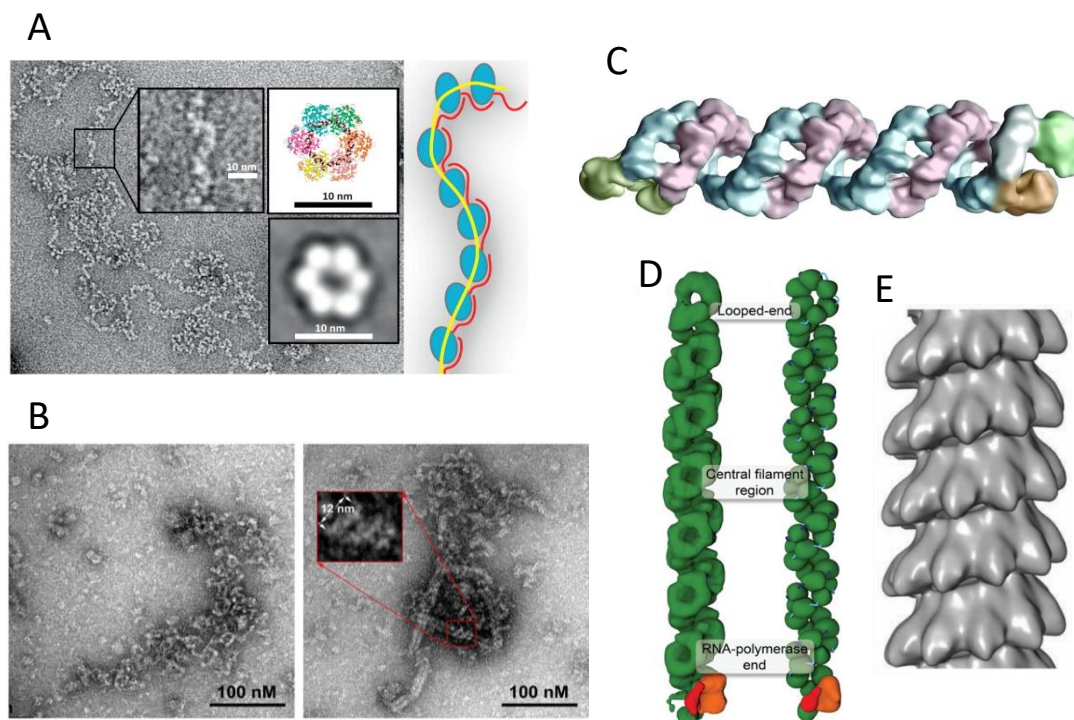


**Figure 1.11:** RNPs of viruses outside of the orthobunyavirus genus. **(A)** The phlebovirus, RVFV, adapted from (Raymond et al., 2010). **(B)** The orthonairovirus, CCHFV, adapted from (Wang, X. et al., 2016). **(C)** and **(D)** conflicting structures of the IAV RNP, adapted from (Arranz et al., 2012; Moeller et al., 2012) **(E)** Cryo-EM structure of the RSV nucleocapsid (Tawar et al., 2009).

### 1.12.3 Non-bunyaviral RNPs

Influenza virus is the best studied of all segmented, negative sense RNA viruses, and in turn their RNPs are the best characterised, with direct observation of IAV RNPs dating back to the late 1960s (Pons et al., 1969). IAV RNPs appear as a distinctive rod-like double helix, with a loop at one end and the heterotrimeric polymerase complex bound to the opposite end. Initial 3D models of the IAV RNP utilised a mini-genome system to produce small, circular RNPs comprising just 9 NP molecules (Coloma et al., 2009). From these it was possible to dock the atomic model of NP derived from crystallography into the EM map, and show how NP monomers interact with each other while bound to RNA, and how they interact with the polymerase subunits (Area et al., 2004; Martín-Benito et al., 2001). Later cryo-EM reconstructions confirmed the details of the double helix (Arranz et al., 2012; Moeller et al., 2012).

Non-segmented RNA viruses such as the *Mononegavirales* have very different RNPs that assemble into long (up to 20 kb) and more ordered nucleocapsid structures, which act as scaffolds for all aspects of viral assembly. These complexes, such as the nucleocapsids of respiratory syncytial virus (RSV) and vesicular stomatitis virus (VSV), are characteristically helical and very rigid. This permits helical reconstruction analysis to be performed and generate high-resolution structures, in the region of 4 to 10 Å resolution (Ge, P. et al., 2010; Gutsche et al., 2015; Tawar et al., 2009; Wan et al., 2017).

The work by Reguera et al. (2013) on LACV presents interesting insights into how the architecture of orthobunyavirus RNPs changes drastically to accommodate essential processes such as unwinding for transcription and replication and condensing for genome packaging into nascent virions. It is likely that this model of RNPs which transition between multiple conformations with varying degrees of

flexibility is the most accurate, as it fits all of the requirements which must be met by the RNP structure during the course of the virus replication cycle.

## **1.13 Transmission electron microscopy (TEM)**

### **1.13.1 Principles of TEM**

Transmission electron microscopy (TEM) is the technique of transmitting electrons through a sample to generate a projection image from the resulting interaction of the electrons with the specimen (Both the technique and the machines themselves; transmission electron microscopes, are abbreviated to TEM). The short wavelength of an electron beam (picometres) allows TEMs to obtain information at a significantly higher resolution than a light microscope. Data collected on current state-of-the-art microscopes can be used to produce structures at atomic-resolution (Bartesaghi et al., 2018; Merk et al., 2016).

From the top down a TEM consists of an electron source often referred to as a gun, a series of electromagnetic lenses to focus the electron beam, a sample holder and a system for electron detection (figure 1.12). The electron source is typically a tungsten filament or a single crystal of lanthanum hexaboride ( $\text{LaB}_6$ ), which is connected to a high voltage source (between ~100 and ~300 kV). The current generated in the gun causes the emission of electrons, either due to high temperature exciting the electrons (thermionic emission) or an extremely high potential difference between two electrodes (field emission). Many of the highest-resolution structures deposited in the EMDB were produced with the aid of microscopes operating at 300 kV, but near-atomic-resolution structures have been determined with microscopes operating at 200 kV (Campbell, M. G. et al., 2014; Herzik Jr et al., 2017). Higher accelerating voltages increase the penetration of the electrons, but at the cost of reduced contrast (Orlova & Saibil, 2011).

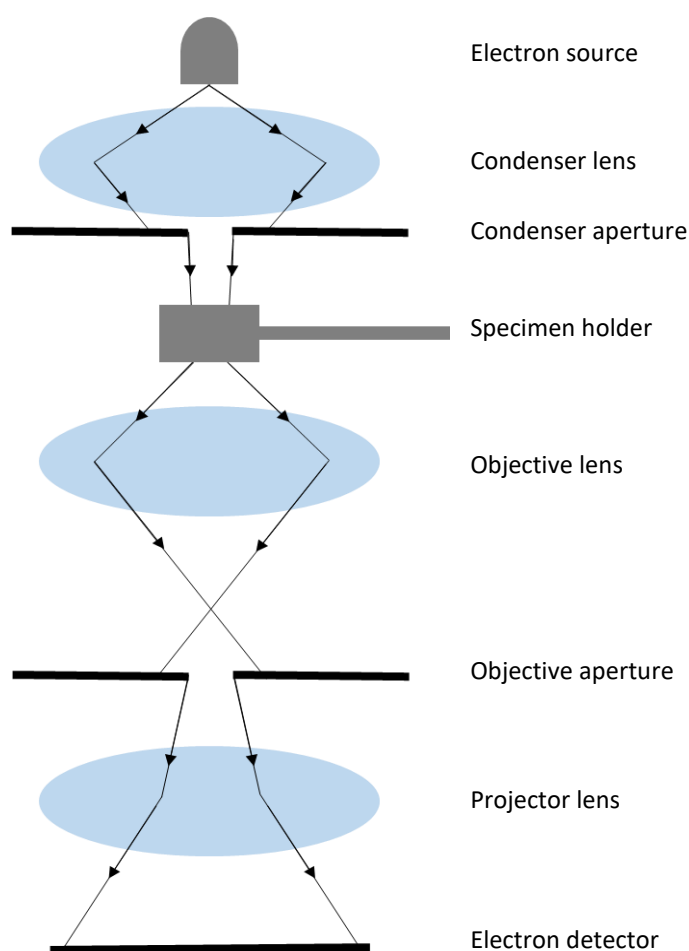


**Figure 1.12:** Schematic of a typical TEM. Thin lines and arrows indicate the path of the electron beam down the microscope.

A series of electromagnetic fields are shaped precisely by magnets to produce lenses which focus the electron beam much like a glass lens focuses a beam of visible light. Typically, there are three lenses in a TEM; the condenser lens shapes the initial electron beam and focuses it onto the specimen, the objective lens focuses the beam as it passes through the specimen, and the projector lens expands the beam onto the electron detection system to produce an image. A series of apertures filters out aberrant electrons and maintains the coherence of the beam. These consist of metal plates with a hole in the centre and permit the passage of electrons along the optical axis while excluding those a certain distance from this axis.

TEMs are operated under vacuum conditions to minimise the interaction of the electron beam with gas atoms. A cold trap consisting of a copper rod cooled to LN<sub>2</sub> temperatures may also be used to adsorb gases such as water vapour and condense them on the trap surface, preventing them from contaminating the grid. The vacuum within the microscope column poses the problem of biological samples rapidly dehydrating and being damaged, and necessitates the use of techniques to preserve the integrity of the sample such as fixing in a heavy metal stain or in vitreous ice (Scarff et al., 2018).

One of the biggest challenges in high-resolution EM is radiation damage to the specimen. Electrons are scattered from the specimen in two ways; elastic and inelastic. Elastic scattering occurs when the path of an electron is altered with no accompanying energy loss, while inelastic scattering involves the transfer of energy from the electron. This energy transfer causes damage by the ionization of the sample and breaking of bonds, and generates ions and free radicals that cause further downstream damage (Baker, L. A. & Rubinstein, 2010; Henderson, 1995). This effect is mitigated to some extent by negative staining and by vitrification but is still a problem that must be accounted for, particularly in high voltage cryo-EM where the high energy electron dose applied to the sample must be carefully controlled.

### **1.13.2 Electron detection**

One of the most important factors in the recent, rapid advance in the resolution which can be achieved with EM is the improvement in electron detection systems. The overall efficiency of a detector can be expressed as the detective quantum efficiency (DQE), which is simply defined as the ratio of output signal-to-noise ratio (SNR) to input SNR. Early EM used photographic film to record scattered electrons, which offered a large number of pixels with a small pixel size, set by the size of the silver halide crystals coating the film. However, the main disadvantage of film is the need to remove the film from the microscope and scan it

for digitisation and analysis, which slows down data processing and results in the loss of information. Charge coupled devices (CCDs) provide a much quicker readout than film, but have a lower DQE (McMullan et al., 2009). Incident electrons are detected on a phosphor screen, converted to light and optically transferred to the CCD.

The most advanced electron detections systems available are direct electron detectors (DEDs) such as the Gatan K2 Summit and FEI Falcon II which are monolithic active pixel sensors (MAPS). These detectors detect the voltage drop across a capacitor when it is struck by an electron. DEDs combine the speed of a CCD with the high DQE of film and their high frame rate allows them to produce movies by capturing multiple frames in the same field of view. This allows the electron dose to be spread across the multiple frames, and allows correction of beam-induced motion in the sample. Most DEDs can operate in both integrating mode and counting mode. In integrating mode the total signal of all electrons encountered in a frame are combined, while in counting mode individual electrons are counted upon interacting with the detector. Counting mode therefore has a higher DQE and can facilitate sub-pixel positioning of electrons but must be used with a low electron dose and longer exposure times. Consequently, although integrating mode has a lower DQE it allows faster data acquisition and thus is less affected by specimen drift.

### **1.13.3 Negative staining**

Negative staining is a commonly used method of preserving biological material for TEM. Samples are adsorbed to the surface of a mesh grid typically made from copper, which has a thin coating of carbon on one side. Fixation of the sample and staining is achieved by the subsequent deposition of a heavy metal salt such as uranyl acetate (used at 1 or 2% (v/v)) or uranyl formate onto the grid. The stain acts by absorbing electrons and providing contrast to the sample through which electrons pass. This technique produces low-resolution data as many features of the molecule

below the stain are obscured, but permits the rapid, inexpensive collection of data and provides much higher contrast than cryo-EM. If computational alignment and averaging is used then the amount of information gained from negative staining can be increased significantly and 3D reconstructions can also be determined by this method, but are generally limited to approximately 20 Å resolution.

#### **1.13.4 Cryo-EM**

A detailed discussion of the theory and methodology of cryo-EM is beyond the scope of this project, in which cryo-EM was used in a very limited capacity. However, a brief discussion of it is prudent, both as an introduction to cryo-ET which was used extensively, and because some cryo-EM data were collected and are presented here.

Cryo-EM utilises the vitrification of a sample within ice by plunging into liquid ethane (Thompson, R. F. et al., 2016), to offer protection from radiation damage and to preserve it in a near-native state. Recent advances in electron detectors combined with the availability of very stable 300 kV microscopes such as the Titan Krios (FEI) and CryoARM (JEOL) has led to the solution of cryo-EM structures at atomic-resolution, and placed the technique alongside X-ray crystallography and nuclear magnetic resonance (NMR) spectroscopy as an extremely powerful and important piece of the structural biologist's toolbox.

As of 2019, several impressive reconstructions below 2 Å resolution are amongst the highest-resolution cryo-EM structures available. These include; the highest-resolution structure in the EMDB, apoferritin at 1.54 Å from Keiichi Namba's group (University of Osaka, Japan) (EMD-9865) (unpublished); the highest-resolution non-apoferritin structure in the EMDB, a 1.8 Å structure of glutamate dehydrogenase (Merk et al., 2016); and the highest-resolution whole-virus structure, an adeno-associated virus at 1.86 Å (Tan, Y. Z. et al., 2018). Additionally, a 1.54 Å

reconstruction of a virus was reported by Craig Yoshioka (Oregon Health & Science University, USA) in 2018 but has not yet been released.

The high-resolution of these structures was achieved by single particle analysis (SPA) or helical reconstruction. The mathematic, computational and physical principles underpinning these techniques will not be discussed here. Briefly however, for the sake of a complete summary of EM, SPA relies on a protein or macromolecular complex randomly adopting multiple conformations within the layer of ice it is vitrified within. The resulting micrographs collected will contain many copies of the particle being studied, at (ideally) all possible orientations. The projection-slice theory posits that the Fourier transform of a 2D projection of a 3D molecule in real space (i.e. a single orientation of a protein within a micrograph) is a 2D slice through the centre of the 3D Fourier transform of the molecule. Therefore, if micrographs are produced of a molecule at multiple orientations and the direction of these projections is known then the 3D Fourier transform of the molecule can be reconstructed, and from this the application of an inverse Fourier transform will produce the original 3D structure (Cheng, Y. et al., 2015). Helical reconstruction follows the same principles but relies on the fact that individual subunits along a helix are also different orientations of the subunit (Egelman, 2007).

#### **1.13.5 Cryo-electron tomography (cryo-ET)**

Cryo-electron tomography is a specialised form of EM in which a sample is imaged in one location but tilted at a series of different angles. This generates a series of 2D images which can be combined into a 3D reconstruction. Identical particles within a tomogram can be extracted, aligned and averaged as in SPA to increase SNR and resolution in a process called sub-tomogram averaging (STA). Although the highest-resolution structures obtained by STA are around  $\sim 4$  Å (Mattei et al., 2018), fewer than half of the structures deposited in the EMDB are above 28 Å resolution, and only  $\sim 10\%$  are above 12 Å resolution. The highest resolution structure of a viral

surface glycoprotein is that of LASV, which at 13.6 Å resolution allows the fitting of crystal structures and the visualisation of a conformational change relative to a different, 16 Å structure (Li, S. et al., 2016).

#### **1.13.6 Tilt series**

After an area of the grid has been selected from which to collect cryo-ET data, images are collected at a range of different tilt angles; typically  $-60^\circ$  to  $+60^\circ$ . Collecting multiple images of the same part of the grid increases the risk of radiation-induced damage to the sample so to mitigate this the microscope is operated in low-dose mode. The low electron dose leads to low contrast and SNR but this can be improved by the use of a phase plate which introduces phase shift to increase contrast. This allows the collection of data closer to in-focus and results in lower SNR (Danev & Baumeister, 2016). An unavoidable problem of cryo-ET is the missing wedge problem in which information is lost due to the physical limits of how far the specimen holder can tilt, resulting in stretching of the reconstruction in the Z axis (figure 1.13). Collecting a dual-axis tilt series can reduce the missing wedge of information to a smaller missing pyramid, and STA can also reduce the stretching effects of the missing information.

#### **1.13.7 Tomogram reconstruction and sub-tomogram averaging (STA)**

The first step in generating a 3D tomogram is to accurately align the component images of the tilt series. This alignment is generally carried out with the aid of gold fiducial markers. These markers are highly electron dense and are distributed throughout the sample and can be automatically detected by tomogram reconstruction software. The fiducial markers are used to determine the shifts between each image and allow the individual 2D images within the tilt series to be placed within a 3D volume.

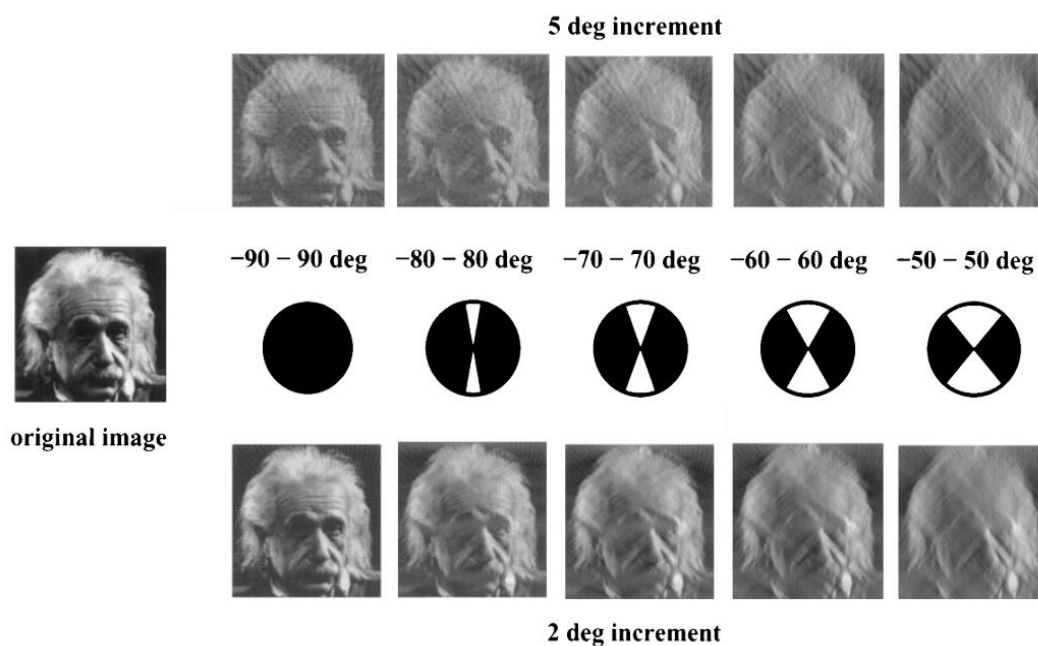


**Figure 1.13:** Illustration of the missing wedge problem and the effect it has on the final reconstructed tomogram. Reproduced from (Koster et al., 1997)

Generation of the 3D tomogram following alignment is achieved by weighted back projection (figure 1.14A). Within a reconstructed tomogram multiple instances of the complex of interest can be extracted. The orientation of the extracted sub-tomogram is refined iteratively similarly to SPA, but in 3D rather than 2D. Averaging the aligned copies of the extracted sub-tomogram can be used to increase the resolution of the complex of interest (Zhang, P., 2019) (figure 1.14B).

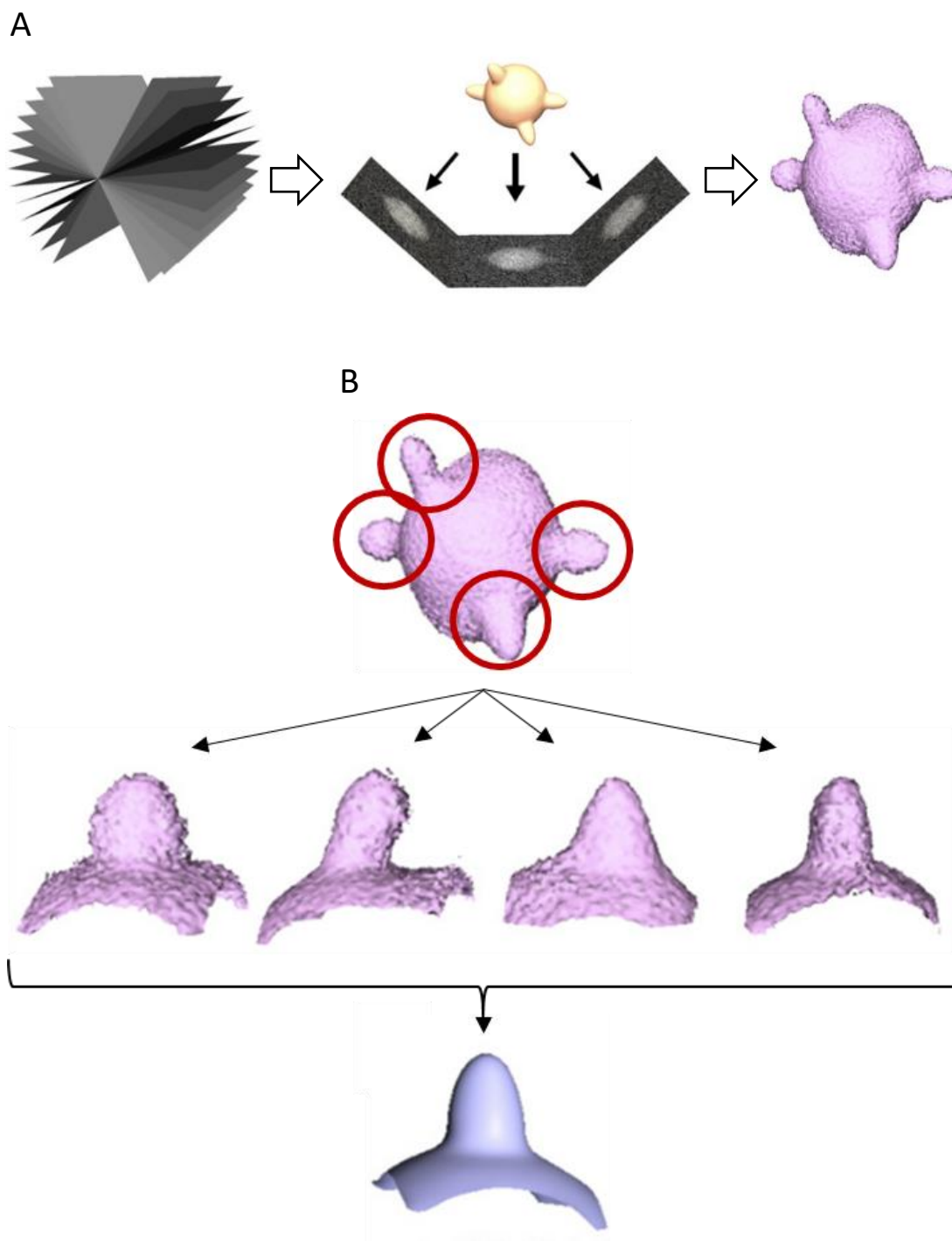


**Figure 1.14:** Schematic of tomogram reconstruction and STA. **(A)** Images are collected at a range of angles around a central point (left) and the projection recorded at each angle (middle) is used to build a 3D model (right). **(B)** Small areas of interest (sub-tomograms) (top, circled in red) are isolated from the 3D model (middle) and aligned and averaged to improve SNR and resolution (bottom). Adapted from (Subramaniam et al., 2007).

### 1.14 Aims of the project

Previous work within the field of segmented negative strand viruses has presented conflicting models describing the ultrastructure of native orthobunyavirus RNPs. The overarching aim of this PhD project was to resolve this conflict by investigating the ultrastructure of BUNV RNPs using EM, specifically to determine whether they adopt either a flexible architecture with NP monomers interacting solely through flexible terminal arms, or alternatively with NP arranged as a highly ordered helical structure.

Within this overall aim, the first project objective was to optimise a protocol for the generation, harvesting and purification of BUNV virions in high concentrations, followed by the extraction and purification of RNPs, and their subsequent visualization using negative stain EM in order to characterise their gross morphology. In parallel, attempts were made to reconstitute RNPs from recombinant NP and *in vitro* transcribed RNA, and to compare the resulting assembled RNP complexes to virion-derived RNPs.

Having determined which of the two models of RNP architecture best described BUNV RNPs, the second and final project objective was to establish a 3D model of this architecture. Part of the negative stain characterisation of RNPs would involve establishing optimum conditions for EM analysis, which could then be taken forward to cryo-EM analysis. At the beginning of the project due to the narrow width, high flexibility and uncertainty over their exact architecture, it was unknown if cryo-EM analysis would take the form of cryo-ET, SPA or helical reconstruction, but this information would be elucidated through the negative stain studies.

## **Chapter 2**

### **Materials and methods**

#### **2.1 Tissue culture and virological techniques**

##### **2.1.1 Cell and virus stocks**

Sub-confluent hamster-derived BHK-21 cells and human-derived SW13 cells were both maintained in 'complete media', which consisted of Dulbecco's Modified Eagle Medium (DMEM) (Sigma-Aldrich) supplemented with 10% foetal bovine serum (FBS) and 5% penicillin/streptomycin (Sigma-Aldrich). Both cell lines, when uninfected, were incubated at 37°C with 5% CO<sub>2</sub>. Low-passage number, healthy cells were regularly expanded from frozen stocks to replace cells which had been passaged extensively. Details of how cells were handled upon viral infection are described below.

##### **2.1.2 Virus propagation**

BHK-21 cells at 70-80% confluency were infected with BUNV at a multiplicity of infection (MOI) of 0.01. In theory, this means that for every cell in the flask 0.01 infectious virus particles was added, or more simply that one infectious virus particle was added per 100 cells. An appropriate volume of virus stock for this MOI was diluted into 3 ml of serum free-media which consists of only DMEM and penicillin/streptomycin. After washing the cells twice with sterile phosphate buffered saline (PBS) the 3 ml inoculum of virus was added directly to the cells and this was incubated at 32°C for three hours with occasional rocking. Following this the flask

was topped up with serum-free media to the minimum volume required to cover the cell monolayer, approximately 11 ml for a T175 cell culture flask. Maintaining the infected cells in the smallest possible volume of media maximised the number of flasks from which supernatant could be aspirated and loaded into an ultracentrifuge; the volume of the ultracentrifuge being the limiting factor for how much virus was purified. Flasks of infected cells were incubated for three days at 32°C with twice daily rocking to facilitate the infection of the entire cell monolayer and amplification of the virus prior to purification. Incubation at the slightly lower temperature slowed cell growth to aid the survival of the cells for three days in media lacking serum.

### **2.1.3 Virus purification**

Supernatant was aspirated from infected cells three days post-infection and centrifuged at 3700 *g* for 20 minutes to pellet cellular debris. The supernatant was passed through a 0.45 µm filter and centrifuged for a further 20 minutes at 3700 *g* before loading into 38 ml Open-Top Thinwall Ultra-Clear ultracentrifuge tubes (Beckman-Coulter). Tubes were each loaded with 30 ml of the clarified supernatant and underlaid with 7 ml of sterile filtered 30% D-sucrose (Fisher Scientific) that had been prepared in TNE buffer (100 mM Tris-HCl, 200 mM NaCl, 0.1 mM ethylenediaminetetraacetic acid (EDTA), pH 7.4) supplemented with EDTA-free Protease Inhibitor Cocktail (Roche). Tubes were placed into the appropriate buckets for loading into an SW32 rotor (Beckman-Coulter) and centrifuged in a Beckman-Coulter XPN-80 ultracentrifuge at 100000 *g* for three hours at 4°C, before deceleration with a low brake. The supernatant and cushion were discarded after samples had been taken for SDS-PAGE and the tubes allowed to air dry for approximately five minutes. The pellet was then resuspended overnight in 100 µl of TNE buffer with protease inhibitors as described above, with gentle rocking at 4°C. If the purified virus was not required immediately following resuspension then a

sample was taken to confirm purity by SDS-PAGE and the remainder was divided into small aliquots, flash frozen in liquid nitrogen (LN<sub>2</sub>) and stored at -80°C.

#### **2.1.4 Plaque assay**

The titre of infectious BUNV was determined by plaque assay carried out in SW13 cells that had been seeded into 12-well plates at an appropriate density for ~80% confluency at the start of the plaque assay. To determine virus titre, serial dilutions were made in serum-free media from 10<sup>-1</sup> to 10<sup>-5</sup>. Wells were inoculated with 200 µl of diluted virus such that a 12-well plate contained two wells of each dilution and two mock infected wells to which only serum free media was added. After incubation for one hour at 37°C the inoculum was aspirated and the cells overlaid with a 1:1 mixture of complete media and 1.6% (w/v) methyl-cellulose (MC). The mixture of media and MC is so viscous that when progeny viruses are released following the lysis of infected cells, their movement through the supernatant is limited, and thus virus spread is to neighbouring cells only. This leads to the formation of localised areas of cell death or 'plaques', which can be observed and which represent the outcome of a single initial infection event. The infected cells and their overlay were incubated at 37°C for six days before the overlay medium was aspirated and the cells were washed once with sterile PBS. Cells were fixed in 10% paraformaldehyde for one hour and then stained by the addition of 0.1% (w/v) crystal violet and 20% (v/v) ethanol to each well, which both fixed the cells and stained them a dark purple. If the viral titre was so high that individual plaques could not be distinguished or counted at the 10<sup>-5</sup> dilution then the assay was repeated with further serial dilutions. When the number of plaques in a single well could be clearly counted this was multiplied by the dilution factor to give the number of plaque forming units (PFU) per ml. This provided a metric for the number of infectious virions in the sample and allowed the calculation of the correct volume of a virus stock needed to infect cells at a specific MOI.

## 2.2 RNP purification

RNPs were isolated by continuous density gradient centrifugation with OptiPrep™ (Sigma-Aldrich), an iso-osmotic, non-ionic and metabolically inert iodixanol-based continuous density gradient medium. OptiPrep™ was prepared to final concentrations of 10, 15, 20 and 25% in TNE buffer. To form gradients 900 µl of 25% OptiPrep™ was added to a 4 ml Open-Top Thinwall Ultra-Clear ultracentrifuge tube (Beckman-Coulter) and frozen quickly with dry ice. Onto this, 900 µl of the 20% OptiPrep™ was added and frozen and this process was continued until a 3.6 ml gradient was formed. Incubation overnight at room temperature allowed the diffusion of the OptiPrep™ and the formation of a continuous density gradient. Frozen virus suspensions prepared as described previously were thawed and incubated at 4°C for one hour with TNE buffer containing 1% Triton X-100 (Sigma-Aldrich) and 0.1% NP-40 Alternative (Calbiochem), a non-ionic surfactant sold as an alternative to the now discontinued Nonidet™ P-40, to ensure complete disruption of virion membranes and release of RNPs. This was then layered gently onto the top of the prepared 10-25% OptiPrep™ gradient and the tube was placed into an appropriate bucket for loading into an SW60 rotor (Beckman-Coulter) and centrifuged in a Beckman-Coulter XPN-80 ultracentrifuge at 250000 *g* for 1.5 hours at 4°C before deceleration with a low brake.

Following centrifugation, the top 400 µl which has been loaded onto the gradient was aspirated and 200 µl fractions were collected from the top to the bottom of the gradient itself. Samples of each fraction were taken to determine the location of RNPs within the gradient by SDS-PAGE and western blotting for BUNV NP, and also to assess purity by Coomassie staining and negative stain EM. Fractions were either used immediately or flash frozen in LN<sub>2</sub> and stored at -80°C.

It was necessary to remove the OptiPrep™ gradient medium to prepare the optimum sample for analysis by EM and this was achieved through buffer exchange using large molecular weight cut off (MWCO) filtration membranes. RNP-containing fractions, as determined previously, were pooled together and added to a 100 kDa MWCO Vivaspin® 6 centrifugal concentrator (Sartorius), which had been equilibrated with the desired buffer. The concentrator was centrifuged at 3000 g for minute-long intervals and regularly checked to ensure the membrane did not dry out. This continued with the addition of more buffer and further centrifugation until all of the OptiPrep™ had been removed and the desired volume of ~100 µl had been reached. The concentration of OptiPrep™ was estimated by taking small samples and measuring their absorbance at 244 nm, the wavelength of maximum absorption for iodixanol. The RNPs in solution were then removed from the concentrating device and immediately prepared for EM analysis or flash frozen in LN<sub>2</sub> and stored at -80°C.

## **2.3 Protein analysis**

### **2.3.1 SDS-PAGE**

SDS-PAGE gels were prepared as follows: first, a 15% resolving gel was prepared with 5 ml 30% bis-acrylamide, 2.5 ml 1.5 M Tris-HCl pH 8.8, 2.3 ml dH<sub>2</sub>O, 100 µl 10% SDS, 100 µl 10% APS, 10 µl tetramethylethylenediamine (TEMED), and 5 ml of this was poured into a gel cast and allowed to set. This was then overlaid with a 5% stacking gel prepared with 830 µl 30% bis-acrylamide, 630 µl 1.0 M Tris-HCl pH 6.8, 3.4 ml dH<sub>2</sub>O, 50 µl 10% SDS, 50 µl 10% APS, 50 µl TEMED and a comb was inserted. Samples were mixed 1:1 with loading buffer consisting of LDS and 1,4-dithiothreitol (DTT), boiled at 95°C for five minutes and stored at -20°C for future use or run on a gel immediately. SDS-PAGE gels were run at 150 V for one hour in SDS running buffer containing 25 mM Tris, 192 mM glycine and 0.1% (w/v) SDS.

Colour Prestained Protein Standard, Broad Range (11-245 kDa) (New England Biolabs, now discontinued) was used as a molecular weight marker.

### **2.3.2 Coomassie stain**

Following electrophoresis, the gel was removed from its cast, washed briefly with tap water and incubated at room temperature for one hour in fixative solution consisting of 40% (v/v) ethanol and 10% (v/v) acetic acid. The fixative was then aspirated and the gel was washed thoroughly with tap water before Coomassie staining. A Coomassie solution was produced by dissolving 1 g of Coomassie Brilliant Blue G-250 (Thermo Fisher Scientific) in 5 ml dH<sub>2</sub>O and at the same time dissolving 100 g ammonium sulphate in 800 ml dH<sub>2</sub>O. The dissolved Coomassie, along with 20 g phosphoric acid, was added to the ammonium sulphate solution and the volume made up to 1 L. A staining solution was made comprising 80% (v/v) of the prepared Coomassie solution and 20% (v/v) methanol and the fixed gel was incubated in this overnight to ensure complete staining of the proteins within it. The following day the staining solution was removed and the gel was washed with tap water. The gel was then de-stained with 1% acetic acid until the gel itself became transparent and the protein bands were clearly visible due to their dark blue staining. The gel was then scanned to produce a digital image.

### **2.3.3 Western blot**

Proteins were transferred from SDS-PAGE gels (see above) to polyvinylidene fluoride (PVDF) membrane (Millipore Sigma) in Towbin buffer (25 mM Tris, 192 mM glycine, 20% (v/v) methanol) using a BioRad Trans-Blot<sup>®</sup> SD Semi-Dry Transfer Cell running at 15 V for one hour. Membranes were then blocked for one hour at room temperature in Odyssey buffer (LI-COR), a commercial blocking agent recommended for use with LI-COR scanning systems, which had been diluted 1:1 with Tris-buffered saline (TBS) (50 mM Tris-HCl pH 7.6, 150 mM NaCl). Blocking buffer was aspirated

and membranes were then incubated for one hour at room temperature with primary polyclonal BUNV NP antisera (collected from a sheep inoculated with purified BUNV NP, generated in house) diluted 1:5000 in TBS buffer supplemented with 1% Tween-20 (Fisher Scientific) (TBS-T). Primary antibody was removed and membranes were washed three times for five minutes each with TBS-T before incubation for one hour at room temperature with secondary IRDye® CW800 donkey anti-goat antibody (LI-COR) diluted 1:5000 in TBS-T. The secondary anti-goat recognises the primary sheep antibody due to goat/sheep cross reactivity. Secondary antibody was then removed and the membrane was washed three times for five minutes each with TBS-T. Membranes were dried for 15 minutes in the dark and protein bands were visualised by their fluorescence, which was detected with a LI-COR Odyssey® Sa scanning system.

## **2.4 Reconstituting RNPs**

### **2.4.1 Recombinant protein expression**

Attempts to reconstitute RNPs were performed using the NP of Simbu virus (SIMV), as it was readily available in the lab. SIMV NP was produced and kindly provided by Georgia Pangratiou (University of Leeds, UK).

Briefly, the SIMV NP coding sequence was codon optimised and synthesised in pUC57 vector (Genewiz). The NP ORF was sub-cloned into a pet28a expression vector (Novagen) downstream of a 6x histidine tag and a SUMO tag. This expression vector was transformed into *Escherichia coli* (*E. coli*) BL21-DE3 cells. Following isopropyl 1-thio- $\beta$ -D-galactopyranoside (IPTG) induction of protein expression, bacteria were pelleted and lysed and the lysate applied to a HisTrap HP nickel affinity chromatography column (GE Healthcare) to which histidine tagged proteins bind. A wash with a high concentration of NaCl was utilised to remove bound host RNA and

non-specific proteins were removed with low concentration imidazole washes, before NP was eluted with a high concentration imidazole wash. The 6x histidine tag was removed by cleavage with SUMO protease and a second metal affinity chromatography step separated the cleaved protein from the tag and the protease. Finally, size exclusion chromatography was utilised with a Superdex 200 26/600 column (GE Healthcare) to isolate tetrameric NP based on its molecular weight (~104 kDa). Tetrameric NP containing fractions were flash frozen in LN<sub>2</sub> and stored at -80°C and rapidly defrosted prior to use.

#### **2.4.2 Synthesis of BUNV genomic RNA**

The S segment-containing plasmid from the BUNV rescue system (pT7riboBUNS) (Lowen et al., 2004) (Kindly provided by Dr Xiaohong Shi, University of Glasgow) was used as the template for generating BUNV S segment RNA. The template plasmid was linearised by overnight incubation at 37°C with HindIII (New England Biolabs) and complementary RNA was generated by use of a HiScribe™ T7 RNA synthesis kit (New England Biolabs) according to the manufacturer's instructions. The resulting RNA was purified away from template DNA and proteins involved in the *in vitro* transcription process using an RNeasy kit (Qiagen) according to the manufacturer's instructions and the resulting purified BUNV S segment RNA was flash frozen in LN<sub>2</sub> and stored at -80°C.

## 2.5 Negative stain EM

### 2.5.1 Grid preparation and image acquisition

For virus and RNPs 5  $\mu$ l of sample was adsorbed to copper EM grids prepared in house by coating with a thin carbon film (Martin Fuller, Astbury Biostructure Laboratory, University of Leeds, UK). Immediately prior to sample application, grids were made hydrophilic by placing them carbon side up in a PELCO easiGlow™ Glow Discharge System and running the glow discharge process for 30 seconds. After five minutes of adsorption excess sample was blotted away with filter paper (Whatman) and the grid was washed twice with 20  $\mu$ l droplets of dH<sub>2</sub>O with blotting between washes. A 20  $\mu$ l droplet of 1% (w/v) uranyl acetate (which had been centrifuged briefly at high speed to pellet any crystals which might contaminate the grid) was then used to stain the grid for 15 seconds before excess stain was blotted away and the grid allowed to air dry and imaged immediately or stored in a grid box for later use.

For imaging recombinant protein this protocol was modified slightly to include a third dH<sub>2</sub>O wash and staining was done by the application of 2% (w/v) uranyl acetate for 20 seconds.

A small number of micrographs were collected using a JEOL JEM-1400 TEM with a Gatan UltraScan 1000XP 1k x 1k CCD camera (figure 3.2). The majority of negative stain micrographs were collected on an FEI Tecnai-T12 microscope with a Gatan UltraScan 4000 4k x 4k CCD camera. Both microscopes were aligned from the top of the column to the bottom and operated at 120 kV. Micrographs from the T12 were collected with one second exposures at roughly -1.5  $\mu$ m defocus at a magnification between 30000x and 68000x, resulting in pixel sizes of. For 2D classification micrographs were collected at a nominal magnification of 45000x, for a pixel size of 2.29 Å. When collecting a series of images for the purpose of 2D classification, the microscope was periodically refocused and then set back

to -1.5  $\mu\text{m}$  defocus and care was taken to ensure that the field of view moved enough between each image that all particles were unique.

### 2.5.2 Image processing

All image processing of negative stain data was carried out in Relion 3.0 (Zivanov et al., 2018) and followed the workflow illustrated in figure 2.1. Initial particle picking was performed manually and generated 1118 particles which were subjected to reference-free 2D classification. The most abundant classes were selected from this and used as initial references for autopicking. A total of 175583 particles was picked from sections of RNP filaments. Further rounds of 2D classification of these particles were carried out, discarding lower quality classes, until a final set of 2D classes were produced from 14899 particles.

For reference-free 3D classification the most populated class in the final 2D classification was used to generate a 3D initial model. Subsequently, this initial model was used as a reference to sort all picked particles into three classes. Later 3D classifications were carried out using a model generated from cryo-ET data which was reoriented and rescaled to match the box size and pixel size of the negative stain data, and particles which had been subject to one round of 2D classification to remove 'junk', leaving 122876 in total.

Helical reconstruction was carried out in Relion 3D auto-refinement with a tube of inner diameter 0 and outer diameter 100  $\text{\AA}$ . Helical symmetry was applied with 5 asymmetrical units and a central Z length of 30%. A range of initial twists and rises was tested, beginning with a twist of  $90^\circ$  and a rise of 18  $\text{\AA}$ , and for later 3D refinements, local searches of symmetry were applied with twist search and rise search set to a minimum and maximum which were -5 and +5 relative to the selected initial values. Ideal helices were generated in bsoft with different helical rises. These

were then fit to the to STA model in UCSF Chimera to determine the closest correlation with the STA, and thus the optimum helical parameters.

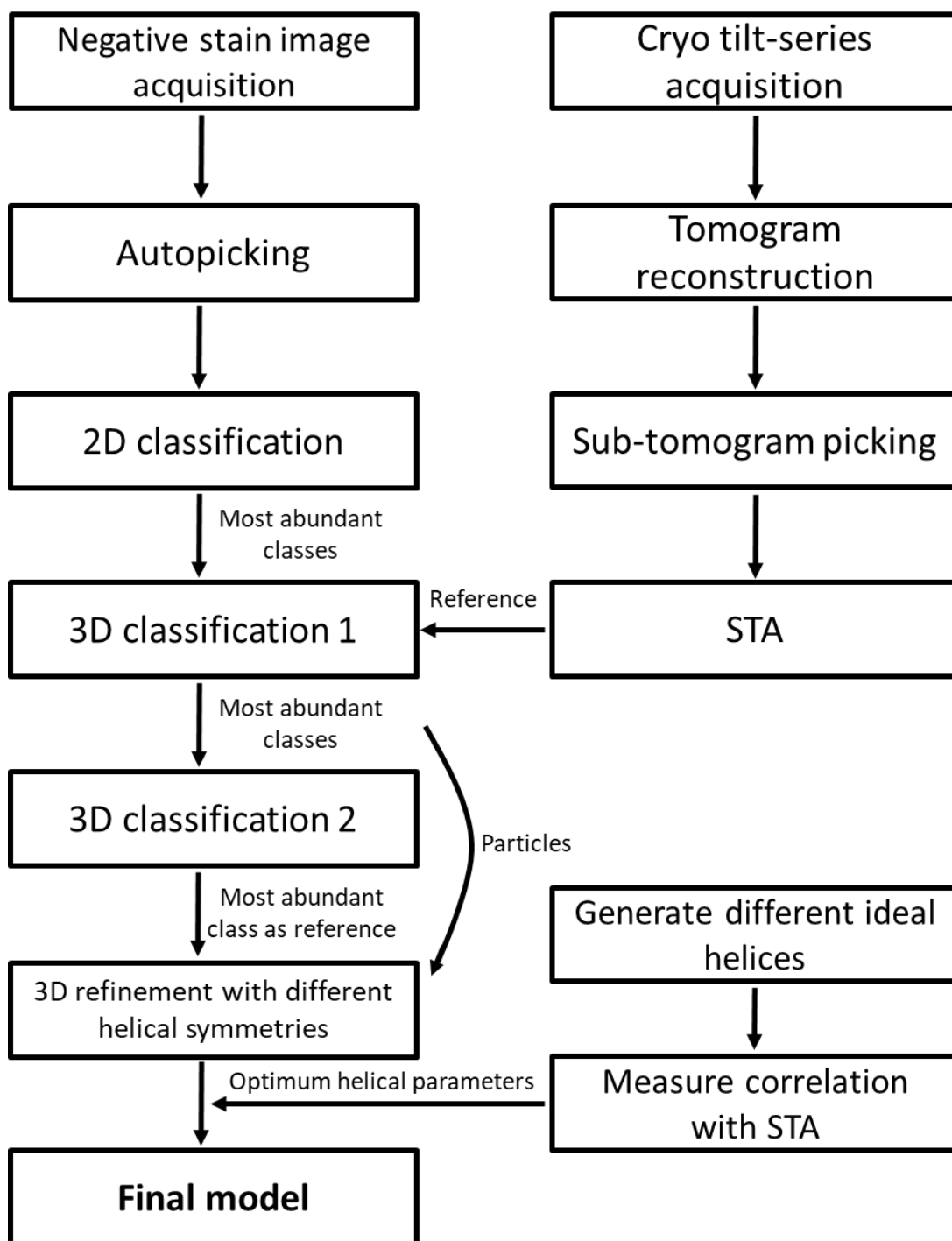


**Figure 2.1:** The EM data processing workflow employed in this project.

## 2.6 Cryo-EM

### 2.6.1 Grid preparation

Quantifoil holey carbon and lacey carbon grids coated with a 2 nm-thin layer of carbon were both tested for sample distribution. Data were collected exclusively on the lacey carbon grids because these exhibited a better distribution of the sample.

Grids were placed carbon side up and glow discharged immediately before use to render them hydrophilic, using a Cressington 208 carbon coater. All grids were prepared using an FEI Vitrobot IV at 100% humidity and 4°C, with a range of blotting times and nominal blotting forces tested. A 5 µl sample volume was applied to the grid while it was held in the upper chamber of the Vitrobot and after blotting, the grid was plunged into LN<sub>2</sub>-cooled liquid ethane and transferred to LN<sub>2</sub>.

### 2.6.2 Data collection

Vitrified samples were imaged at the University of Leeds on FEI Titan Krios microscopes equipped with either a Falcon 3EC DED (single particle) or an energy filtered Gatan K2 XP Summit DED and Volta phase plate (cryo-ET), and operating at 300 kV. On the fly motion correction and CTF estimation were set up in Relion (Thompson, R. F. et al., 2019). Single particle data was collected at a nominal magnification of 130000x for a pixel size of 1.065 Å. Cryo-ET tilt-series were collected at 2° intervals from -60° to 60° at a nominal magnification of 71000x for a pixel size of 2.7 Å.

### 2.6.3 Image processing

Single particle cryo-EM data was processed in Relion 3.0. Manual particle picking produced 1074 particles for reference-free classification but when the most abundant classes were selected they did not work as references for autopicking. A total of 30029 particles were picked manually and subjected to 2D classification and

reference-free 3D classification following the same workflow as the negative stain data (section 2.5.2).

Tomograms were reconstructed within the eTomo pipeline in the IMOD software package (Kremer et al., 1996) and sub-tomogram averaging (STA) was carried out with fiducial-less alignment and weighted back projection within PEET (Nicastro et al., 2006). Reconstructed tomograms were opened in the Fiji distribution of ImageJ to adjust their brightness and contrast and apply a 3D Gaussian Blur to aid in the picking of particles from RNPs (Schindelin et al., 2012). Sub-tomograms were manually picked using 3dMod; RNP filaments were traced, and points for each sub-tomogram were placed at 10 pixel spacing using the AddModPts program. STA was performed by alignment and averaging of these points in PEET, using absolute value of cross-correlation and strict search limit checking. For the first iterations only the orientation of the RNP (without rotation) was included in the angular search range, starting with a maximum of 24° and a step of 8° and halving with each iteration, to produce a straight cylindrical model. In later iterations when the RNPs were orientated down to 6°, the rotation search was included. The calcFSC script in IMOD was used to determine the resolution of the resulting STA model at a FSC cutoff of 0.5, and this was then displayed with the plotFSC script.

#### **2.6.4 Analysis of 3D models**

To dock crystal structures of BUNV NP, the 3D models produced were opened in UCSF Chimera version 1.14 (Pettersen et al., 2004), and a crystal structure of BUNV NP (PDB: 3ZLA) was opened in the same session, containing two RNA-bound NP tetramers. All chains were deleted from the crystal structure except for a single monomer, which was manually moved close to the EM model and fit with the command 'Fit in Map' from the 'Tools' menu. Electrostatic potential was illustrated on crystal structure surfaces using default settings in the command 'Coulombic Surface Coloring' from the 'Tools' menu.

## Chapter 3

# Isolation and initial characterisation of the architecture of BUNV RNPs

### 3.1 Chapter introduction

In 2013, several groups published crystal structures of NP from BUNV, SBV, LACV and LEANV orthobunyaviruses (Ariza et al., 2013; Dong, H., Li, P., Elliott et al., 2013; Li, B. et al., 2013; Niu et al., 2013; Reguera et al., 2013) and in each case NP crystallized in the form of a tetramer. In an attempt to relate the resulting models to the structure of the corresponding native RNPs, several of these studies also presented micrographs of negatively stained RNPs, either released from virions or derived from purified recombinant protein (Ariza et al., 2013; Li, B. et al., 2013; Niu et al., 2013; Reguera et al., 2013). Almost all of the RNPs released from virions appeared as closed circular filaments, while those reconstituted from recombinant NP displayed a shorter, linear conformation. On the basis of these data, two conflicting models for the structure of native orthobunyavirus RNPs were proposed, with one suggesting a tightly ordered helical structure with a width corresponding to that of the NP tetramer, and the other suggesting a less ordered structure in which individual NP molecules are linearly arranged on the viral RNA, connected by flexible head to tail interactions, referred to as the 'beads on a string' model (figure 3.1A).

Two other models were also put forward to explain the correlation between the width of the RNP and an NP tetramer (Ariza et al., 2013) (figure 3.1B). The first model suggests that the RNP is formed from repeating, stacked tetrameric rings and the second suggests it comprises a double helix formed from anti-parallel strands of NP, as exhibited by influenza virus RNPs (Arranz et al., 2012; Moeller et al., 2012). Both of these models however, have flaws. The BUNV NP tetramer contains a planar RNA binding channel so an RNP formed from a stack of tetrameric rings would require stretches of RNA to bridge the gaps between adjacent rings and a sizeable portion of the viral genome would be unencapsidated, while anti-parallel double helix RNPs would be expected to form rods rather than the observed flexible, circularised complexes. The limitations to these two models make either of them a more unlikely possibility than the ordered helix or ‘beads on a string’ models, but as of yet there is no unequivocal evidence to prove these models wrong. The disagreement on the fundamental ordering of the RNP arises mainly from differing measurements of the

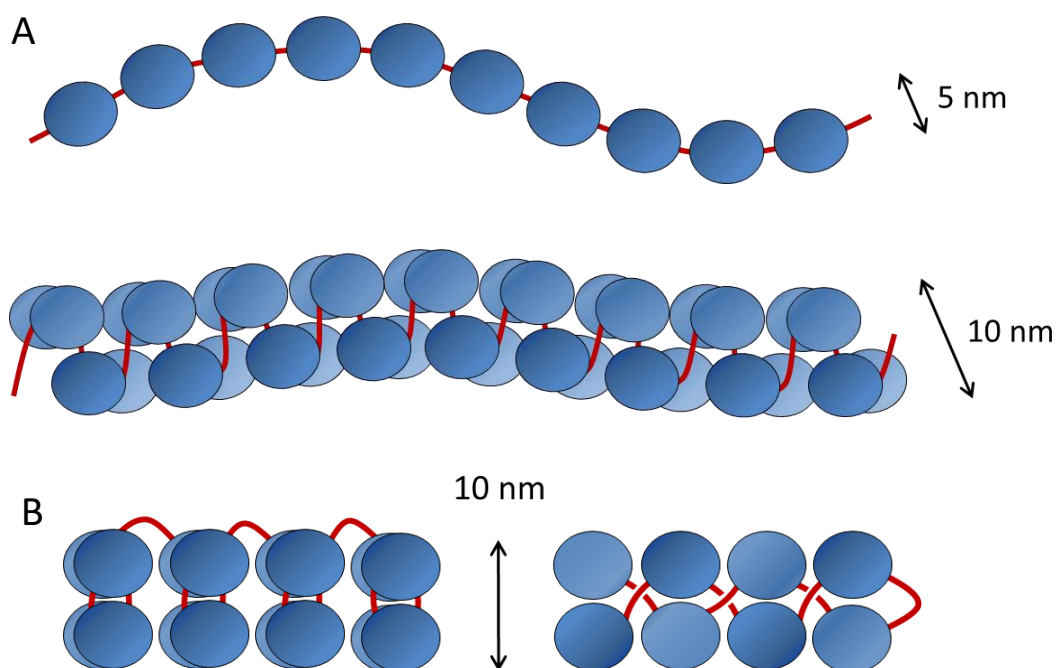


**Figure 3.1:** Proposed models of NP organisation within orthobunyavirus RNPs. **(A)** The two most commonly proposed models; monomer-based ‘beads on a string’ (top) and tetramer-based helix (bottom). **(B)** Proposed non-helical models to account for the matching widths of RNP and NP tetramer, described in (Ariza et al., 2013); stacked, tetrameric rings (left) and an anti-parallel double helix. Red = negative sense ssRNA.

width of the observed filaments, but also from the details of the features observed within the filament.

The packaging of genomic RNA into RNPs is likely to play a crucial role in the orthobunyavirus replication cycle, due to the functions that have been ascribed to the RNPs of other negative-strand RNA viruses. These were discussed in detail in chapter 1 and as well as physically sequestering the viral RNA away from the host immune system, RNP formation aids transcription and replication, and correct genome packaging into nascent virions through interactions with the cytoplasmic tails of the glycoproteins on the virion surface (Sun, Y. et al., 2018). The interaction of NP with RNA and its homotypic interactions with itself determine the overall architecture of the RNP and must be dynamic enough to allow conformational changes in the RNP which permit polymerase access to the RNA bases for transcription and genome replication. The importance of the RNP makes NP a promising candidate for structure-based drug design, but this requires more detailed knowledge of the overall organisation of the RNP. One important question that remains unanswered is what is the relevance of the two observed RNP structural arrangements in the orthobunyavirus replication cycle? Is one native and the other artefactual? Or, do they each represent alternative but relevant conformations that interchange and perform different functions at different stages of the virus replication cycle?

From the outset, cryo-EM was the method of choice to collect high resolution structural information on the orthobunyavirus RNP as it permits such information to be gained on large and dynamic protein complexes and filaments within solution. As described in chapter 1, the field of electron microscopy has advanced at a rapid pace since the negative stain analyses of orthobunyavirus RNPs in 2013, driven by the development of high speed DEDs such as the Falcon 2 and K2 and advances in image processing, as well as the introduction of 300 kV microscopes such as the Titan Krios. These developments have led to what is often referred to as the

'resolution revolution' (Kühlbrandt, 2014), which has allowed the determination of atomic or near-atomic resolution structures of macromolecules in their near-native states.

In order for cryo-EM to be successful it was first necessary to acquire very abundant and pure RNPs and then optimize the sample preparation protocol to enrich for well-separated and untangled RNPs for ease of subsequent computational analysis. To this end, negative staining of samples and visualisation with a 120 kV microscope was employed as the method of gauging the abundance, purity and suitability of RNP samples. Negative staining protocols, as described in chapter 1, are quicker and cheaper than preparing cryo-EM grids and the microscopes used are cheaper and generally simpler and quicker to operate than their cryo-EM counterparts. Thus, negative staining provides a powerful tool for screening samples for further analysis by cryo-EM.

The work which follows in this chapter describes optimising the extraction of RNPs from BUNV virions and moves to the search for the optimum conditions to produce the best sample for EM analysis. The large number of negatively-stained micrographs that were collected facilitated a preliminary examination of the RNPs in 2D, which begins to characterise their overall architecture. Although this analysis demonstrated that BUNV RNPs exhibit a width corresponding to an NP tetramer and the filament resembles a helix when viewed in 2D, it does not completely remove the possibility that they can also adopt looser conformations.

### 3.2 BUNV RNP purification

Over the course of this PhD project a number of different avenues were explored in an attempt to elucidate the structure of bunyaviral RNPs and the mechanisms of their assembly.

Initial efforts to purify bunyavirus virions and their RNPs for study also encompassed LCMV; an arenavirus recently reclassified into the *Bunyaviridae*. When LCMV virion purifications were analysed by SDS-PAGE and western blotting against NP it was found that the signal for NP was very faint and diffuse. The low signal intensity was attributed to low titres of virus being produced, which was in turn attributed to the propensity of LCMV to form defective interfering particles that are incapable of replication (Ziegler et al., 2016). Due to this fundamental difficulty in purifying enough LCMV RNPs for structural analysis, work on LCMV was stopped in favour of BUNV.

Attempts to reconstitute RNPs from recombinant NP initially involved the purification of NP from AINV and Ingwavuma virus (INGV), for which structures have not yet been determined. These proteins were purified for crystallography studies to compare their structures with existing ones from orthobunyaviruses and shed light on the mechanism of RNA binding by NP. However, these proteins were not produced at sufficient purity for crystallisation and could not be characterised by EM.

A final method trialled for the study of orthobunyaviral RNPs was engineering affinity tags into components of the RNP and using the established BUNV rescue system (Bridgen & Elliott, 1996; Lowen et al., 2004) to generate tagged RNPs which could be purified by affinity chromatography. However, attempts to rescue wild type BUNV according to the established protocol were unsuccessful and it was decided that optimising the protocol until successful was a less effective use of time and resources than following the promising leads in purification by ultracentrifugation.

### 3.2.1 Optimising BUNV virion purification

Initial attempts to purify wild type BUNV from mammalian cells involved using polyethylene glycol (PEG) to precipitate virions prior to ultracentrifugation. BHK cells maintained in 175 cm<sup>2</sup> tissue culture flasks were inoculated with infectious BUNV at an MOI of 0.01. Inoculated cells were maintained in serum free media to reduce the neutralising effect of serum proteins on virions, at a slightly reduced temperature of 33°C to minimise the cell death that would occur in the absence of serum, and the infection was allowed to progress for 72 hours. The flasks were filled with approximately 12 ml of media as this was the lowest volume that could totally cover the cell monolayer and a low volume increased the concentration of virions and thus the number of virions that could be loaded into ultracentrifuge tubes. After 72 hours of infection had passed the supernatant was collected from infected cells and precipitated with PEG.

Precipitated virions were subject to density gradient ultracentrifugation using a continuous density gradient made from OptiPrep™, a commercial preparation of iodixanol that is iso-osmotic and metabolically-inert. Fractions were aspirated from the gradient and small samples of these were analysed by SDS-PAGE and western blotting using BUNV NP antisera to identify a peak of NP abundance corresponding to where virions had settled within the gradient. However, a diffuse pattern of NP intensity was observed across most of the gradient (figure 3.2A) with no single clear peak. Furthermore, virions were not clearly visible when fractions with NP signal intensity were analysed by negative staining EM (figure 3.2B).

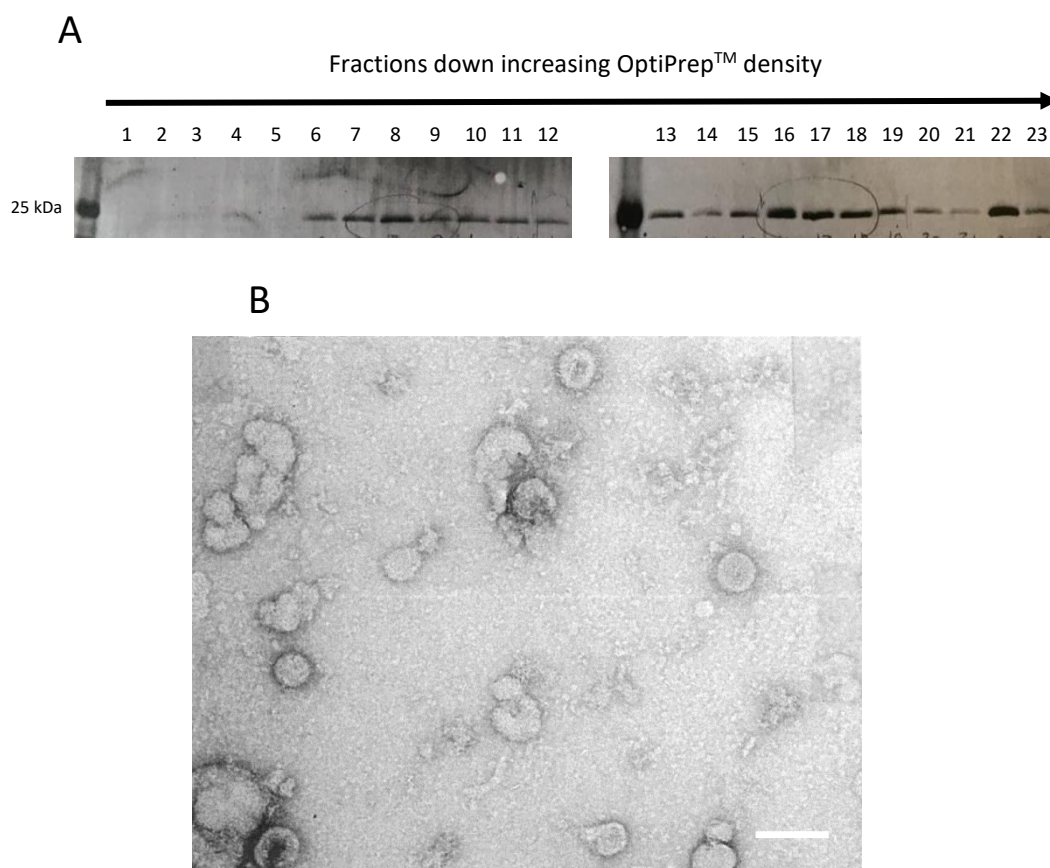


**Figure 3.2** BUNV virions were precipitated with PEG and purified by density gradient ultracentrifugation. **(A)** Fractions taken from the gradient did not contain a clear peak of NP when analysed by western blotting. **(B)** Samples from NP-containing fractions were negatively stained and imaged by TEM. Scale bar is 100 nm.

Since PEG precipitation of virions and application to a continuous density gradient did not yield purified virus particles a new protocol was adopted, in which the initial precipitation step was omitted and supernatant from virus-infected cells was gently centrifuged at 4000 *g* to pellet cellular debris. The clarified supernatant was then ultra-centrifuged through a 30% (v/v) sucrose cushion, to both trap large amounts of contaminating proteins above the cushion, and pellet the virions, which were subsequently resuspended overnight at 4°C in 50 µl of TNE buffer. SDS-PAGE and western blot analysis showed the sucrose cushion protocol was highly successful in concentrating the released virions, as evidenced by a faint band corresponding to NP in the supernatant prior to ultracentrifugation, and a much more intense band in the resuspended pellet (figure 3.3A). This large increase in NP concentration was

consistent with the observed reduction in sample volume during the purification process, in which 180 ml of virus-containing supernatant was reduced to a volume of approximately 50  $\mu$ l of resuspended pellet.

In addition to increased virion concentration, this protocol also allowed purification of virus from contaminating proteins; analysis of the resuspended pellet by SDS-PAGE and Coomassie staining revealed that viral proteins were highly abundant in relation to non-viral contaminants. A prominent non-viral protein band at approximately 56 kDa was present in the supernatant prior to purification and was attributed to BSA in the tissue culture medium. This band was not present in the three different pellets shown, in which the most dominant bands could be attributed to viral proteins NP, Gn and Gc (figure 3.3B).

Small samples of resuspended pellets were applied to glow discharged, carbon-coated copper grids, washed twice with dH<sub>2</sub>O and negatively stained with 2% uranyl acetate for 30 seconds before visualisation with a Tecnai 12 microscope (FEI). In the resulting micrographs, roughly spherical virions were observed that were approximately 100 nm in diameter and largely intact. Some of the virions appeared to have damaged membranes and a small number of filamentous structures could be seen that resembled previously published images of orthobunyavirus RNPs and which may have spilled from virions damaged by the ultracentrifugation protocol (figure 3.3C).

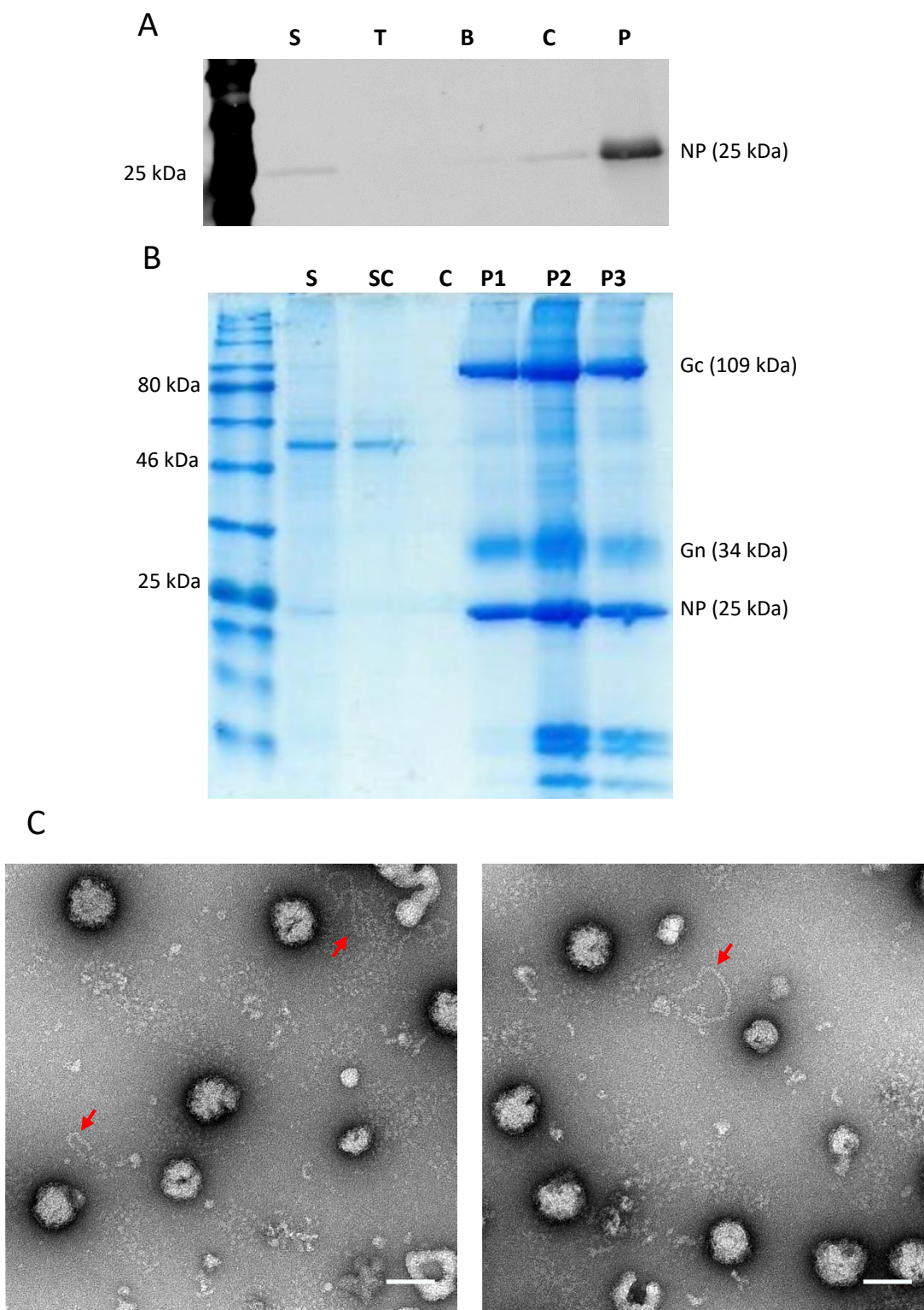


**Figure 3.3:** Centrifugation through a sucrose cushion effectively purified BUNV virions. **(A)** SDS-PAGE followed by western blotting showed a large increase in the amount of NP after purification. **(B)** SDS-PAGE followed by Coomassie staining showed the removal of contaminating BSA and abundance of viral proteins in the pellet. **(C)** Negatively staining the contents of the pellet for visualisation by TEM revealed abundant, clear virions and a small number of RNP filaments (red arrows). Scale bars are 100 nm. S = supernatant pre-purification. SC = clarified supernatant pre-purification. T/B = top/bottom of supernatant post-purification. C = cushion post-purification. P\* = resuspended pellets.

### 3.2.2 Releasing RNPs from BUNV virions

#### 3.2.2.1 Sucrose

Having established a protocol to concentrate and purify large numbers of infectious virions it was necessary to devise a method to effectively release RNPs from within purified virus particles in a manner that was compatible with further analysis by EM.

The first attempt to lyse virions was based on previously established methods (Li, B. et al., 2013) and utilised 1M sucrose to cause osmotic disruption of the viral envelope. Virions were incubated in sucrose for an hour prior to applying them to a grid, however this failed to induce lysis with abundant intact particles visible and no isolated RNPs (not shown). As an alternative approach, virions were next adsorbed to the EM grid and subsequently washed with 1M sucrose solution, before washing with dH<sub>2</sub>O and staining with 2% uranyl acetate as described previously. This approach revealed a small number of discrete RNPs that appeared with high contrast

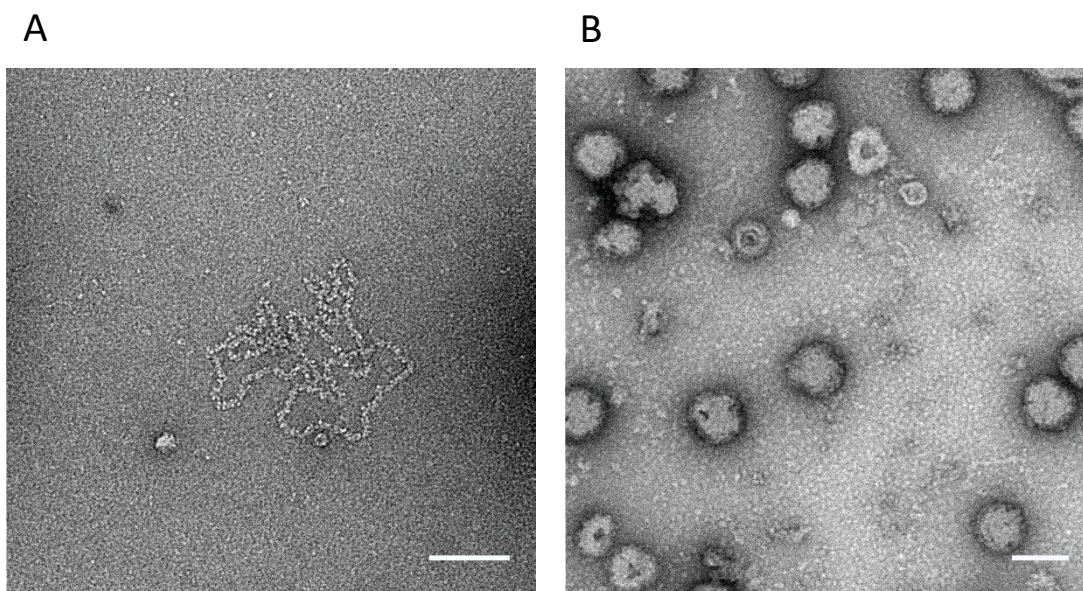


**Figure 3.4:** Washing with 1M sucrose was not a reliable method of lysing virions to release RNPs. **(A)** Initial attempts to lyse virions with sucrose worked and a small number of very clear, well resolved RNPs were observed after negative staining. **(B)** Subsequent attempts at lysing virions with sucrose were unsuccessful and negative staining showed that many virions were still intact following the treatment. Scale bars are 100 nm.

against a very low background signal, and very low presence of contaminating material. This suggested that lysis with 1M sucrose was suitable to effectively release RNPs, although due to the small amounts of any material on the grid it was possible that the subsequent washing steps led to the depletion of virions and RNPs remaining on the grid (figure 3.4A). This lysis protocol using 1M sucrose proved difficult to replicate and in subsequent attempts little to no lysis of virions was observed, and was accompanied with high background signal (figure 3.4B).

### 3.2.2.2 Detergent

A more reproducible method of RNP release from virions was required and a common approach used by others has been to disrupt the viral envelope using detergent (Ariza et al., 2013; Reguera et al., 2013). Following these previous approaches, virions were incubated with the non-ionic detergent Nonidet P-40 (NP-40) at a concentration of 0.1% (v/v) for one hour at 4°C before samples were adsorbed to grids, washed with dH<sub>2</sub>O and stained with 2% uranyl acetate for visualisation by EM. Large membranous structures, likely disrupted and empty virions were observed as well as filaments, suggesting that the detergent was effective at

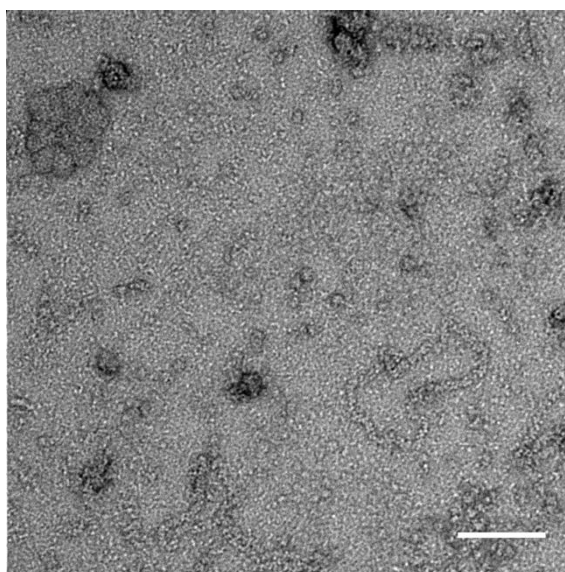


**Figure 3.5:** RNPs were effectively released from virions by adsorbing them to a carbon coated grid which was then washed with NP-40 alternative. However, this caused problems with background signal from the detergent. Scale bar is 100 nm.

breaking virus membranes. However, the micrographs contained a high level of background signal, which would have prohibited more thorough analysis by EM, and is a common problem encountered when using detergents for EM sample production (figure 3.5). Thus, a new protocol was sought, which provided sample reproducibility but without the same problems of high background signal.

### **3.2.2.3 Freeze-thawing**

Throughout the entire process of virus growth and purification care was taken to avoid any freeze-thaw cycles since the resulting physical damage this causes to the lipid envelope is known to decrease virus viability. However, since virus viability was not a consideration for the extraction of RNPs, and to avoid the addition of chemical reagents which could adversely affect EM, freeze-thaw cycles were employed as a mechanism to disrupt the viral membranes and allow RNP release. Resuspended, purified virus was frozen at  $-80^{\circ}\text{C}$  and thawed at room temperature before applying to grids, staining with 2% uranyl acetate and imaging by EM. The resulting micrographs had a low background and high contrast and allowed the clear visualisation of the effects of freeze-thawing on membrane bound viruses (figure 3.6A). Intact virions and membrane debris from disrupted virions were observed, as well as discrete, circular RNP filaments that were sometimes captured spilling from their parent virion (figure 3.6C). This single step freeze-thaw method of releasing RNPs was the most reproducible and further rounds of freeze-thawing did not have a noticeable effect on the proportion of virions that were disrupted and were spilling their RNPs (figure 3.6B). A single round of freeze-thawing was incorporated into all subsequent RNP purifications to effectively release RNPs without adding other reagents unnecessarily.

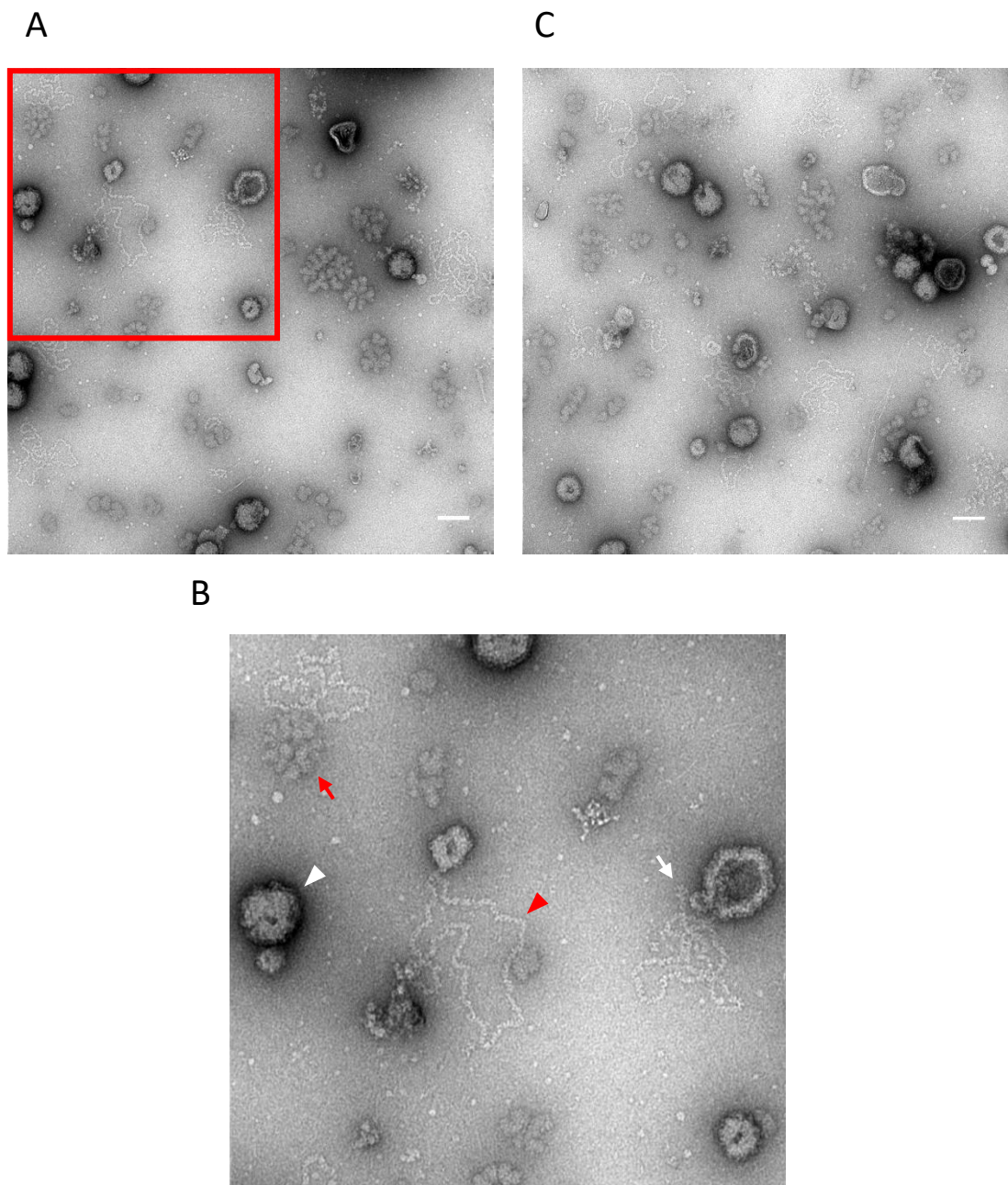
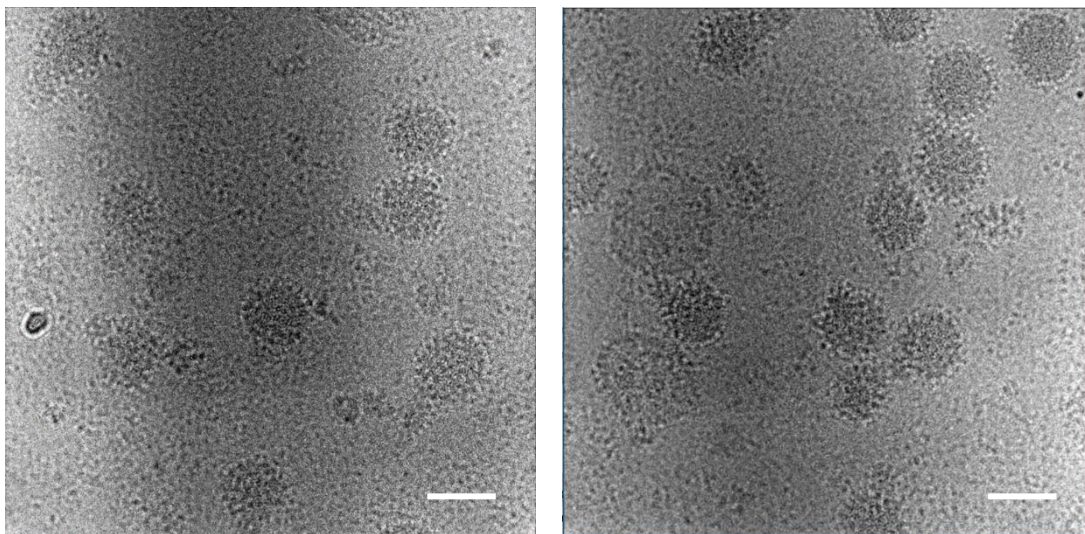


**Figure 3.6:** Freeze-thaw cycles were tested for their effectiveness at disrupting virion membranes. **(A)** One round of freeze-thawing caused great physical damage to virion particles and the release of RNPs. **(B)** Zooming in on the boxed region in (A) shows virion membranes (red arrow), intact virions (white triangle), discrete RNPs (red triangle) and an RNP spilling from a virion (white arrow). **(C)** Two rounds of freeze-thawing was not noticeably more effective at releasing RNPs than one round. Scale bars are 100 nm.

### 3.2.3 Initial cryo-EM

With an effective and reproducible protocol for the release of BUNV RNPs a first attempt at cryo-EM was undertaken. Cryo-EM grids were prepared by applying freeze-thawed virions to lacey carbon-coated copper grids and plunge freezing them with an FEI Vitrobot. Grids were screened on a Titan Krios microscope to find areas of the grid with optimum ice thickness and distribution of RNPs. An overnight data collection was set up using EPU, with on-the-fly motion correction and CTF correction in Relion, and a total of 1027 micrographs were collected. The problems with this data collection however, were twofold; Firstly, due to technical difficulties encountered by the microscope during the data collection period, micrographs were collected at a broad range of defocus values (most of which exceeded 20  $\mu\text{m}$ ) and apart from the lower defocus value ones from the beginning of the data collection, most were simply not suitable for further analysis. Secondly, a more fundamental flaw was found with the RNP sample itself upon inspection of the better micrographs collected. These revealed few RNPs but an abundance of high contrast intact virions, identified by their lipid membrane and characteristic glycoprotein spikes (figure 3.7A). It was hypothesised that the incomplete lysis of virions led to the formation of a thick layer of vitrified ice on the grid with a depth of around 100 nm, approximately that of an intact BUNV particle. This is an order of magnitude greater than the previously observed width of a BUNV RNP, of approximately 10 nm. The dimensions of this thick ice layer would provide more 3D space for the RNPs to adopt multiple orientations, rather than to lie flat within the ice. In addition, the thick ice layer may obscure signal from any RNP filaments that were aligned in a flat and uncoiled way (figure 3.7B). It was thus decided to attempt separation of the RNPs from larger particles such as intact virions or the debris from lysed virions prior to cryo-EM analysis.

A



B

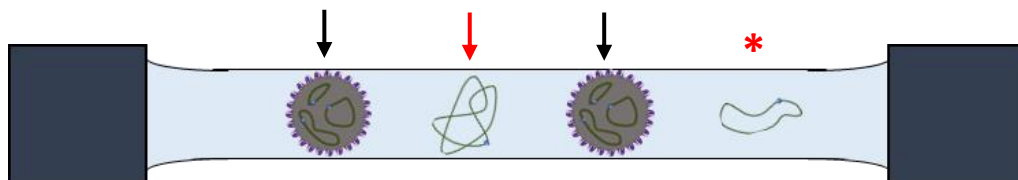


**Figure 3.7:** Micrographs from an initial cryo-EM single particle data collection contained clear images of virions but not of RNPs. **(A)** Representative micrographs from cryo-EM data collection. **(B)** Schematic to illustrate how the ice thickness of the grid conformed to the diameter of a virion (black arrows) which could have caused RNPs to coil up (red arrow) or remain spread out but be obscured by thicker ice (red asterisk). Scale bars are 100 nm.

### 3.2.4 RNP purification by continuous density gradient ultracentrifugation

To separate RNPs from larger components, a further round of ultracentrifugation was implemented, using a continuous density gradient as had been described previously (Ariza et al., 2013; Novoa et al., 2005; Reguera et al., 2013). Following a single freeze-thaw cycle purified virions were subjected to a 30 minute incubation with Triton X-100 and NP-40 alternative detergents as in (Reguera et al., 2013) to ensure complete disruption of lipid membranes. Although care had been taken previously to remove detergents from the protocol their addition ensured complete virion lysis and maximum RNP yield, and after a short centrifugation at 10000 *g* to pellet membranous debris the lysed BUNV particles were layered on top of a 5 to 25% OptiPrep™ gradient. Due to the low volume and high

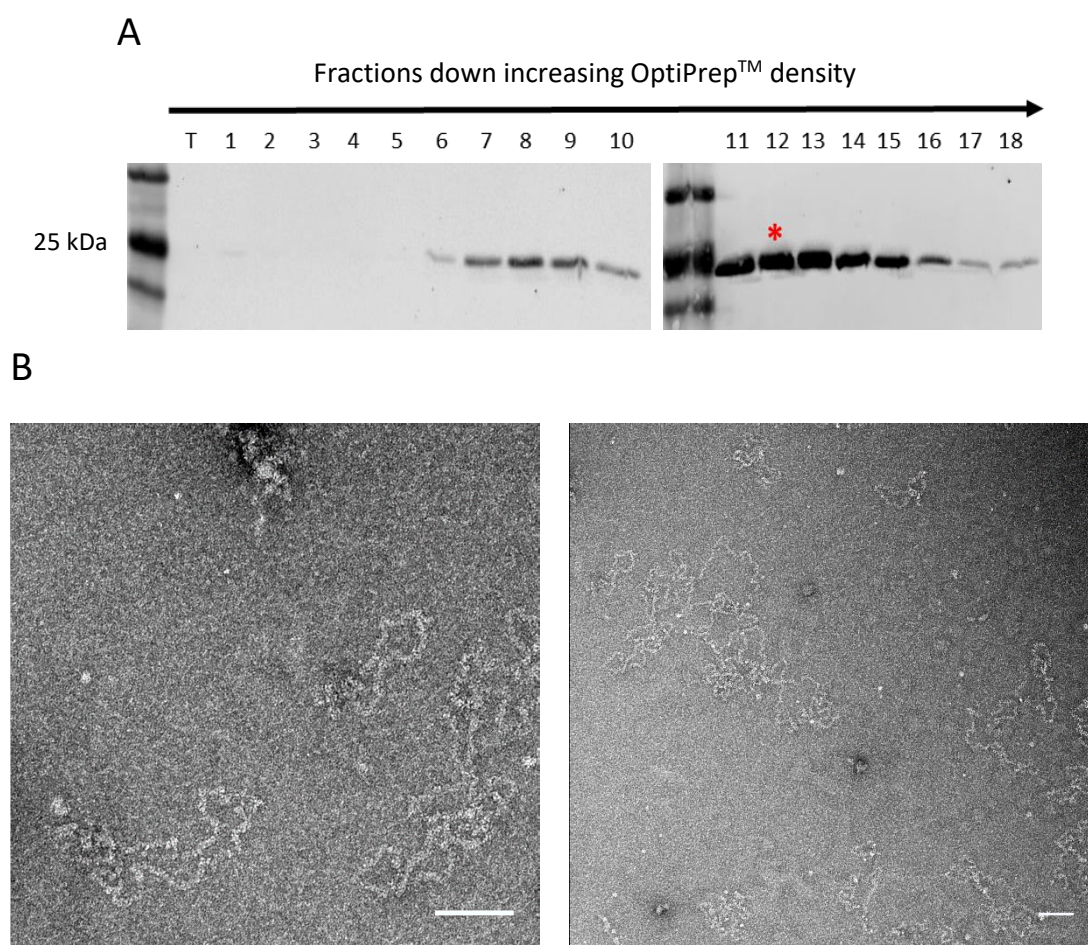


**Figure 3.8:** Visualisation of purified RNPs. **(A)** Disrupted virions were applied to a continuous density gradient and ultracentrifuged, banding around fraction 12 (red asterisk). **(B)** Samples of fraction 12 were visualised by EM and were found to contain abundant, discrete RNPs. Scale bars are 100 nm.

concentration of disrupted virions the gradient was prepared to a volume of 3.6 ml, which is lower than that used previously by other groups (Li, B. et al., 2013; Novoa et al., 2005).

Following ultracentrifugation residual material at the top of the tube was aspirated and then 200 µl fractions were taken from the top to the bottom of the gradient. Samples of each fraction were analysed by SDS-PAGE followed by western blotting with NP antisera to identify peak NP intensity corresponding to the RNP-containing fractions within the gradient (figure 3.8A). Two NP peaks were detected within the gradient, which corresponded to fractions 8 and 12. Small samples of these two fractions were applied to carbon-coated copper grids, negatively stained with 2% uranyl acetate and analysed by EM for the presence of RNPs. While uranyl acetate staining of grids corresponding to fraction 8 failed to reveal any distinct NP containing structures (not shown) fraction 12 was found to contain a large number of characteristic RNPs (figure 3.8B). This protocol was reproducible and so was utilised throughout the rest of the project.

### **3.2.5 Optimum buffer conditions for EM analysis of RNPs**

To increase the chances of obtaining successful class averages, and eventually a 3D reconstruction of an orthobunyavirus RNP, the buffer in which the RNPs were applied to the grid needed to be optimised. The ideal buffer would provide the minimum noise and thus the highest contrast, as well as preventing the filaments from aggregating and thus presenting a high proportion of straight segments. Despite being notoriously difficult to remove from solution, the iodixanol component of OptiPrep™ can pass through a concentrator with a large enough molecular weight cutoff (MWCO). The BUNV S segment is 961 nucleotides in length so assuming a binding stoichiometry of 11 nucleotides per NP monomer, an S segment RNP should be comprised of 87 NP monomers, which corresponds to a mass of at least 2 megadaltons (MDa). Thus, a concentrator with a 100 kDa MWCO would be expected

to trap S segment RNPs as well as those of the significantly larger M and L segments, and this approach was utilised for buffer exchange to test a range of different buffer compositions, much like the screening process in crystallography.

First, a range of different NaCl concentrations within the TNE was tested ranging between 0 and the 200 mM. It was found that NaCl concentration had a marked effect on the RNP conformation and the degree of RNP straightening broadly correlated with increasing NaCl concentration in an inverse manner, with straightest RNPs observed in 25 mM NaCl. Interestingly, when NaCl was absent, RNPs appeared less straight than in 25 mM NaCl (figure 3.9A-C). Increasing or decreasing the pH from the 7.4 of standard TNE did not have an observable effect on the straightness of RNPs (figure 3.9G-H).

Incubating the RNPs with antibodies was tested using anti-BUNV NP sheep antisera which had been generated in house. It was predicted that an antibody would bind across nearby sections of the RNP and pull that area of the filament straight. What was actually observed was the RNPs condensing into tight coils and it was reasoned that the antibodies were actually binding to distant sections of the RNP and bringing them into closer proximity (figure 3.9G). Introducing this antibody to the RNP sample also introduced a large amount of debris which obscured the RNPs and which was attributed to serum proteins and other contaminants originating from within the sheep antisera. The addition of DTT to the buffer appeared to promote some straightening of the RNPs (figure 3.9D), whereas the addition of magnesium to the TNE resulted in no noticeable effect (figure 3.9E). Swapping NaCl for KCl in the TNE also resulted in no observed improvement of RNP straightness (figure 3.9F).

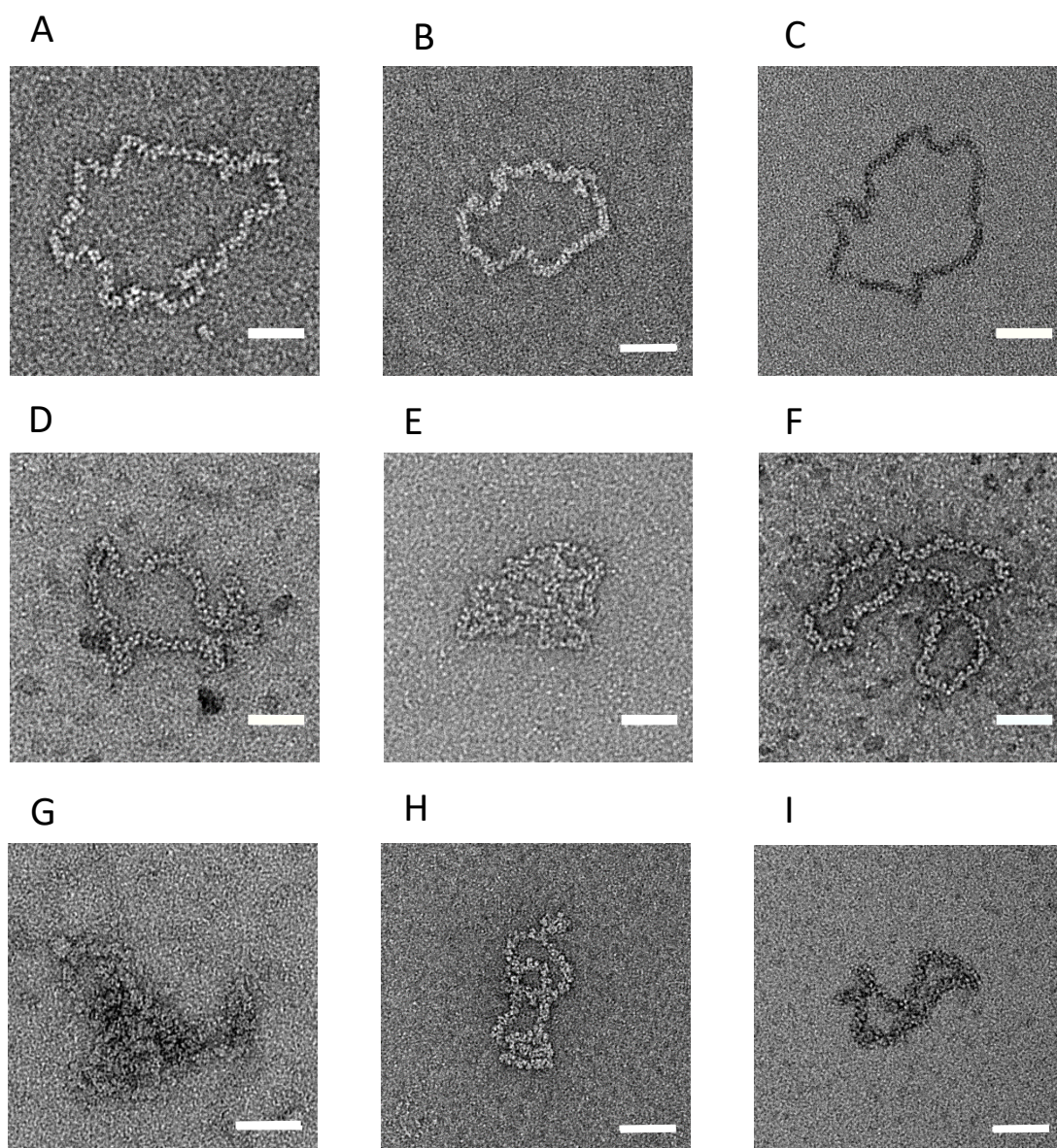


**Figure 3.9:** The effects of different buffers on RNP conformation. Purified RNPs were visualised after buffer exchange into a variety of different conditions; **(A)** TNE with no salt. **(B)** TNE with 25mM NaCl. **(C)** TNE with 50 mM NaCl. **(D)** TNE with addition of DTT. **(E)** TNE with addition of MgCl<sub>2</sub>. **(F)** TNE with KCl substituted for NaCl. **(G)** TNE with addition of antisera. **(H)** TNE pH 6.4. **(I)** TNE pH 8.0. Scale bars are 50 nm.

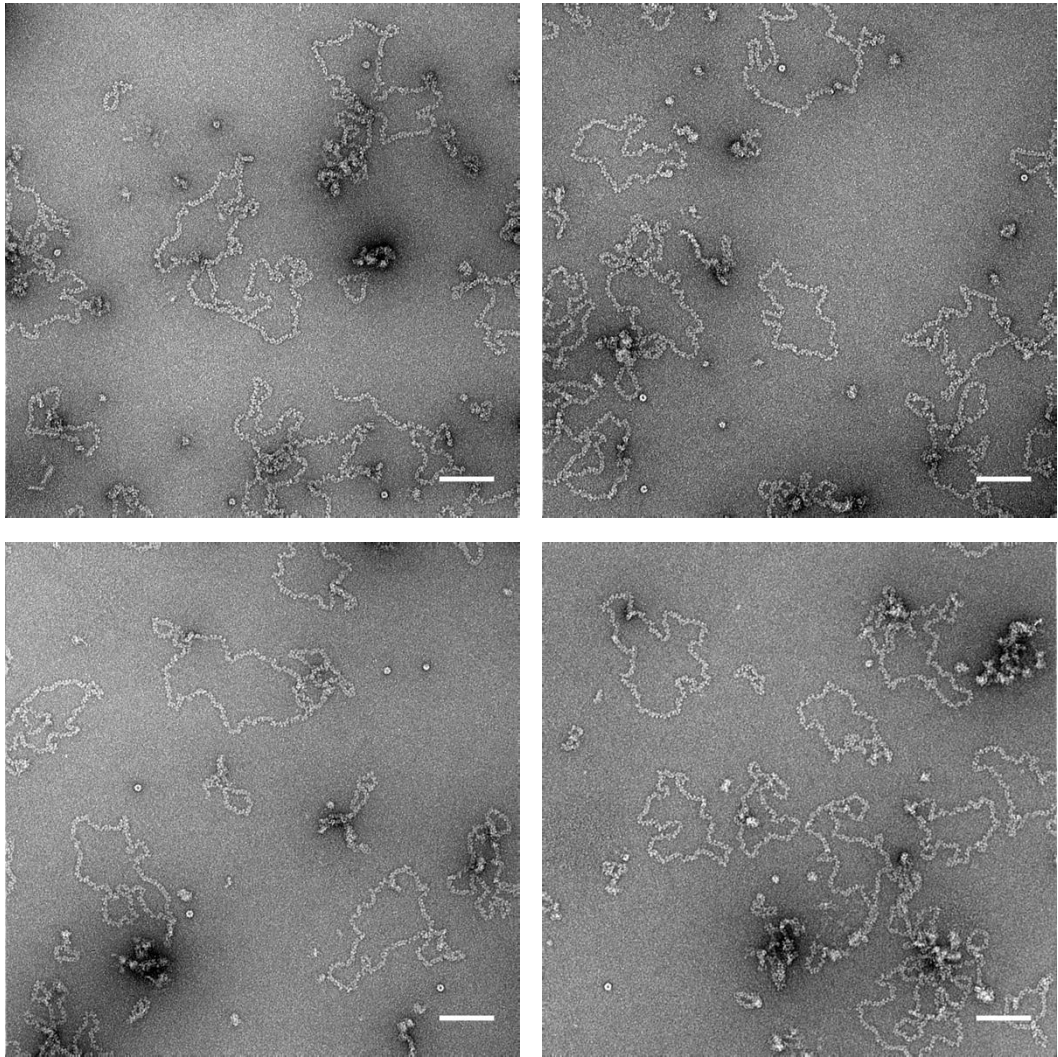
### 3.2.6 Optimising concentration of RNPs

Despite the current protocol now yielding highly purified discrete RNPs, a more concentrated sample was required to ensure that enough particles could be acquired from micrographs in later analysis, particularly in cryo-EM data.

Having established that a freeze-thaw step of virions was an essential step in the RNP purification protocol, this allowed for multiple pellets from separate virus harvests to be stored at  $-80^{\circ}\text{C}$  and pooled together prior to the second round of ultracentrifugation, thus increasing the quantity of starting material. This provision meant that the capacity of the centrifuge rotor used in sucrose cushion purification was no longer a limiting factor in how many RNPs could be purified, as multiple pellets could now be resuspended in a volume appropriate for a single gradient. After scaling up the amount of purified virus being disrupted and applied to a continuous density gradient, RNPs were purified by the already established protocol and buffer exchanged into the four most promising buffers.

Negatively stained EM grids were prepared from each of these to determine the optimum grids for further negative stain, and subsequent cryo-EM analysis. The condition containing TNE with a reduced NaCl concentration of 25 mM was selected and a series of micrographs was collected from this grid for class averaging and further analysis (figure 3.10A). Within these micrographs circular RNPs were abundant and clearly visible due to the low background noise and high contrast of negative staining. Circular filaments of a range of different lengths were observed and when viewed more closely it was possible to see the individual NP monomers within the filament and the step-wise, rising organisation they adopt within the context of the RNP filament (figure 3.10B), similar to that seen in previously published micrographs (Ariza et al., 2013; Reguera et al., 2013).

A



B

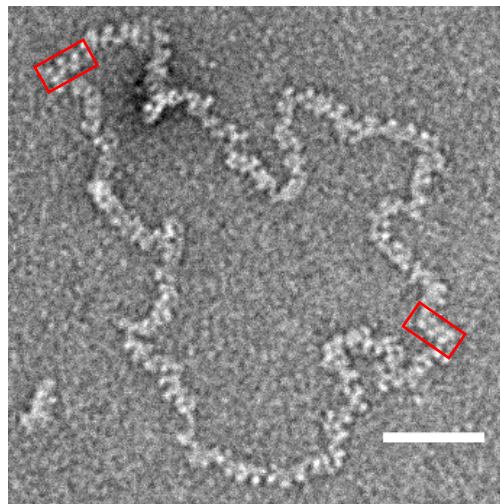


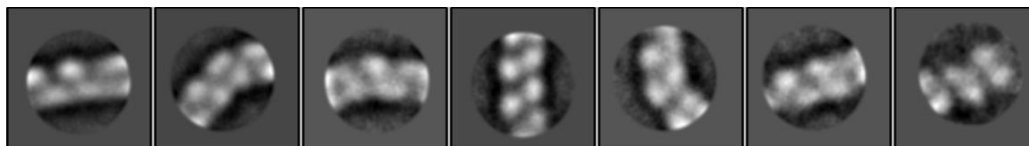
**Figure 3.10:** Optimising RNP concentration. **(A)** High contrast micrographs were obtained of negatively stained BUNV RNPs. **(B)** Zooming in reveals the detail of a single, discrete RNP filament. Red rectangles highlight areas with a clear alternating pattern of monomers. All scale bars are 100 nm in **(A)** and 50 nm in **(B)**.

### 3.3 Analysis of negatively stained BUNV RNPs

#### 3.3.1 Class averages of RNP filaments

Analysis of negatively stained RNP filaments in 2D was performed on a total of 263 micrographs, which had been collected at a nominal magnification of 45000x and a defocus of approximately -1.4 nm, and constituted a very large data set of high contrast discrete RNPs. Initial 2D class averages of RNPs were produced from ~1000 manually picked particles in Relion 3.0 and the top classes, representing 833 particles were selected as references for autopicking (figure 3.11A). Due to very high flexibility of the filaments it was uncertain if the autopicking tool in Relion would be able to effectively pick particles along the lengths of filaments, so it was tested on a small subset of 10 micrographs. The filaments in these micrographs were found to be extremely amenable to autopicking in this manner (figure 3.11B).

A



B

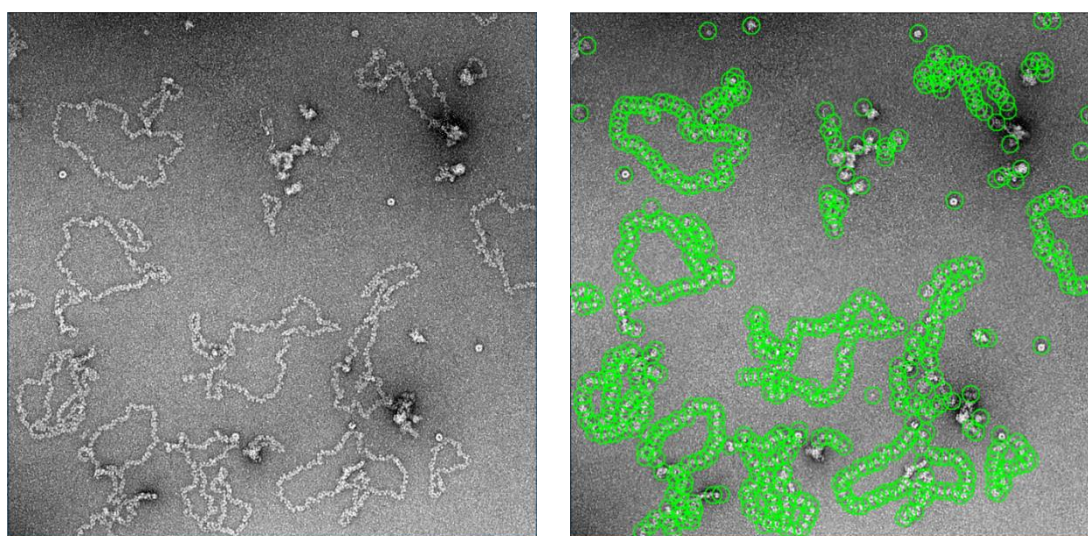
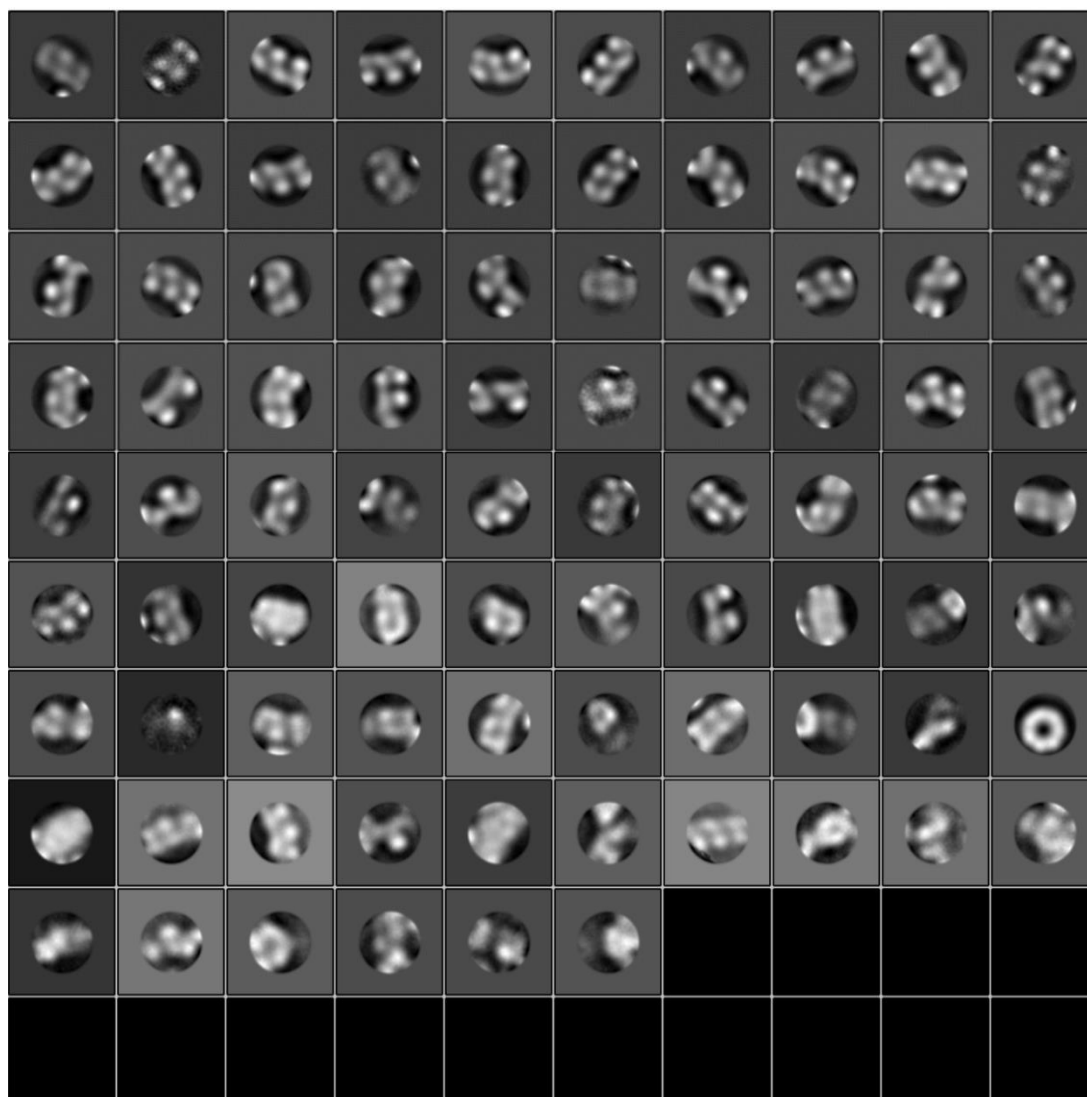


**Figure 3.11:** Reference based autopicking of BUNV RNPs. **(A)** Initial class averages of RNPs were produced from manually picked particles and the most populated classes selected. **(B)** Selected classes were then used as references for autopicking which was highly effective, demonstrated by comparing a typical micrograph (left) and the particles selected by the Relion autopicker tool (right).

The reference particles used to generate the initial class averages (figure 3.11A) were then applied to all available micrographs. From these 263 micrographs the Relion autopicker selected ~180000 particles that were extracted for classification. The initial 100 classes produced from these particles (figure 3.12A) confirmed that the particles were suitable for analysis, producing clear averages in which monomers of NP could be easily distinguished. The bottom 50 classes from this initial classification were discarded and the remaining 50 were reclassified into 100 new classes. This process of manually discarding junk particles and reclassifying the rest was repeated until a final subset of the top ~15000 particles remained which was classified into 10 final classes (figure 3.12B). These top classes of the RNP filament unequivocally demonstrate a step-wise, rising pattern of monomeric NP along the axis of the filament that appears in 2D as an alternating left to right placement of monomers. This supports the hypothesis that BUNV RNPs exhibit a helical architecture based on a multimer of NP (Ariza et al., 2013) and which resembles the helical crystal structure that has been reported (Reguera et al., 2013).

A



B

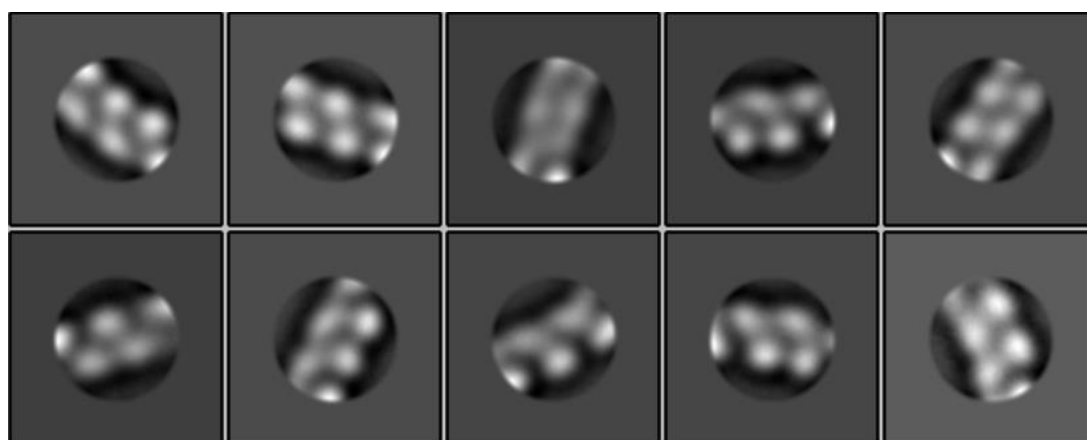


**Figure 3.12:** 2D classification of BUNV RNPs. **(A)** The entire set of particles extracted following autopicking was divided into 100 classes, the top 50 of which contained clear averages of filaments which were classified further. **(B)** After multiple rounds of classification the final 10 class averages represented the most homogenous particles.

### 3.3.2 Filament characteristics

Preliminary analysis of the nature of the BUNV RNPs was done on the collected micrographs of negatively stained sample (figure 3.13). The diameter of filaments was measured in ImageJ by measuring across several points within the filament class averages which had been produced previously (figure 3.13A). RNPs were found to have a mean observed width of 9.2 nm with a minimum of 8.9 nm and maximum of 9.5 nm, in keeping with previous measurements (Ariza et al., 2013; Reguera et al., 2013) but at odds with others (Li, B. et al., 2013; Niu et al., 2013). Estimates of the helical pitch of the filaments were derived by measuring between the neighbouring NP monomers within filament class averages using ImageJ (figure 3.13A). In this manner, the helical pitch was found to have a mean value of 6.3 nm, in keeping with previous findings for LACV (Reguera et al., 2013). Maximum and minimum values of the helical pitch were 4.9 nm and 8.6 nm and were found in curved sections of RNP. In these sections the NP monomers on the outer edge of the curve were more spread out and adopted a distinct 'spine' appearance, while those on the inner curve were pushed closer together. Additionally, the lengths of individual, discrete circular RNPs were measured in ImageJ following manual tracing with the segmented line tool. A histogram of the measured lengths of approximately 800 RNPs demonstrated that three distinct species of RNP existed that could be attributed to the S, M and L genomic segments (figure 3.13B-C).

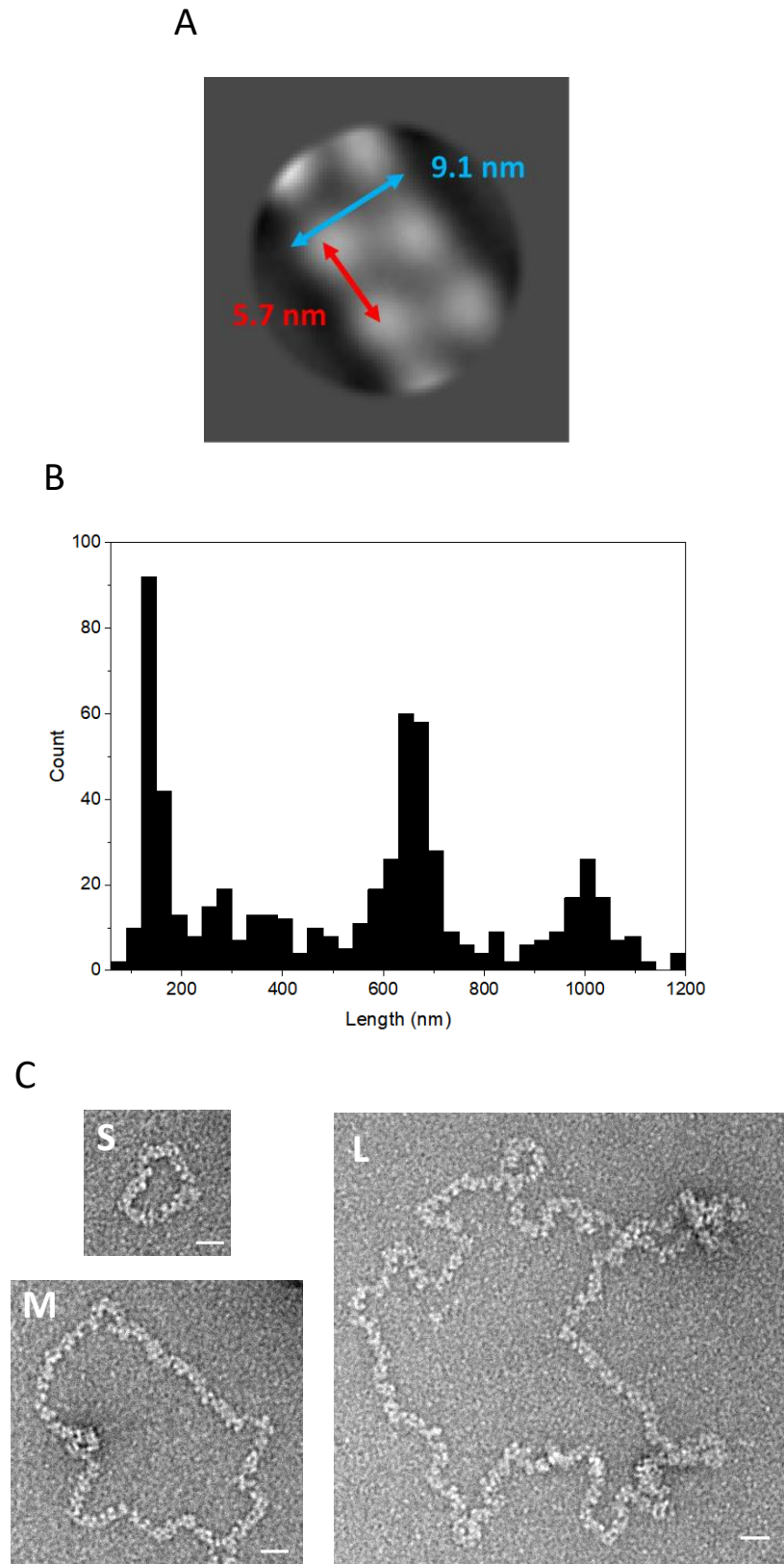


**Figure 3.13:** Initial characterisation of BUNV RNPs. **(A)** ImageJ was used to measure the diameter and helical pitch of RNPs. **(B)** ImageJ was also used to trace the lengths of filaments and three distinct populations corresponding to S, M and L genomic segments were identified. **(C)** Representative S, M and L RNPs. All scale bars are 20 nm.

### 3.3.3 Class averages of bends within RNP filaments

Within the micrographs of abundant RNPs it was apparent that the filaments could bend at a wide range of angles while maintaining their structural integrity, and within the initial classification (figure 3.12A) bent or kinked RNP classes were produced in which discrete NP monomers could be distinguished. To establish if RNPs bend at a distinct series of angles and to investigate how the conformation of NP adjusts to accommodate bending, particles were picked with a larger box size which centred on the points where an RNP filament bent at an angle of at least 45°. Initial classes were produced and used as references for autopicking in Relion, resulting in ~140000 particles. These were subject to successive rounds of 2D classification until 20 classes representing ~20000 particles remained. These classes clearly showed the range of angles at which BUNV RNPs can bend, but revealed little of the mechanism behind this. In most classes, monomers were more clearly visible at the edge of the box and the signal in the interior was more diffuse, suggesting a degree of heterogeneity that prevented clear averaging. It was apparent however that where the filaments bend, the distance between monomers increases on the outside of the curve but decreases on the inside (figure 3.14). Interestingly, it was expected that somewhere in all of the acquired images of intact, complete RNPs there would be some evidence of a heterogeneous sections like a bump or a kink which could be attributed to the ends of the RNA segments and the proposed panhandles which form. However, there was no evidence as such in these classes or those produced from smaller particles (figure 3.12).

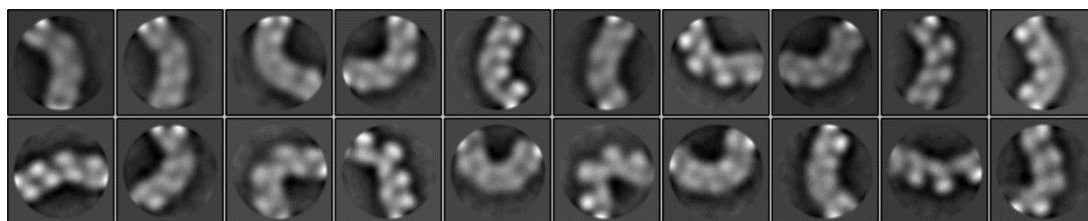


**Figure 3.14:** 2D classification of BUNV RNP corners. Particles of a larger box size were placed manually to produce initial classes and then these were used for autopicking. After several rounds of 2D classification to remove particles of straight filaments, a final set of classes was produced of the bends and kinds within the filaments.

### 3.3.4 Class averages of a potential viral polymerase

When highly abundant RNPs were visualised by negative staining a distinct population of asymmetrical ring-shaped particles was observed, and a large proportion of these were in close proximity to RNP filaments (figure 3.15A). Interestingly, these particles closely resembled the class averages of polymerases from other negative sense RNA viruses (figure 3.18) (Gerlach et al., 2015; Kranzusch et al., 2010; Liang, B. et al., 2015) and due to this and their apparent association with RNP filaments it was hypothesised that they might be BUNV polymerase molecules that have disassociated from purified RNPs. These particles appeared infrequently in micrographs and in an attempt to produce class averages a total of almost 1000 were selected from within micrographs. Class averages of these particles were produced, which showed them to be very regular ring shapes, unlike typical polymerases and unlike how the particles had initially appeared in micrographs (figure 3.15B). This was likely due to the low number of particles which could be picked and there not being enough for effective alignment and averaging.

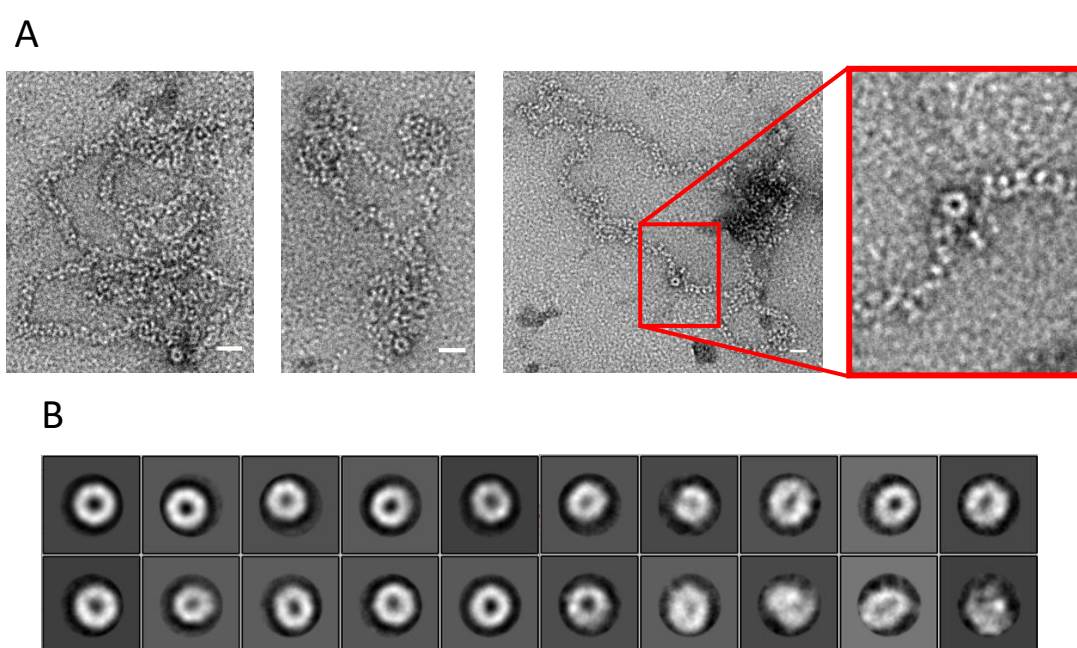
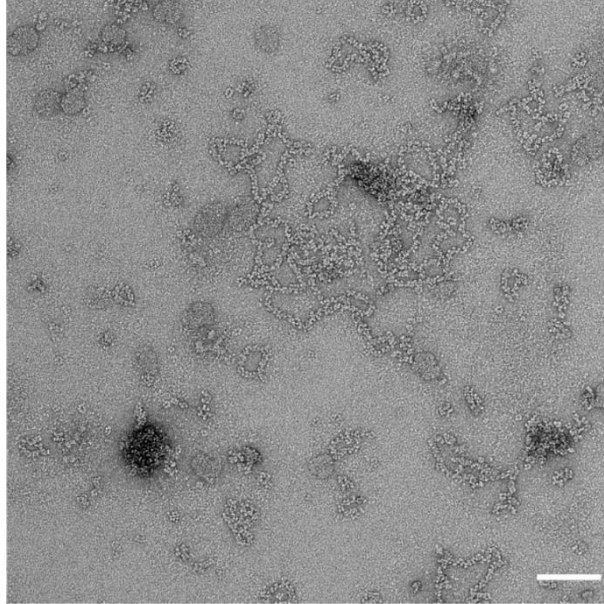


**Figure 3.15:** Large particles were found within micrographs which were potentially the viral polymerase. **(A)** Ring-like particles of roughly 80 to 100 nm diameter were observed, often in proximity to filaments. Inset in red shows detail. **(B)** 2D classification was performed on these particles. Scale bars are 20 nm.

### 3.3.5 Heating RNPs alters their conformation

In order to begin studying how the orthobunyavirus RNP might respond to the internal temperature of a mammalian host, and how the filament may accommodate the binding of the polymerase for transcription and genome replication, purified RNPs were heated to 37°C for 30 minutes, as previously described (Reguera et al., 2013). In this study, the authors reported unwinding of the helical RNPs into a much narrower filament more akin to the 'beads on a string' model and propose that this conformation leads to greater exposure of RNA and permits transcription and genome replication. Analysis of heated RNPs by negative staining revealed them to be much less ordered than unheated samples, and a variety of small oligomers were observed (figure 3.16A). Despite the apparent increase in heterogeneity across the RNPs the Relion autopicker was still able to effectively pick particles along filaments as well as picking small, discrete oligomers and picked ~50000 particles from 80 micrographs. After two rounds of 2D classification the top ~30000 particles were classified into 50 class averages. These averages revealed that although some stretches maintained the alternating, helical pattern, some stretches adopted more a stacked ring conformation and many of the classes showed such heterogeneity that it was difficult to see a filament at all. Interestingly tetramers, pentamers and hexamers were all observed as well (figure 3.16B).

A



B

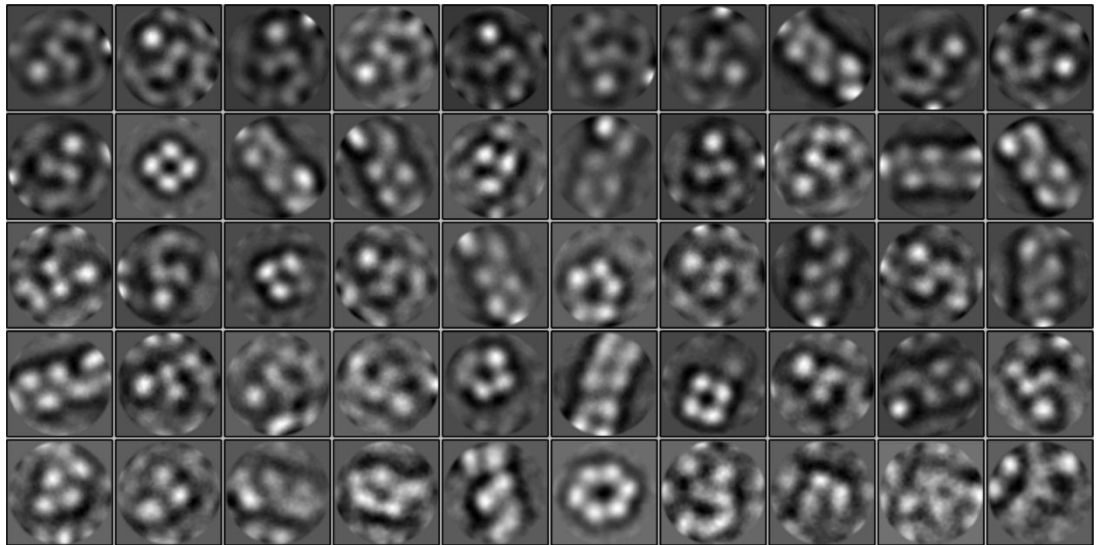


**Figure 3.16:** The effect of heating on BUNV RNPs revealed by negative staining. **(A)** RNP filaments appeared more heterogeneous following heating to 37°C and oligomeric rings were produced. **(B)** Class averages from these micrographs showed that some heterogeneity was preserved within filaments, while oligomeric rings consisted of tetramers, pentamers and hexamers. Scale bar is 100 nm.

### 3.4 Recombinant RNPs

Recombinant orthobunyaviral NP was incubated with BUNV S segment RNA in an attempt to reconstitute RNP filaments. The NP utilised was that of SIMV because it was readily available and NP across the orthobunyaviruses has high structural similarity and shares sequence-independent RNA binding. SIMV NP had been purified by size exclusion chromatography and corresponded to the molecular weight of a tetramer.

Negative stain EM and classification of apo SIMV NP revealed that rather than just being tetrameric, a small number of pentameric and hexameric species were contained within the sample. Upon incubation of NP and RNA for one hour at room temperature, larger oligomers such as heptamers and octamers were visible. Interestingly, oligomers appeared to associate with each other in a lateral manner, as evidenced by both the raw micrographs and class averages in which pairs of oligomeric rings appear side by side (figure 3.17A). A small number of aggregates were observed where more than two oligomeric rings were closely associated with each other into small 'clump' of protein. Finally a small number of filamentous structures were observed, although they look markedly different to the virion-derived RNPs described previously, and it is a strong possibility that these are just chains of tetrameric NP (figure 3.17B).

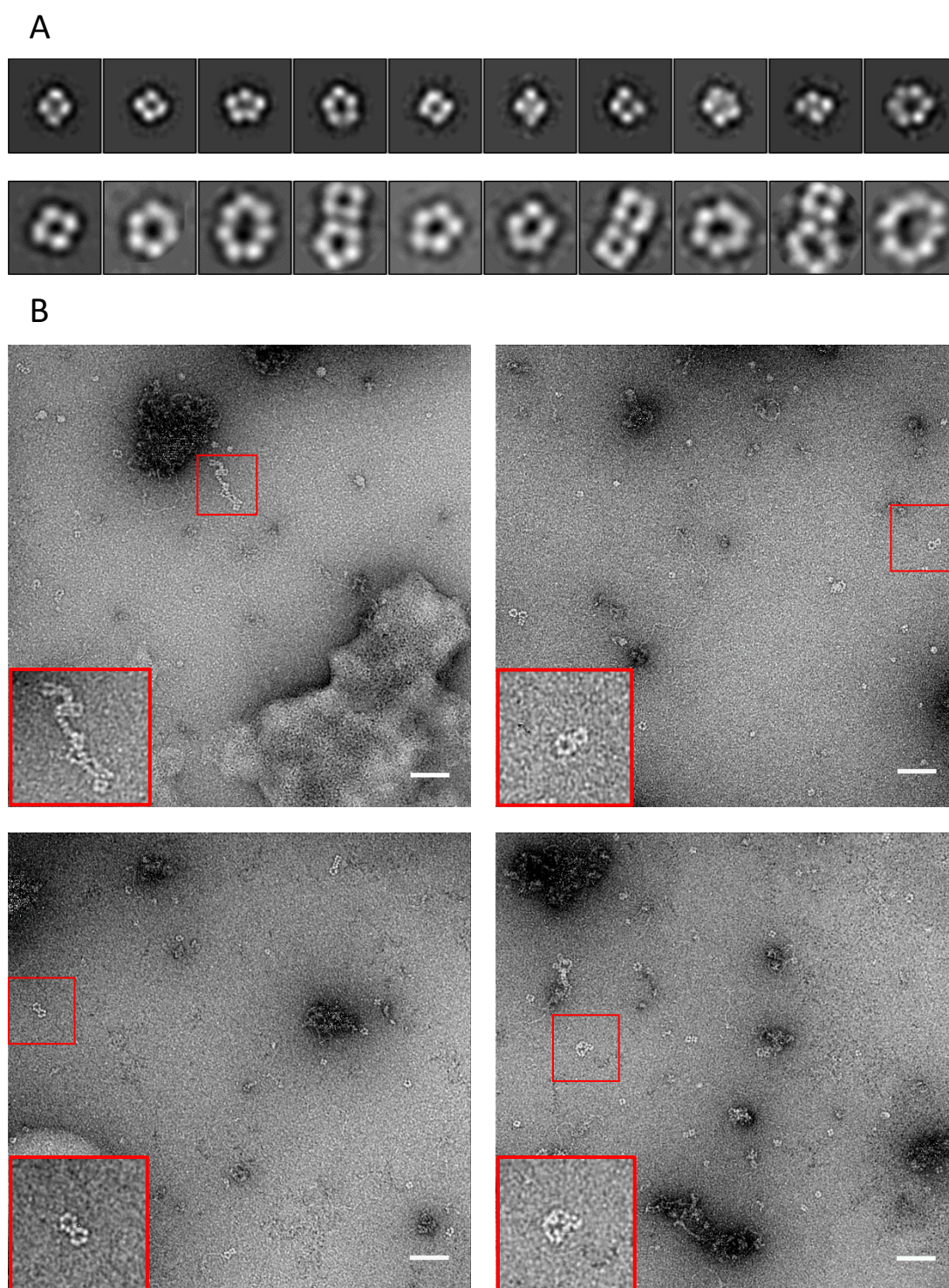


**Figure 3.17:** Reconstituting RNPs from recombinant protein and RNA. **(A)** Class averages from apo SIMV NP (top) and from micrographs represented in **(B)** (bottom) show a range of oligomeric rings formed on mixing NP and RNA, and these oligomers apparently associating with each other. **(B)** Representative micrographs with insets to show detail of oligomeric NP associating into larger complexes. Scale bars are 100 nm.

### 3.5 Discussion

The work presented in this chapter describes the optimisation of a protocol for the analysis of orthobunyavirus RNPs by negative stain EM. Utilising a sucrose cushion and a gentle resuspension it was possible to obtain pure, concentrated and mostly intact virions. After freezing and thawing this purified virus it was possible to observe the release of RNPs from disrupted virions as in figure 3.6B where an RNP has been captured in the process of spilling from a virion. Initial efforts to analyse these spilled RNPs by cryo-EM were unsuccessful due to the need to separate the RNPs from the virions themselves. A protocol for this was optimised which involved using an OptiPrep™ gradient and then removing the OptiPrep™ by buffer exchange. A range of buffer conditions was tested in order to obtain the straightest RNPs possible to make them as suitable as possible for EM analysis. It was observed that changing the salt concentration had the biggest effect on the conformation of the RNPs, with lower concentrations producing the most suitable RNPs for analysis.

Initial images of the purified RNPs showed that they had a distinct stepwise, rising pattern of alternating monomers which could be helix based on a multimer of NP, and which appeared to be roughly 10 nm wide with a helical pitch of roughly 6 nm. RNPs proved very amenable to autopicking in Relion and class averages from ~15000 particles clearly exhibited the helical pattern and close analysis in ImageJ agreed with the observations of width and helical pitch with average values of 9.2 nm and 6.3 nm respectively.

Two striking observations from all of the images of intact RNPs (figure 3.10A) raise interesting questions about the fundamental nature of the orthobunyavirus RNP. Firstly, almost without exception the RNPs were circularised. The circular nature of bunyaviral RNPs was already known, and had already been visualised by EM (Pettersson & Bonsdorff, Von, 1975). This was traditionally thought to be a consequence of the complementary 3' and 5' ends of the vRNA forming a panhandle,

circularising the RNA strand. Recent insights into the binding of 3' and 5' ends of the vRNA to the RdRp have led to an updated model in which the vRNA ends are held apart from each other on the polymerase molecule, but this model is still compatible with a circularised RNP. The second observation is that, with the exception of the large, round particles which were sometimes in proximity to RNPs (figure 3.15), no circularised RNPs contained a region of noticeably different architecture, which could be compatible with an RNA panhandle or a bound polymerase. Evidence for such a region was also never found within class averages of RNP filaments (figure 3.12), even though the Relion autopicking tool was so effective that virtually all possible RNP particles were picked (figure 3.11B). The RNPs observed here would appear to be completely linear arrangements of NP-enwrapped RNA. The number of RNA nucleotides at the 3' and 5' ends is ~8-11 (Reguera, Gerlach & Cusack, 2016) so if they protrude from the RNP then it is possible that they are simply too small to observe. If the RNA ends are protruding from the RNP then the lack of particles which could be clearly attributed to bound polymerase could suggest that their interaction with the RNP has been disrupted at some point in the purification protocol. Further experimental analysis would be needed to confirm this and to determine what factors affect this interaction.

Within the original micrographs the RNPs were a variety of lengths but mostly fell into three distinct populations of approximately 150, 650 and 1020 nm. The size of the genomic segments of wild type BUNV are 961, 4458 and 6875 bases for S, M and L respectively. Structural studies have shown that orthobunyavirus NP binds to 11 nucleotides (Ariza et al., 2013; Niu et al., 2013; Reguera et al., 2013). Dividing the length of each segment by 11 gives an estimate of the number of NP monomers bound to each segment; 87, 405 and 625. Thus, if the number of monomers is divided by four to account for the number of monomers per turn in the proposed helix, and the length of each segment is divided by this number of tetramers, an estimate of the helical pitch can be estimated. For S, M and L segments these values are 6.8, 6.4

and 6.5 nm respectively. These values are very similar across the three different segments, and the difference between them could be attributed to the longer segments being more flexible. Since the distance between monomers varies when the filaments bend (figure 3.14) the average distance would be slightly different in filaments containing more bends. These calculated values are also very close to the value of 6.3 nm calculated from analysing 2D class averages (figure 3.13). The close agreement of these calculated values with those observed in EM leads to an interesting conclusion. If extended stretches of RNA protrude out of the RNP then the number of bound NP monomers per RNP would be lower and the numbers calculated would be different. The RNP must therefore encapsidate the entirety of the viral genome, precluding the possibility that BUNV, and likely other orthobunyaviruses, can accommodate extended RNA secondary structures within their RNP, as has been demonstrated for influenza virus (Dadonaite et al., 2019).

All observed RNPs displayed a width of around 9 nm and a helical pitch in keeping with the calculated values, and no beads on a string conformations were observed. The values calculated here also lend evidence to the hypothesis of a helical architecture of orthobunyavirus RNPs. A monomer of BUNV NP within the crystal lattice is 4 nm in length (Ariza et al., 2013) so if monomers were arranged on RNA end-to-end, like 'beads on a string', then the 87 monomers bound to an S segment RNA would be 348 nm in length, which is over twice the length observed here. It would be interesting to quantify the number of each type of genome segment to test the hypothesis that each virion contains one copy of each segment and similar analysis has been performed on RVFV (Wichgers Schreur & Kortekaas, 2016). In the histogram produced here (figure 3.13B) it appears that there are many more S segment RNPs present than M or L, however this may be an artefact of the manual tracing method by which RNPs were measured, and the larger RNPs were often simply too flexible to identify a single, discrete RNP with complete confidence.

An interesting question in this field is that of how the helical RNPs achieve their observed flexibility, which must be essential for packaging into virions. In an attempt to shed some light on this class averages were produced from ~20000 particles which were centred on the corners of RNPs (figure 3.14). These averages show that the RNPs seem to bend at a relatively small number of angles but these were not homogenous enough to produce clear alignments and averages. However, the angle of these kinks within the filaments seem to fit within quite a narrow range of different values. The signal within the middle of these averages is more diffuse than in the other class averages produce, indicating that there is a large degree of heterogeneity in terms of the actual arrangement of NP monomers within the filament as it bends.

After scaling up the production of viral RNPs a number of large, ring-like particles were also observed and were often in close proximity to RNP filaments. The particles themselves appeared to resemble the class averages of the polymerases of other negative RNA viruses (figure 3.18). However, when 2D classification was

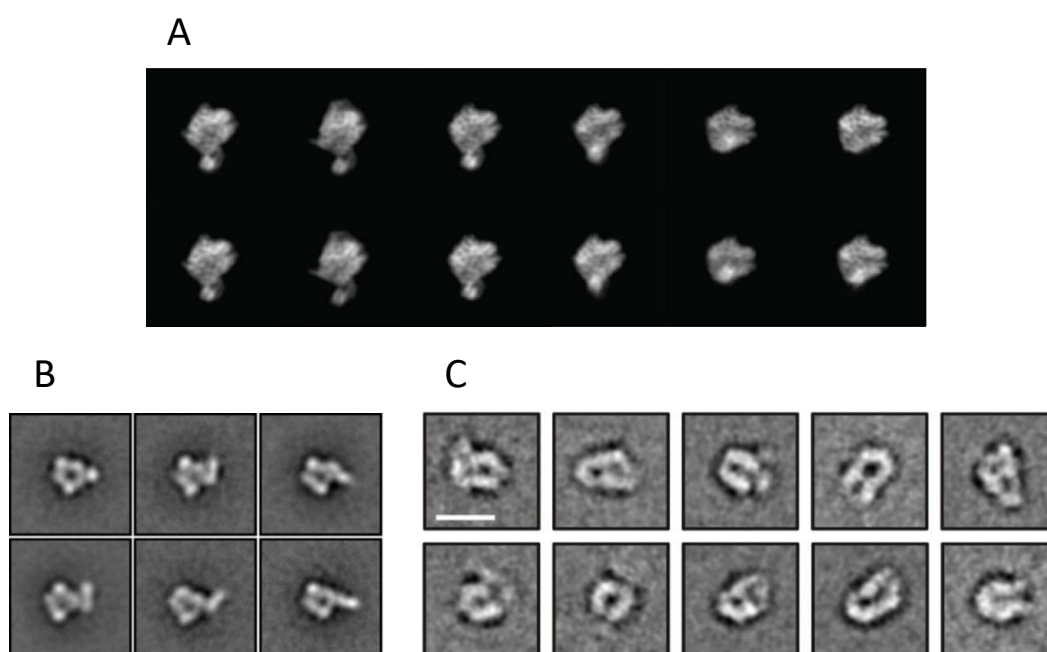


**Fig 3.18:** Previously published 2D class averages of the polymerase of different negative RNA viruses. (A) LACV, from (Reguera et al., 2013). (B) Machupo virus (MACV), from (Kranzusch et al., 2010). (C) Vesicular stomatitis virus (VSV), from (Liang, B. et al., 2015).

performed on the particles observed here the class averages appeared much rounder and smoother (figure 3.15), and the distinctive shape and features seen in other polymerases were much less apparent than in the micrographs. One possibility is that these particles were rings of NP, but their class averages are very different to the classes of oligomeric rings of NP which were produced (figure 3.17B). Due to the low number of particles used to generate averages it is difficult to test our hypothesis that these might be the viral polymerase. Purifying the viral polymerase from infectious virus is inefficient and polymerase bound bunyaviral RNPs have never been reported before in the literature, and if the particles presented here are indeed polymerase roughly 1000 of them were found in 263 micrographs; more than an order of magnitude fewer than the number of picked filament particles from the same micrographs. A different approach would have to be adopted for a thorough study of how the viral polymerase associates with NP and RNA to form a complete RNP, possibly by reconstituting RNPs from recombinant protein or by relying on reverse genetics to engineer an affinity tag into the polymerase; two approaches which have had success in the study of influenza (Coloma et al., 2009; Martín-Benito et al., 2001)

Reguera et al (2013) reported that heating the RNPs to 37°C resulted in unwinding of the helical filament into a narrower and more flexible conformation. In our hands, heating had a different effect; RNPs lost their ordered, helical structure but retained the characteristic diameter of unheated samples. This transition to a less-ordered conformation may have the same effect as that proposed in (Reguera et al., 2013), which is to allow RdRp access to the RNA for transcription and replication, albeit through a very different mechanism. It is unclear why the different oligomeric rings appear upon heating up RNPs. Oligomers which are larger than tetramers have been reported for other orthobunyaviruses and members of other genera within the bunyaviruses (Baklouti et al., 2017; Carter et al., 2012; Dong, H., Li, P., Böttcher et al., 2013; Guo et al., 2012) and were observed here (figure 3.17) but this is the first time they have been observed when derived from a sample of

virus, rather than recombinant protein. Such oligomeric rings were observed after attempting to reconstitute RNPs and appeared to coalesce into even larger complex which began to resemble filaments. The filaments observed in figure 3.17 do not resemble viral RNPs and are more reminiscent of stacked tetramers, but a possible model of orthobunyaviral RNP assembly is that these oligomeric rings are some form of assembly intermediate, which associate with each other and begin to stack to form filaments. There would then be some sort of displacement of monomers within the planar tetramers which produces a continuous helix, similar to the displacement described for TOSV NP (Olal et al., 2014). The observation that the same oligomeric rings also form upon heating RNPs suggests that they may be disassembly intermediates too. A major limitation of this model of orthobunyaviral RNP assembly is explaining how a long RNA is encapsidated effectively by multiple oligomers of NP which each contain a planar, enclosed RNA-binding groove, without leading to the problems described in section 3.1 and illustrated in figure 3.1B. The current model of orthobunyaviral genome replication described in section 1.9.1 (Gerlach et al., 2015) illustrates the complexities of the assembly of new RNPs and it is likely that the process is dependent on the RdRp, potentially in a dimerised state, and the nascent RNA is encapsidated in NP as it exits the replication complex. Simply incubating NP and RNA does not adequately capture the complexities of this process, so it is hard to determine the validity of findings from such experiments, but the observations of changing oligomeric states and formation of filament-like structures may be a starting point to begin to describe the orthobunyaviral RNP assembly process.

Overall, this chapter describes the first detailed characterisation of orthobunyavirus RNPs. It answers the question of the overall architecture of the filaments and shows that only a helical architecture was observed. This agrees with previously published work on BUNV and SBV (Ariza et al., 2013; Reguera et al., 2013). It is in disagreement with the conclusions of other work published on BUNV (Li, B. et al., 2013) although close inspection suggests that the micrographs in this

study may not actually agree with the 'beads on a string' model put forwards by the authors. It also disagrees with work published on LEAV (Niu et al., 2013) although the micrographs presented here were derived from recombinant protein and may differ from viral RNPs. The large amount of negative stain data collected in search of potential polymerase particles allowed subsequent 3D analysis which will make up a large part of the next chapter. The optimisation of a protocol for producing abundant, highly pure RNPs also allowed the project to move forwards and onto the acquisition of cryo-EM data, to further unravel how orthobunyavirus RNPs are assembled.

## Chapter 4

# Determining a three dimensional model of highly flexible BUNV RNPs

### 4.1 Chapter introduction

The previous chapter described the optimisation of a protocol designed to generate abundant, purified BUNV RNPs for EM analysis, as well as the preliminary characterisation of these RNPs from 2D negative staining data. Next, the project focussed on elucidation of a 3D structure, to model the structure of BUNV RNPs, and thus provide a categorical answer to the question of whether orthobunyaviral RNPs are helical or not. Due to its capacity to acquire structural data on large and flexible macromolecular complexes in solution, cryo-EM was selected as the most appropriate and powerful method to achieve this objective.

To date, high-resolution 3D information has been very difficult to acquire on any protein filaments with a degree of flexibility comparable to orthobunyavirus RNPs. Most existing models of viral RNPs are derived from members of the *Mononegavirales* which have very regular, rigid helical RNPs (Gutsche et al., 2015). This ordered structure facilitates EM structure determination and explains why the RNPs of *Mononegavirales* such as RSV, VSV and Ebola virus are more represented in the EM database than their *Bunyavirales* counterparts. Additional structures of complexes formed by viral RNA-binding proteins are those of the coat protein arrays

of Tobacco mosaic virus (TMV), Bamboo mosaic virus (BaMV) and Pepino mosaic virus (PepMV); all positive-RNA plant viruses which again contain rigid, highly ordered, helical filaments (Agirrezabala et al., 2015; DiMaio et al., 2015; Sachse et al., 2007). Of note, the coat protein of PepMV has high structural similarity to the NP of CCHFV, an orthonairovirus (Agirrezabala et al., 2015).

An example of an RNP structure from a segmented, negative-RNA virus which was solved by cryo-EM is IAV. The overall architecture of IAV RNPs was determined by two groups in 2012 (Arranz et al., 2012; Moeller et al., 2012), with one of them imaging RNPs purified from virions and the other one employing reconstituted RNPs derived from recombinant proteins. While these two models were at a comparable resolution (18 Å and 22 Å), the models differed in the handedness

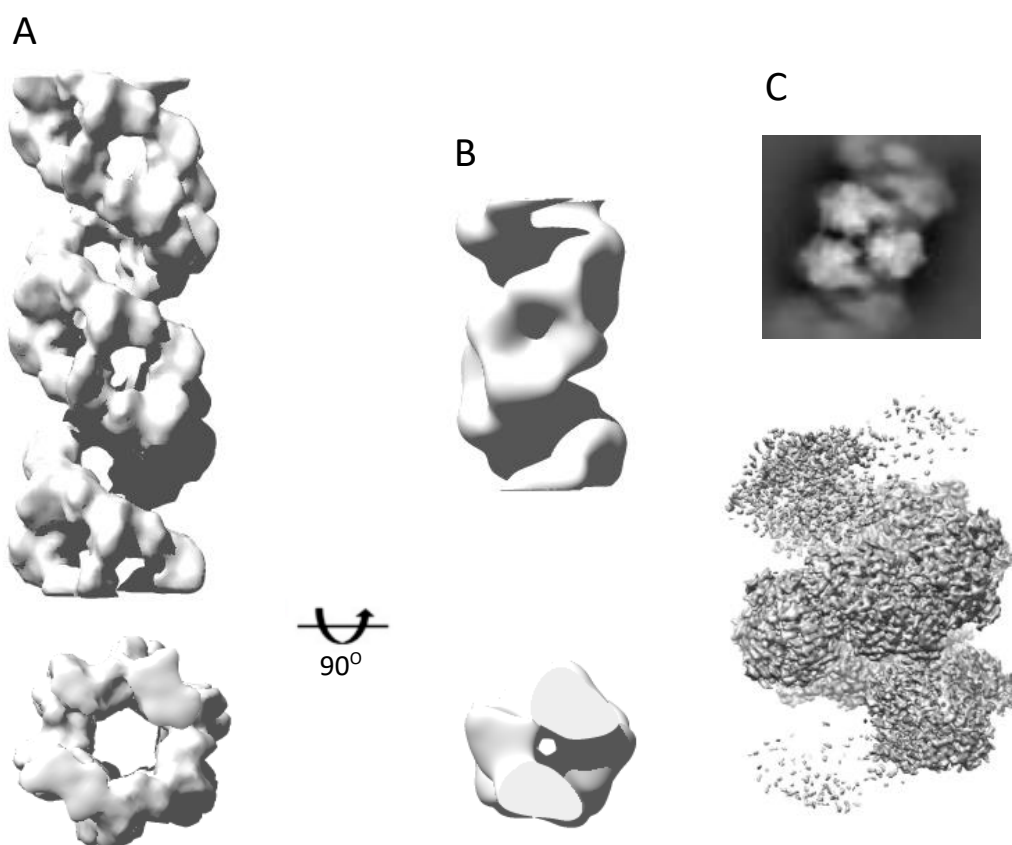


**Figure 4.1:** Models of other flexible protein filaments determined by cryo-EM. Helical models were determined of IAV RNPs, either (A) purified from virions (Arranz et al., 2012) or (B) reconstituted from recombinant NP (Moeller et al., 2012). (C) 2D class averages of AdhE display a similar organisation of monomers to that observed here in BUNV RNPs (top) and a 3.5 Å map was generated by SPA (bottom) (Kim, G. et al., 2019).

of the helix. However, both groups were able to dock the IAV NP crystal structure into density corresponding to NP monomers, and thus propose a model of the gross structural characteristics of the RNPs. Both studies concluded that the long, central sections of IAV RNPs comprise a double helix of anti-parallel chains of NP (figure 4.1A-B). The ambiguity in handedness and the low resolution of these models illustrates the inherent difficulty in high-resolution structure determination of such flexible and dynamic protein complexes. However, the ability to fit crystal structures into the models shows that even for such flexible structures it is possible to gain information on the overall arrangement of protein subunits by EM analysis.

Very few sub-nanometre resolution structures of helical yet flexible assemblies have been elucidated. One recently published example is that of helical filaments formed by aldehyde-alcohol dehydrogenase (AdhE) (Kim, G. et al., 2019). From micrographs it was apparent that these filaments are less flexible than an orthobunyavirus RNP and twice as wide by diameter, and the monomers are about four times larger than an orthobunyavirus NP. However, the 2D class averages of these filaments exhibit a very similar alternating, rising pattern of monomers to that observed here in BUNV RNPs (figure 4.1C), and the high-resolution of the 3D structure suggests that similar resolutions could be possible for BUNV RNPs. The methods employed by the authors involved isolating small particles along the length of a filament, which also proved effective in the analysis of BUNV RNPs.

This chapter describes the efforts to generate a 3D average of BUNV RNPs to a sufficient resolution to reveal how the NP monomers are organised within the RNP filament. Due to the highly flexible nature of the filaments and the lack of contrast in the grids produced, it was very difficult to produce a detailed model from the cryo-EM movies collected. To overcome this, cryo-ET tilt series were collected and STA was used to generate an initial 3D model of BUNV RNPs. This model was then used as a reference for 3D analysis of the negative stain data described in the

previous chapter, leading to the generation of a 3D model of a BUNV RNP in to which previously solved crystal structures could be docked. This model was in agreement with previously published EM and X-ray crystallography and confirms the proposed helical confirmation of the BUNV RNP described in the previous chapter. A discussion then follows that examines the implications of the resulting 3D helical RNP model in terms of its functions during the BUNV replication cycle, and which looks to future efforts to generate a high-resolution model that overcomes the obstacles encountered here.

## **4.2 Initial 3D analysis of negative stain data**

In the course of analysing the negative stain data described in chapter 3, an initial model was generated that exhibited a cylindrical, step-wise arrangement of discrete 'blobs' of density corresponding to an individual NP monomer (figure 4.2A). Extra density was apparent at the ends due to the model being cropped at the edges. No helical architecture could be deduced from this, largely due to the lack of density linking the monomers. This initial model was in turn used as a reference for 3D classification of all ~175000 particles derived from the negative stain data set. The two most populated classes contained 39% and 36% of particles (figure 4.2B, classes 1 and 2). As in the initial model, these classes had a cylindrical arrangement of monomers, although with no clear organisation. However, compared to the most populated class the middle class appeared to contain more complete density in its lower half as pictured, and more NP monomers are visible. The final class (figure 4.2B; class 3) contained the remaining particles and least resembled any of the 2D class averages produced in figure 3.12.

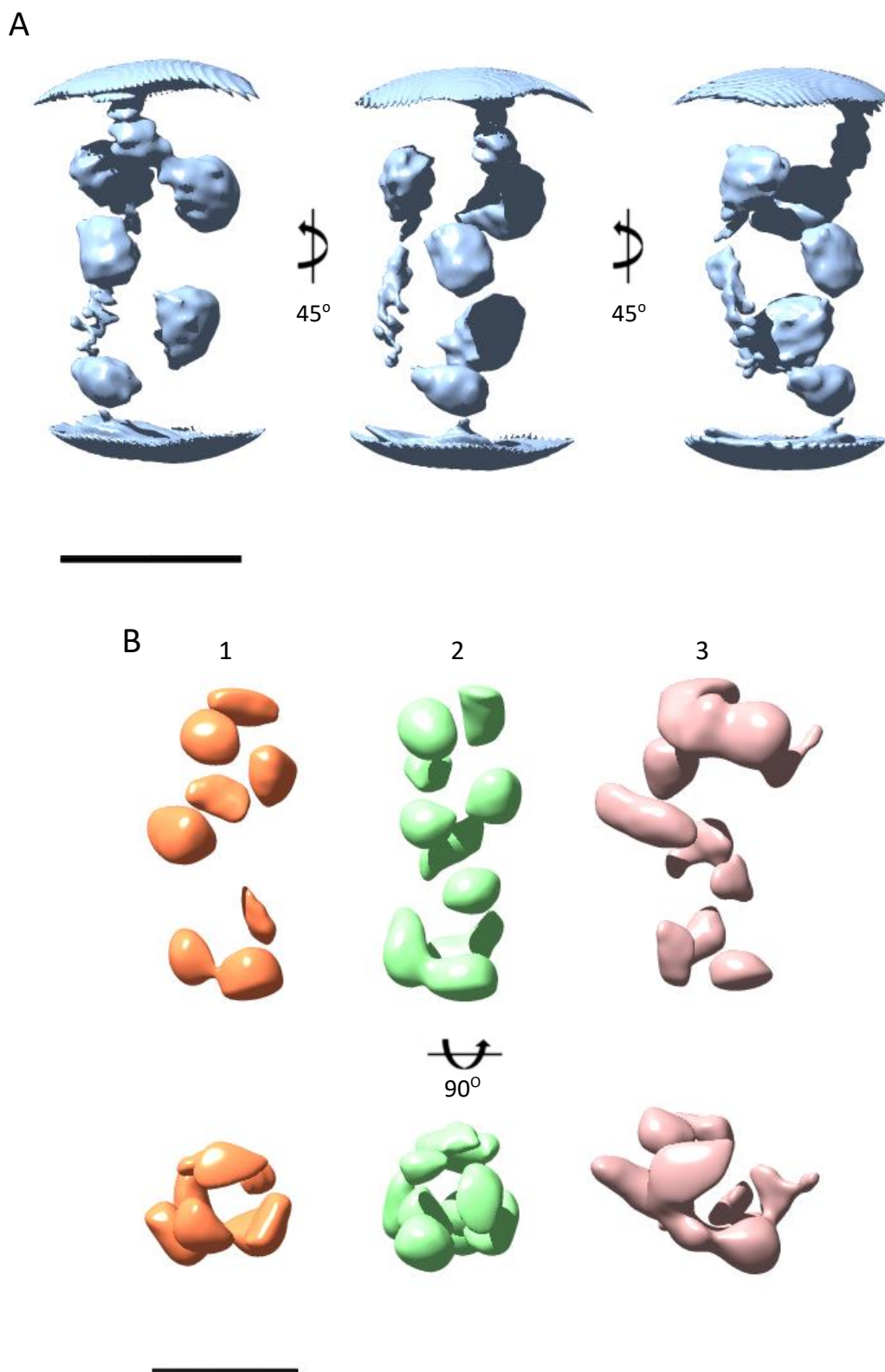


**Figure 4.2:** Initial 3D analysis of negatively stained BUNV RNPs. **(A)** An initial model of the BUNV RNP was generated in Relion from the negative stain data set, and is shown at different orientations. **(B)** Subsequently, the initial model was used as a reference for 3D classification. Models of the three most populated classes are shown; most populated on the left, least populated on the right. Scale bars are 10 nm.

## 4.3 Cryo-ET of BUNV RNPs

### 4.3.1 Cryo-ET tilt series acquisition

BUNV RNPs were purified as described previously in section 3.2 and buffer exchanged into TNE containing 25 mM NaCl and 3  $\mu$ l of the resulting sample was applied to 200-mesh copper grids with a lacey carbon film, replicating as closely as possible the parameters that were previously shown to permit good RNP distribution and optimal data collection in negative stain (section 3.2.5). A range of blotting times and nominal blotting strengths were trialled to optimize ice thickness and sample dispersion and resulting grids were screened on a Titan Krios to determine the optimal conditions. Grids were initially prepared with single particle data collection in mind. However, following a single particle data collection the low contrast of the RNPs made picking and processing the dataset to generate a 3D model very difficult. Therefore, it was decided to re-image the same grids with a Volta phase plate inserted and to acquire a tilt-series data set suitable for tomography. Of note, cryo-ET can generate 3D maps of unique structures without the need of averaging, albeit at a resolution of  $\sim 40$  Å. However, since the grids were originally prepared for single-particle imaging, fiducial markers, routinely used for the alignment of cryo-ET projections, were not added. The lack of fiducial markers was an oversight that may have had some impact on the quality of the downstream tomographic reconstruction.

Single-axis cryo-ET tilt series were collected on a Titan Krios microscope operating at 300 kV with a Volta phase plate inserted, at a nominal magnification of 45000x, with each tilt series ranging from -60 to +60 degrees at 2 degree intervals. Due to the size and physical characteristics of the RNPs combined with the relatively low magnification at which locations are selected for data collection, RNPs were not readily visible while selecting these areas. However, since the grid had already been used to collect an SPA data set in which RNPs were evenly dispersed throughout the sample, tilt series were collected 'blindly' from thin, apparently clear patches of ice

assuming that the RNPs would be present in these locations. A total of ten series was collected successfully and within these, some RNPs were immediately visible (figure 4.3). Within these raw micrographs from the tilt series, large dark particles were also clearly visible which had not been present when the same sample was negatively stained. These particles could not be explained and were attributed to ethane contamination, although it is acknowledged that ethane contaminants are usually more sharply defined and more electron transparent, and this is not a completely satisfactory explanation.

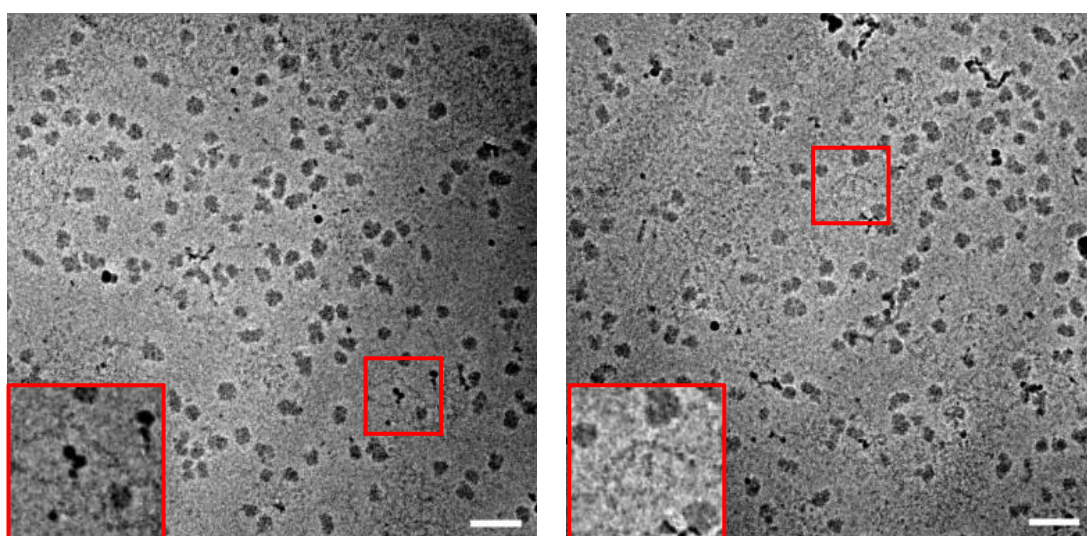


**Figure 4.3:** Raw micrographs from two different tilt series. RNPs are not visible but were known to be present from previous single particle data collection. The large, dark particles were not present when this sample was negatively stained and imaged previously and are attributed to ethane contamination which possibly occurred during vitrification. Insets in each micrograph show magnified sections highlighted in red, and indicate visible RNPs. Scale bars are 100 nm.

Using eTomo within the IMOD software package the collected tilt series were aligned without fiducial markers, and these aligned tilt series were then reconstructed into tomograms by weighted back projection. Within tomograms (figure 4.4A) the electron-dense contamination clearly visible within the raw micrographs appeared more pronounced but did not obscure any of the visible RNPs. Other smaller, dark contaminants also became visible in reconstructed tomograms, which appeared in patches and which had also not been visible when negatively stained. Of note, and

discussed later in this chapter, the RNP filaments appeared very clearly and had a high contrast in these micrographs. The filaments also appeared to be spread out (figure 4.4B), which in combination with the higher contrast from the phase plate aided greatly with selecting particles from RNPs for STA.

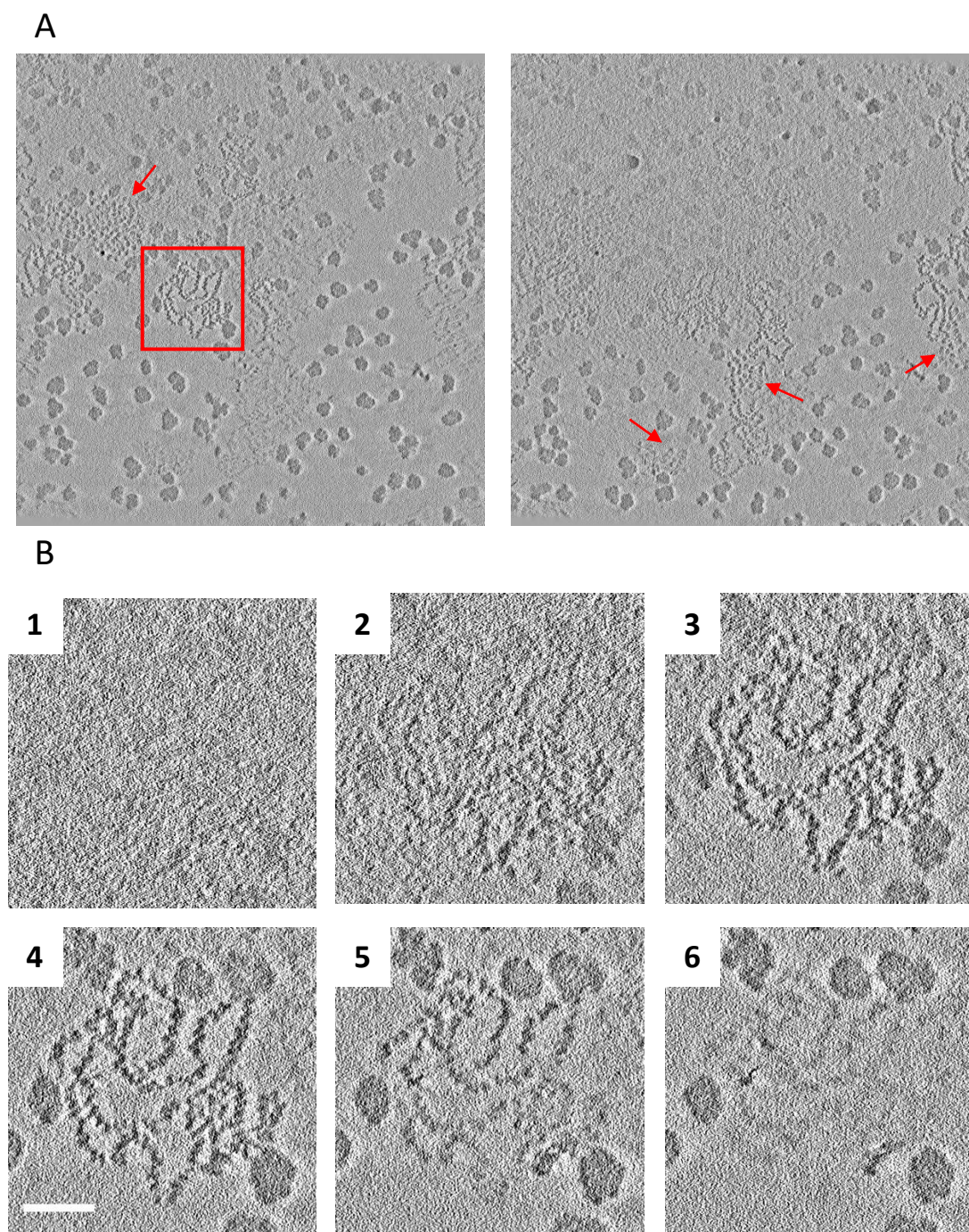


**Figure 4.4:** Reconstructed tomograms of purified BUNV RNPs. **(A)** Whole, reconstructed tilt series revealed clear RNPs and numerous electron dense particles. Red arrows indicate patches of smaller, denser unidentified contaminants. Images are of slices of the same tomogram, 54 Å apart. **(B)** Slices through the area boxed in red in (A), 27 Å apart, which is centred on an area displaying clear RNP(s). Scale bar is 50 nm.

### 4.3.2 Sub-tomogram averaging (STA)

Tomography data is inherently affected by the missing wedge problem, described in section 1.13.6, and computational approaches to recover the unacquired data results in distortion of the final reconstruction, particularly when the data is only collected on a single axis. The best way to compensate for this limitation is to perform STA. In this method, homogeneous particles with missing wedges in different directions are averaged, thus filling the missing information; additionally, this approach increases the signal-to-noise ratio of the volume of interest (in this case, BURENV RNPs), increasing the resolution of the final 3D volume. Particles for sub tomogram averaging were selected along RNPs by manual tracing (figure 4.5). In order to capture one complete turn of the helix (a distance termed helical pitch) with each particle picked, particles were picked at 10 pixel intervals along the traced filaments, which corresponded to 54 Å intervals (pixel size was 5.4 Å). This separation was decided after estimating the BUNV RNP helical pitch to be between 50 and 60 Å, by using the previously published helical crystal structure of the LACV RNP (Reguera et al., 2013) and the measurements derived from the negative stain analysis in this project (figure 3.13).

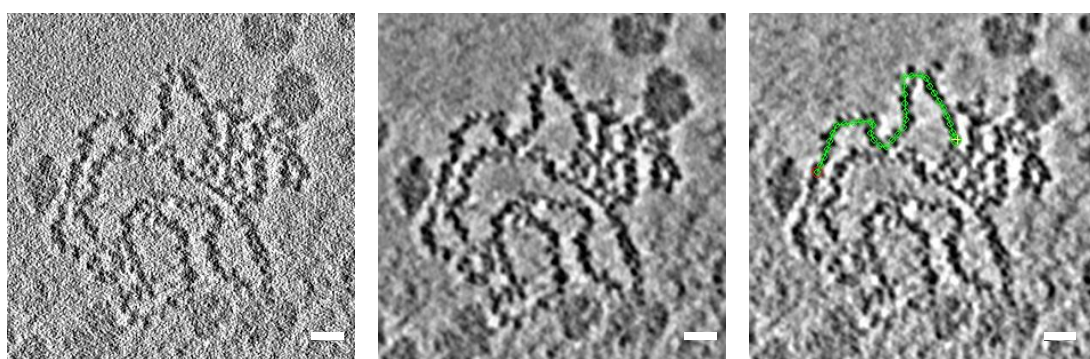
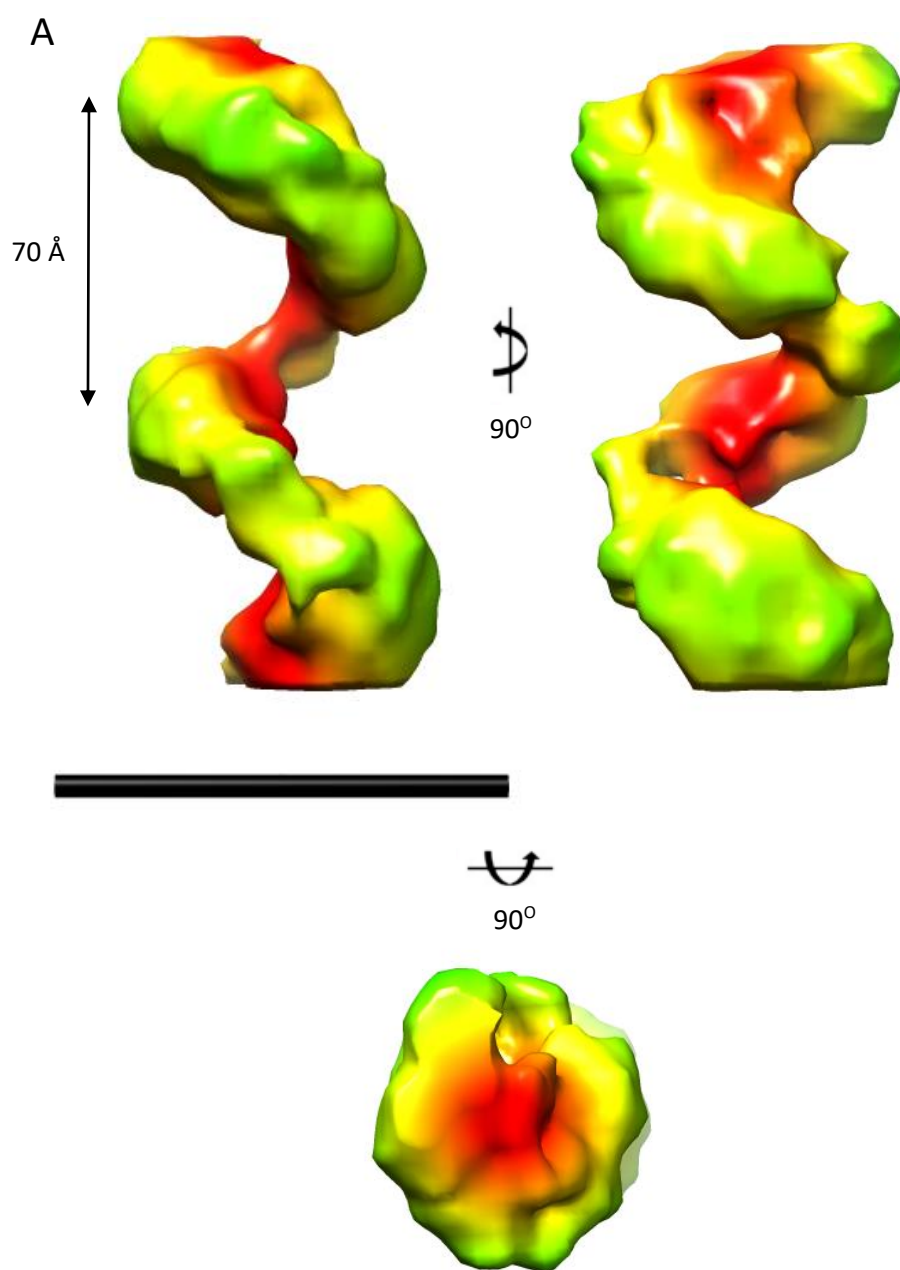


**Figure 4.5:** Placing model points along RNPs for STA. Reconstructed tomograms (left) were filtered by Gaussian blurring (middle), and RNPs were manually traced in 3dmod (right, green). These traces were used to place points to select particles for STA from the original tomograms. Scale bars are 20 nm.



**B**

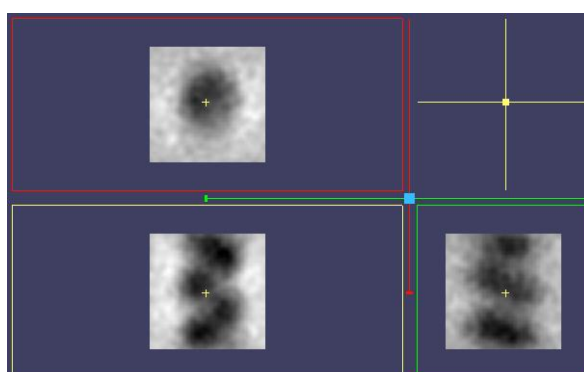


**Figure 4.6:** Sub tomogram averaging of BUNV RNPs. **(A)** 3D density of the helical model generated by STA coloured by cylinder radius, red in centre towards green at edge, at different orientations. **(B)** XYZ representation of the model in (A). Scale bar is 10 nm.

Initial STA jobs were run to align all subtomograms consistently, using a cylinder as reference. This was achieved through only refining the orientations of the subtomograms, without refining the RNP rotation along their own axes. This resulted in a continuous cylinder of the correct diameter. Subsequent PEET refinements began to use angular searches in all angles to find the parameters of the helix, including rotation. This was initially done on a small number of particles to minimise computing costs while finding the optimum parameters. More particles were added until no further improvements in resolution were gained. The final resolution, at an FSC cut-off of 0.5, was 23 Å.

When viewed in 3D the model produced in PEET by STA showed a clear helical architecture but density for individual discrete NP monomers could not be distinguished and crystal structures could not be accurately docked into the density (figure 4.6A). Despite the monomers not being apparent when viewed in 3D, when it is viewed in XYZ then individual subunits become apparent (figure 4.6B). The helix shown appears to be narrower in diameter than had been estimated for an orthobunyavirus RNP and a full helical turn had a pitch of approximately 70 Å when measured in the 2D sections, which is larger than estimated from negative stain data (figure 3.13A).

## 4.4 3D model of BUNV RNPs from negative stain data

### 4.4.1 3D analysis of negative stain data with a reference from cryo-ET

The helical model that had been derived from STA (figure 4.6) was rescaled to the same box size and pixel size as the negative stain data and re-orientated to the standard helical direction used within Relion (Heymann et al., 2005). An initial round of 2D classification was performed on the particles that had previously been extracted for the 2D negative stain analysis and classes that corresponded to bent RNPs or junk particles were discarded, leaving a total of ~120000 particles. These remaining particles were 3D classified against the rescaled and re-orientated STA model into five further classes. The three most populated classes exhibit the clearest arrangement of density corresponding to monomeric NP. Side views exhibit flat density at the top and bottom of the models but show a number of individual densities in the middle arranged in a helical pattern. Top down views also differ from each other with only classes 2 and 3 exhibiting a tight cylindrical arrangement when viewed along this axis.

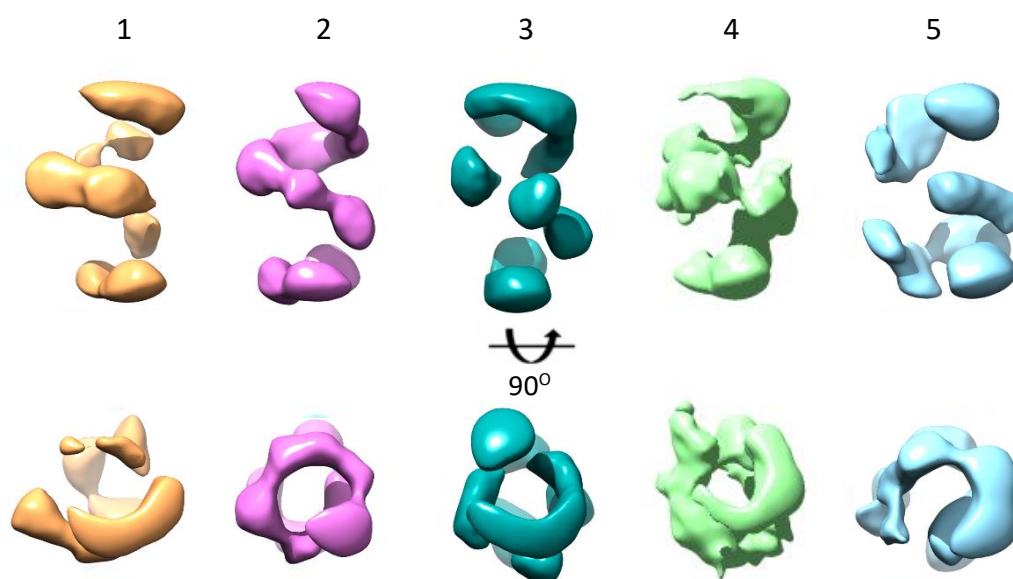


**Figure 4.7:** First round 3D classification of negative stain EM data, using a cryo-ET derived model (figure 4.6A) as a reference. Models of the five most populated classes are shown; most populated on the left, least populated on the right. Scale bar is 10 nm.

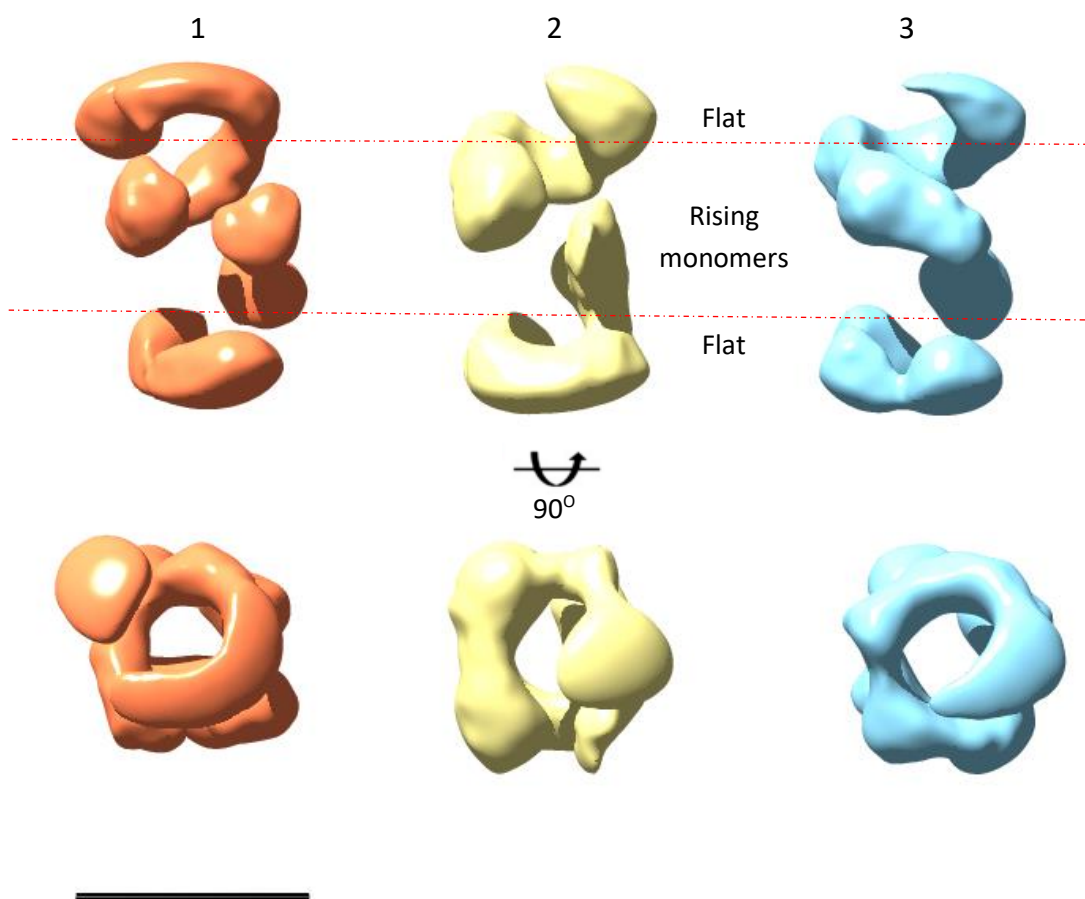


**Figure 4.8:** Second round 3D classification of negative stain EM data, using a cryo-ET derived model (figure 4.6A) as a reference. Models of the three most populated classes are shown; most populated on the left, least populated on the right. Red dashed lines divide regions of flat density from the central rise of monomers. Scale bar is 10 nm.

Three different subset selection jobs were carried out on the 3D classes shown in figure 4.7. These corresponded to class 1; classes 1 and 2; and classes 1, 2 and 3 respectively. The selected particles were in turn 3D classified again, against the tomography model, into a further three classes.

Of these, the models generated from classes 1 and 2 in figure 4.7 looked the most homogeneous and the most like a helix with clear individual monomers (figure 4.8). These classes together comprised ~55000 particles and exhibited more homogeneity than the previous round (figure 4.7). Side views showed the same pattern of flatter density at the top and bottom and a rise of monomers in the middle. Top down views showed more consistent widths along the length of the filament compared to the classes from the previous round (figure 4.7).

The most populated class from the second round of 3D classification (figure 4.8) was used as a reference to refine the ~55000 particles classified in figure 4.8. The resulting model had the same overall pattern observed in the two rounds of 3D classification. The NP monomers at the bottom as viewed here, are arranged in a flat, planar manner but a helical twist of monomers can be seen rising to the top of the model (figure 4.9). The top down view shows a distinct arrangement of monomers at  $90^\circ$  angles to their neighbours, resembling previously published crystal structures of tetrameric orthobunyavirus NP. However, this pattern of monomers arranged at  $90^\circ$  to each other did not continue down the whole length of the model and in the bottom left of the top down view (figure 4.9, circled) an NP monomer towards the bottom of the model is offset relative to the organisation of the ones above it.

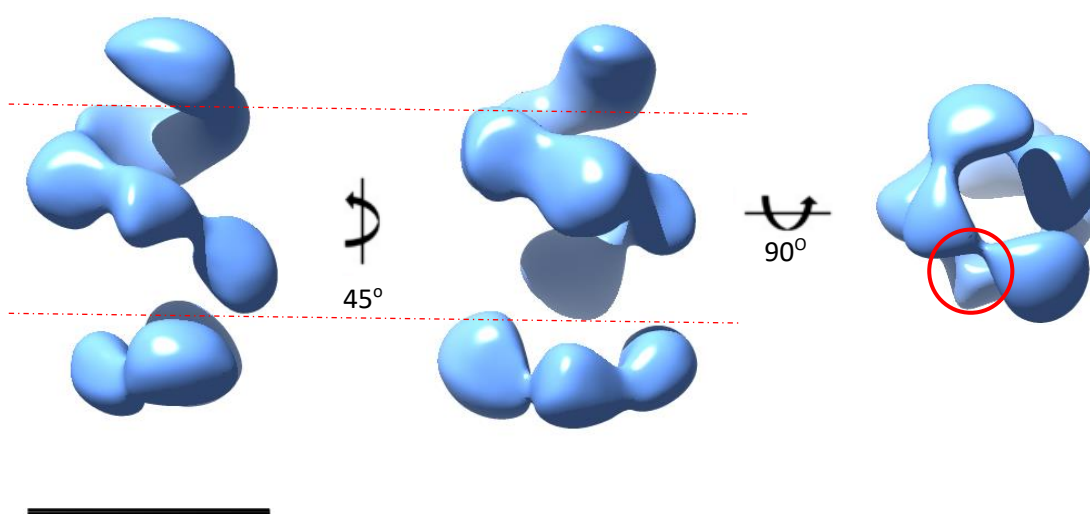


**Figure 4.9:** 3D refinement of the top particles from negative stain data, at different orientations. No helical symmetry was applied. Red dashed lines divide regions of flat density from the central rise of monomers, as in figure 4.8. Scale bar is 10 nm.

This was the first 3D model generated to display clear density for discrete NP monomers which somewhat resembled a helix and the first in which the top down view showed an arrangement of NP similar to that of a tetramer, albeit with a helical rise. Of note, this model was generated without the application of any helical

symmetry, despite the close resemblance to the helix expected from the negative stain data. The next step was to apply helical symmetry in order to produce an idealised model of the RNP at its straightest sections.

#### 4.4.2 Helical Symmetry

The most populated class from figure 4.8 was again used as a reference to refine the top ~55000 particles, but this time with the application of helical symmetry. A mask around the helical RNP was generated with an outer diameter of 120 Å. The helical parameters employed were a twist (i.e. the angle between two consecutive NP monomers) of 90° and a rise 18 Å (i.e. the distance along the helix direction between two NP monomers). Thus far the helix has been described in terms of helical pitch, but the input parameters in Relion specify a helical rise, not pitch. The values for initial twist and rise were taken from previously published crystallography data of tetrameric NP (Ariza et al., 2013; Niu et al., 2013; Reguera et al., 2013) and the negative stain EM data presented in figure 3.13. Local searches of symmetry were

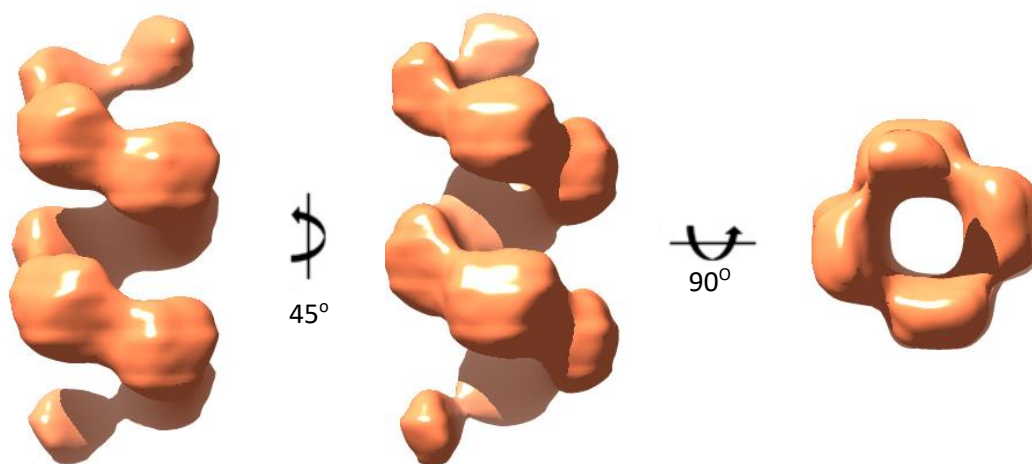


**Figure 4.10:** Optimising the 3D refinement of negative stain data with helical symmetry applied. Model with angular search ranges and correct handedness shown at different orientations. Initial twist was set at  $-90^\circ$  and rise at 18 Å and local searches of symmetry were applied. Scale bar is 00 nm.

also applied in a small range around the chosen helical parameters. The resulting model exhibited very clear helical characteristics with a pattern of subunits that bears some resemblance to the stepwise, rising pattern of monomers observed in the 2D data in section 3.3. However, several issues with this model are immediately apparent. Namely, the empty core of the filament as seen in the top down view is too wide and prominent striped artefacts run horizontally across the entire model. These issues suggest that the helical parameters required further optimisation to generate a better model.

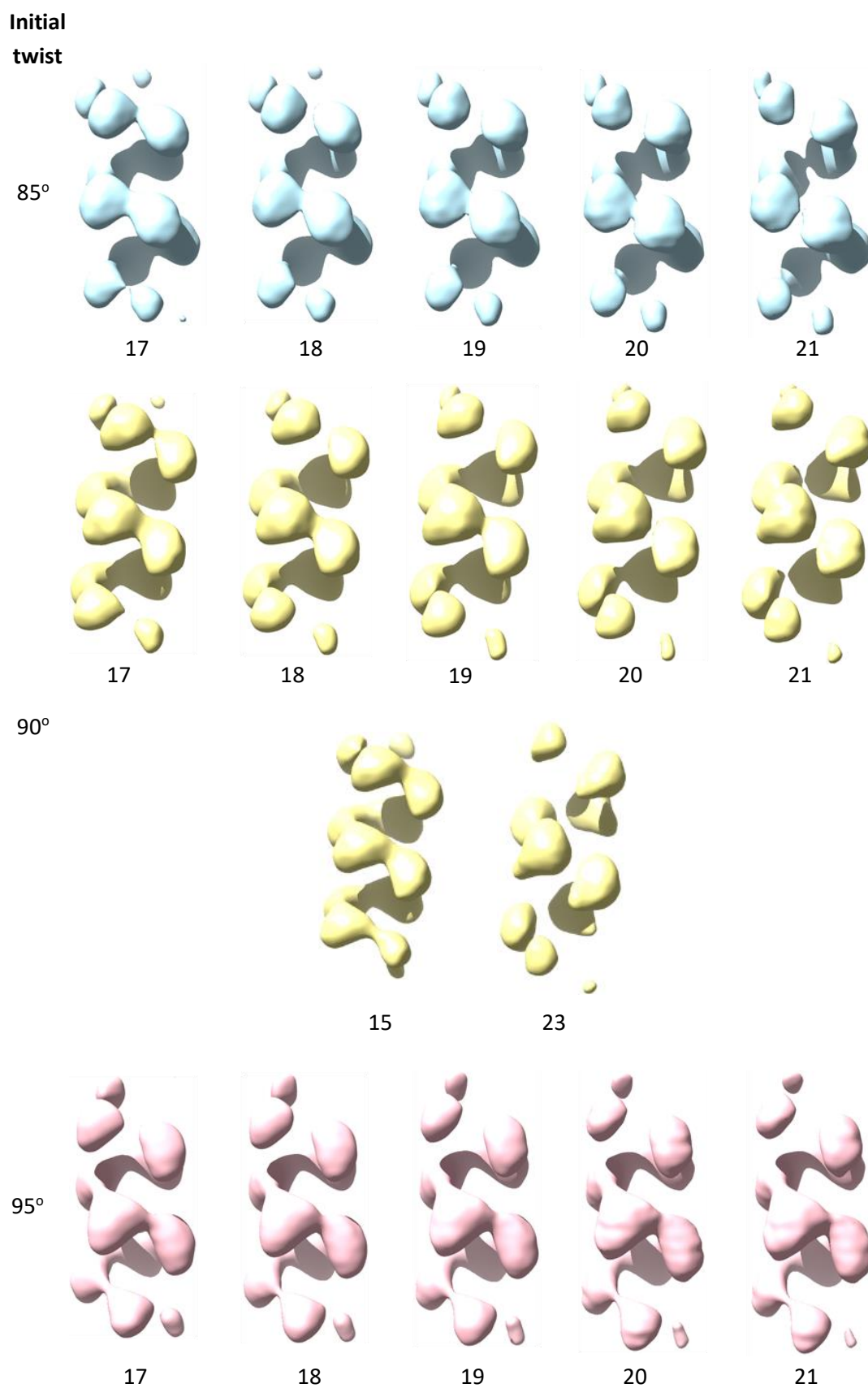


**Figure 4.11:** A range of helical parameters were applied in Relion to calculate a 3D refinement. Initial twist ranged between 85° and 95° and the initial rise ranged between 15 and 23 Å (shown below each model).

Thus far, it has been confirmed that BUNV RNPs are helical and approximate values for the helical twist and pitch had been determined. However, repeating the helical reconstruction of the negative stain data using a range of values for helical pitch generated models that all looked very similar and that all had the same resolution according to Relion (figure 4.11). However, there were still differences in the quality of the produced models and red asterisks within figure 4.11 indicate models produced with an initial twist of  $85^\circ$  or  $95^\circ$  where the previously seen striped artefacts remained, or which lacked density joining NP monomers.

The question therefore arose of which helical rise was correct to use for helical reconstruction, and would generate the best model of a helical BUNV RNP with the available data. To this end, a series of ideal helices were produced from spheres, with helical rises ranging from 14 to 20 Å (figure 4.12A-B). Each helix in turn was then fitted into the density of the model derived from STA using UCSF Chimera (figure 4.12C) and a value for the correlation between the fitted helix and the STA model was output. The helix which scored the highest correlation was that with a pitch of 16 Å and so a final refinement was performed with this value used to apply helical symmetry.

Having established the best parameters to use for helical reconstruction, these were applied to a refinement of the particles that had been picked from negative stain micrographs. The resulting model (figure 4.13A) exhibited a clear, rising pattern of subunits, which when viewed from the side bore a close resemblance to the pattern of monomers observed in an RNP in 2D class averages. The striped artefacts that had persisted since the first helical reconstructions were absent in this model.

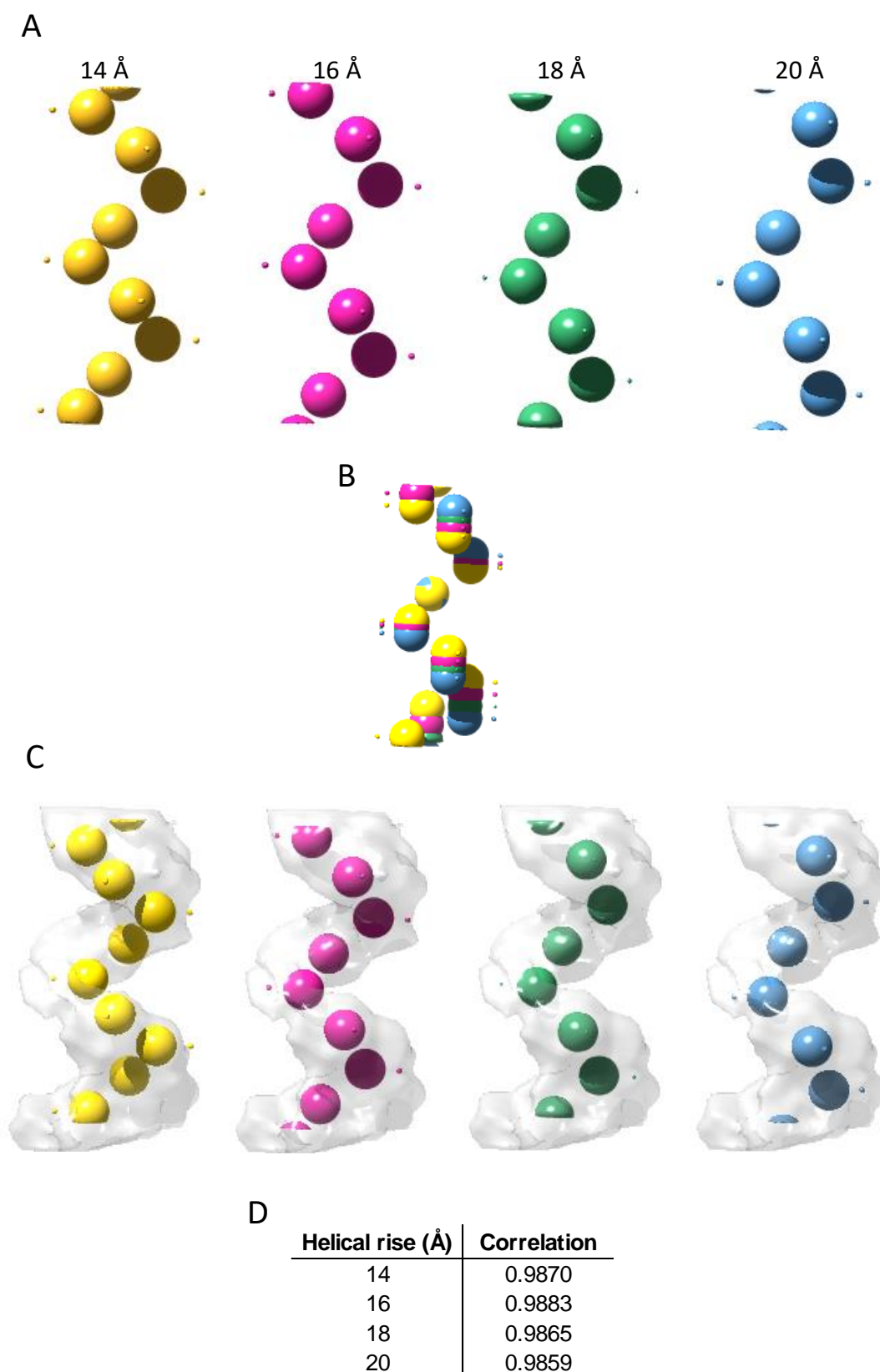


**Figure 4.12:** Generating ideal helices to test parameters for refinement of negative stain data. **(A)** Helices of 14, 16, 18 and 20 Å pitch were produced in bsoft. **(B)** Direct comparison of the ideal helices produced. **(C)** Each helix in turn was fitted into the density from STA and the correlation was measured with UCSF Chimera to find the best fitting helix. **(D)** The correlations of each helix as measured in UCSF Chimera.

The crystal structure of a single BUNV NP monomer was docked into the density for the individual subunits in this model, and this fits in a manner in which the RNA binding groove faced the interior of the filament and the N- and C-terminal oligomerisation arms were clearly able to contact their neighbouring monomers (figure 4.13B). The oligomerisation arms in the crystal structure extend at distinct angles to facilitate the formation of the flat and closed tetramer in which the NP crystallised. In the model presented here the arms of an individual NP monomer appear to protrude directly into their neighbours but this is simply an artefact of docking the structure of NP from a closed tetramer into the helical model. The arms of orthobunyavirus NP display such a high degree of flexibility that they would be able to adopt a conformation that allows them to correctly interact with neighbouring monomers in the context of the helix described here (see discussion, section 4.5.2).

When viewed from the top down the model presented here clearly displays the four subunits binding to each other at  $90^\circ$  angles that had been hypothesised and was also evident in flat, closed tetrameric rings (figure 4.13C). When the crystal structure of an RNA bound NP tetramer was overlaid on the top down view of the helical model, the globular cores of the individual NP monomers matched the location of subunits within the filament (although they did not fit in the helical RNP model, as each monomer is at a different height). Thus the arrangement of monomers within the helical average is similar to the tetrameric NP crystal structure, which contained RNA; therefore it is likely that this helical NP arrangement allows the encapsidation of the viral RNA.

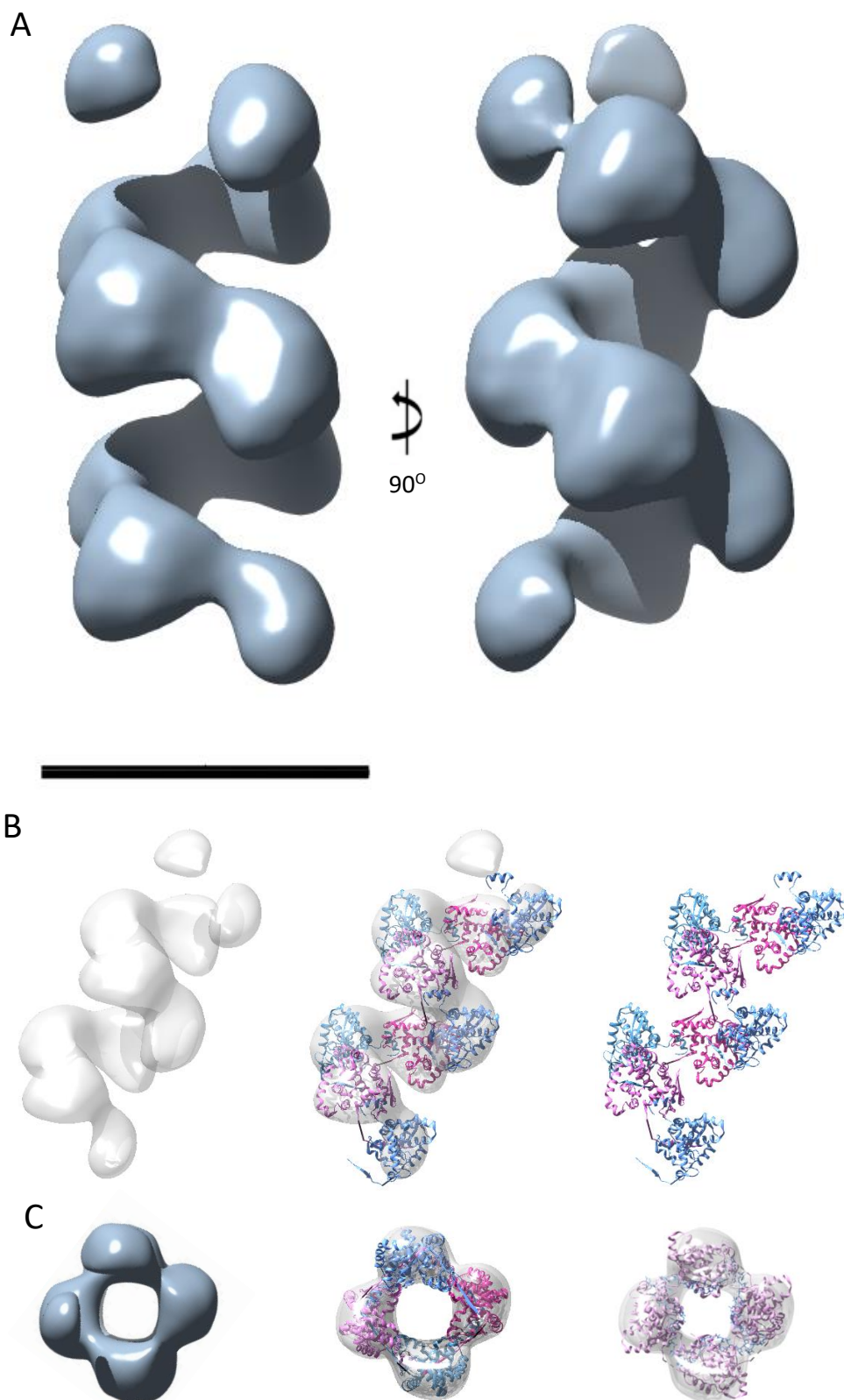


**Figure 4.13:** A helical 3D model of BUNV RNPs. **(A)** Negative stain data was refined using the STA result as initial reference, and helical symmetry applied to generate a model of a BUNV RNP. **(B)** NP crystal structures could be docked into the density in (A) to show their organisation in more detail. **(C)** The top down views of (A) and (B) showed the “tetrameric” basis of the helix (left and middle). The crystal structure of tetrameric RNA bound NP overlaid on the top down view (right) closely fits the EM density from this view, although it should be noted it does not fit along the axis of the RNP. Scale bar is 10 nm.

## 4.5 Cryo-EM of BUNV RNPs

### 4.5.1 Cryo-EM data collection

Cryo-EM movies were collected and upon viewing the micrographs in Relion, it was apparent that the RNPs were difficult to distinguish due to the low contrast (figure 4.14A). An initial auto-picking with Laplacian-of-Gaussian filtering failed to accurately detect meaningful particles and instead indiscriminately selected objects across almost the entirety of each micrograph (4.14C).

As an alternative, ~1,000 particles were picked manually and an initial set of 2D classes was produced. The most populated classes which most closely resembled previous 2D averages of RNPs (figure 4.14B) were selected and used for reference based autopicking. This method of autopicking had the same issue as the Gaussian autopicking, of being unable to select RNPs and simply placing particles over the entirety of the micrograph.

The resulting classes produced from this initial set of manually-picked particles (Figure 4.14B) exhibited the same gross characteristics as had been seen with the negative stain class averages, with similar discrete and alternating patches of density along the long-axis of the particle. Therefore, although labour intensive, manual picking was employed across all micrographs, placing particles wherever an RNP could be distinguished by eye (figure 4.14A). A total of ~30,000 particles were picked that covered a range of defocus values. This did not cover all of the available micrographs but further particle picking was limited by time constraints and the taxing nature of picking particles in this manner. The ~30000 particles that were picked were 2D classified and the resulting classes exhibited the alternating pattern of monomers (figure 4.14D) that had been observed in the negative stain data.

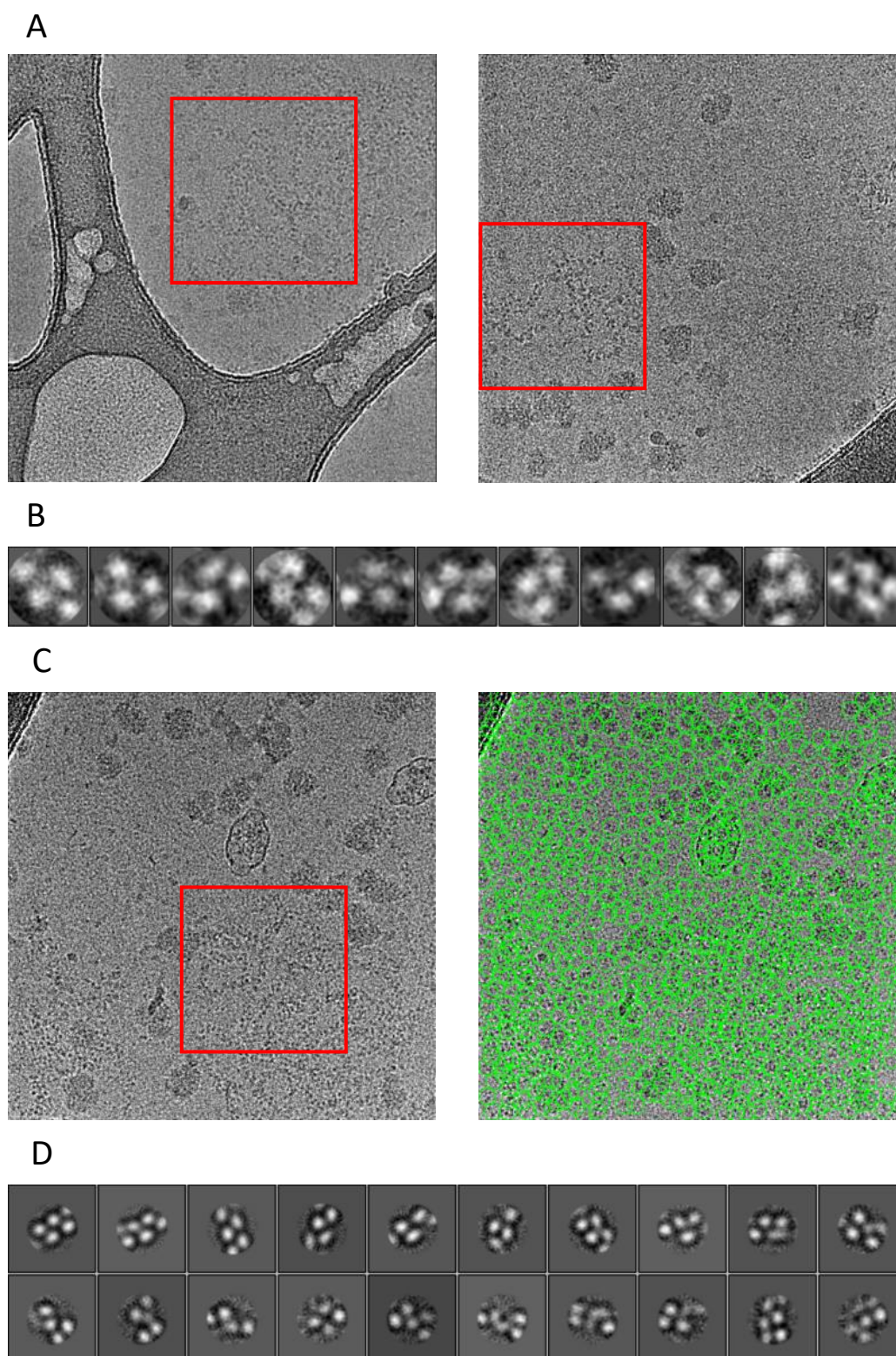


**Figure 4.14:** 2D cryo-EM of BUNV RNPs. **(A)** Representative micrographs of BUNV RNPs illustrate the difficulty in selecting clear, straight sections of RNP filament. Visible sections of RNP are indicated. **(B)** 2D classes were generated in Relion from manually picked particles and were highly similar to the negative stain 2D classes in chapter 3. **(C)** Autopicking was unable to distinguish RNP filaments, despite the visible RNPs indicated. Left = before autopicking. Right = after autopicking. **(D)** Most populated classes following a 2D classification of manually picked particles.

This confirmed that the cryo-EM micrographs did contain RNPs and that their gross appearance closely agreed with all of our assumptions and observations about their organisation made up to this point. The evidence of RNPs being present in the micrographs and amenable to 2D analysis also raised the possibility that 3D information could be gathered from them too.

#### **4.5.2 3D analysis of cryo-EM data**

The most highly populated classes from the 2D classification of manually-picked cryo-EM particles (figure 4.14D) were selected and used to generate an initial 3D model in Relion without imposing helical symmetry (figure 4.15A). Within the resulting model discrete, round patches of alternating density corresponding to NP monomers, which had been seen consistently throughout the 3D EM analysis, were present and organised in a linear, filamentous way. The density corresponding to these monomers did not contain any linking density that would be suggestive of oligomerisation and the entire model lacked a clear organisation.

The initial Relion model (figure 4.15A) was used as a reference for 3D classification of the ~30000 picked particles into three classes (figure 4.15B). The most populated class contained 60% of all particles and had an arrangement of NP monomers that showed no order when viewed from the side but which bore some resemblance to an NP tetramer, and to the helical negative stain model (figure 4.13A) when viewed from the top down. The middle class contained 38% of particles and also lacked an obvious helical organisation when viewed from the side, but the density for individual monomers appeared to adopt the same positions as in the most populated class. The remaining 2% of particles made up the final class. That the particles fell almost entirely into two classes and these looked so similar suggests a degree of homogeneity in the particles and raises the possibility that with more work BUNV RNPs could be made amenable to high-resolution structure determination by cryo-EM. Indeed, if all available particles were manually picked then the data collected

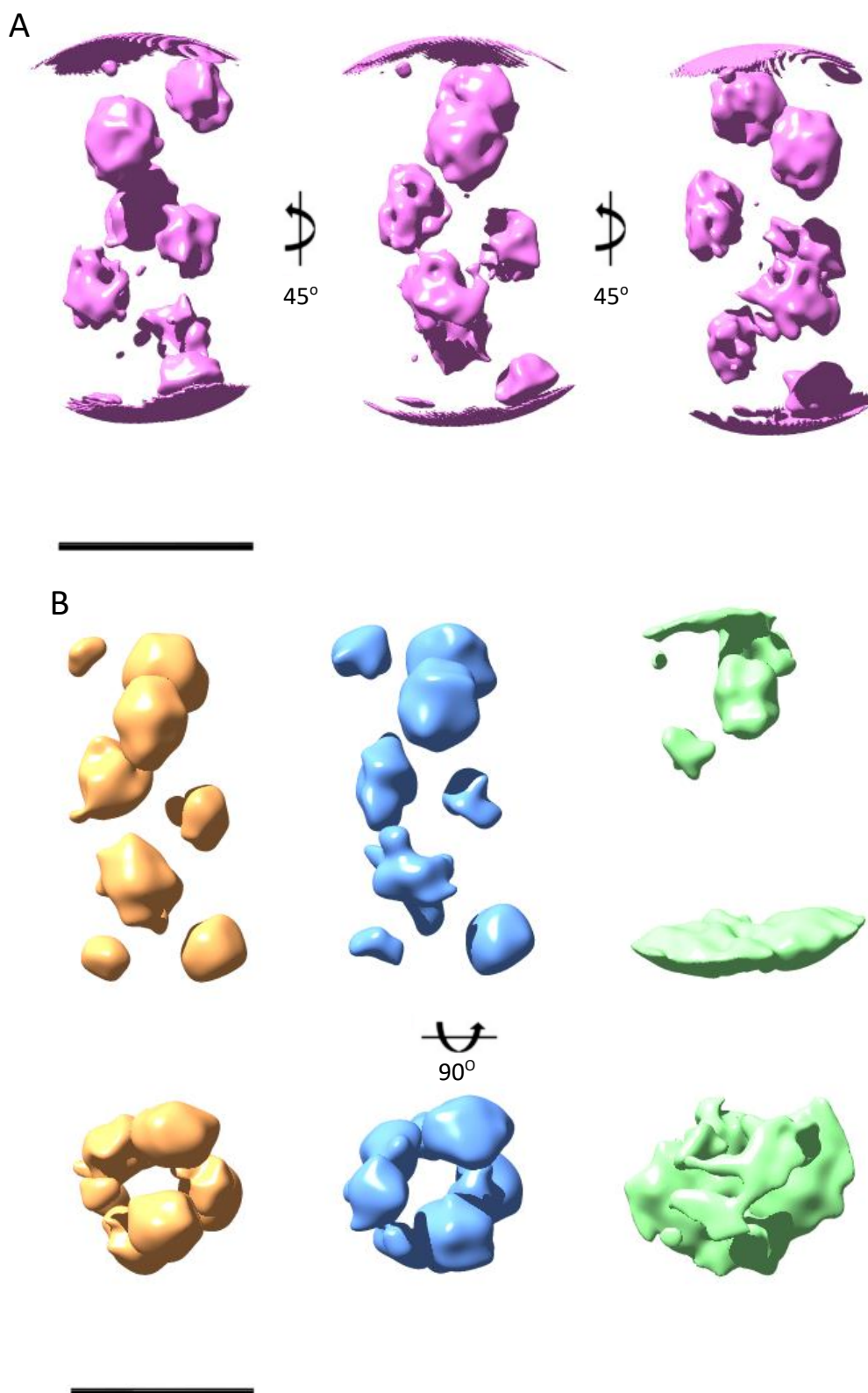


**Figure 4.15:** 3D analysis of BUNV RNPs from cryo-EM. **(A)** An initial model of the BUNV RNP was generated in Relion 3.0 from the cryo-EM data set, and is shown at different orientations. **(B)** Subsequently, the initial model was used as a reference for 3D classification. Models of the three most populated classes are shown; most populated on the left, least populated on the right. Scale bars show 10 nm.

here could potentially be processed to a higher resolution. The 3D model generated from the negative stain data with helical symmetry applied was used as a reference for refining the ~30000 particles picked from cryo-EM micrographs. However, these are not shown as they were almost indistinguishable from the 3D models in figure 4.15B, and suggest that fundamentally, better sample preparation will be required before useful cryo-EM data can be obtained.

### **4.5.3 Cryo-EM with phase plate**

A final cryo-EM data set for SPA was collected from newly made grids, prepared as previously described, with a Volta phase plate inserted. Collecting cryo-ET data with the Volta phase plate (figure 4.4) and SPA data without it (figure 4.14) from the same grid demonstrated the marked effect that the phase plate had on sample contrast, which was the key determinant in the ability to pick particles. It was assumed that collecting a data set with the phase plate inserted would enable the Relion autopicker to function effectively and pick particles of sufficient number and quantity for subsequent processing.

Cryo-EM movies were collected and upon viewing them in Relion it was apparent that, with the phase plate inserted, RNPs were much more clearly visible (figure 4.16A). Class averages were produced from ~1500 manually picked particles and these were used as a template for auto picking. Although many junk particles were also picked, particularly from the previously described unidentified electron-dense contaminants, the Relion autopicker was able to select most of the available RNP particles. The large number of junk particles also picked were isolated and discarded after the first round of 2D classification, and after several more rounds of classification a relatively homogenous set of RNP containing particles was left (figure 4.16B). This first round of classification was carried out with particles extracted with a relatively large box size that encompassed multiple turns of the proposed helix, in order to identify the straightest sections of RNP following alignment. Resulting

classes exhibited the alternating pattern of monomers which indicated a regular, helical architecture and which had been observed in all previous 2D classifications throughout the project.

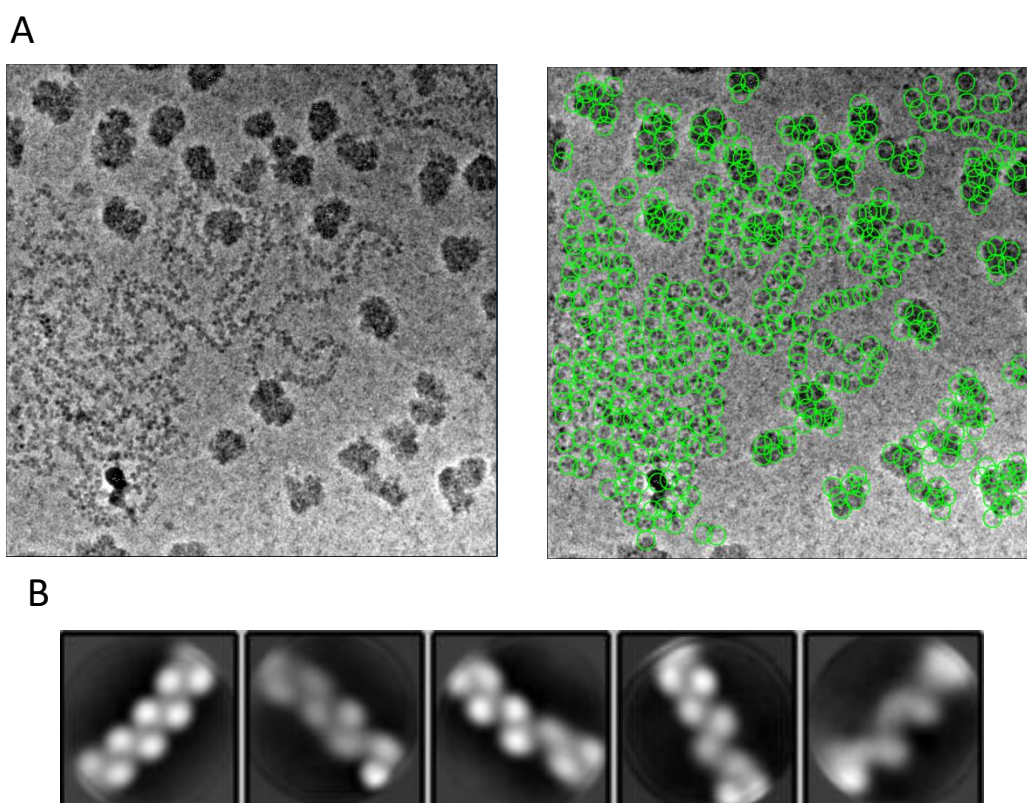


**Figure 4.16:** 2D analysis of BUNV RNPs from a cryo-EM data collection aided by a phase plate. **(A)** A representative micrograph of BUNV RNPs illustrates the increased contrast when a phase plate was inserted during data collection. This permitted efficient autopicking in Relion. Left = before autopicking. Right = after autopicking. **(B)** 2D classes were generated from manually picked particles and appeared highly similar to all of the 2D classes produced previously from both negative stain and cryo-EM data.

The set of homogenous particles identified by 2D classification was subject to 3D classification using a number of different references; the STA model (figure 4.6), the negative stain model (figure 4.13), or a cylinder of 100 nm width. All of the resulting classes looked very similar but the ones produced with an STA-derived reference had the most clearly defined features, so these classes were used to carry out further rounds of 3D classification to identify a smaller and more homogenous dataset. The coordinates of this final subset of straight RNP particles were re-extracted with a smaller box size in order to isolate shorter segments of filaments. It was reasoned that these particles would be more homogenous because isolating shorter segments would, to some extent, mitigate the curvature of the very flexible filaments.

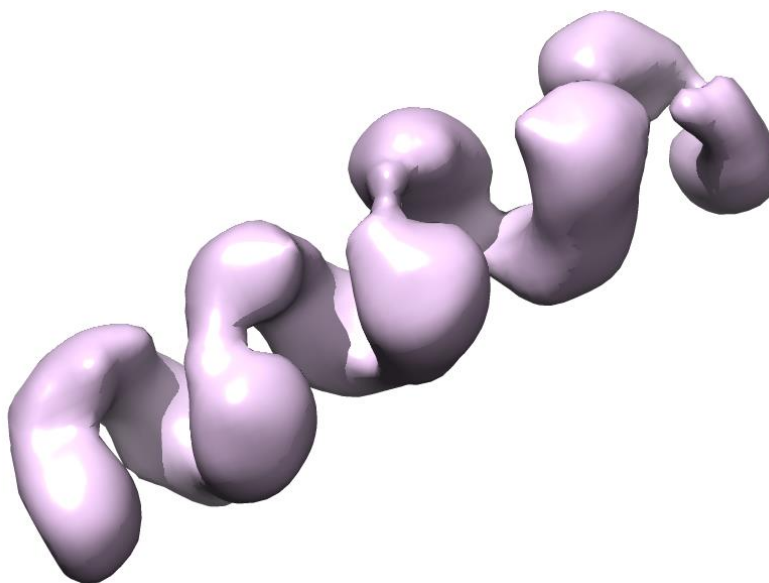


**Figure 4.17:** A helical 3D model of a BUNV RNP, generated from cylindrical reference.

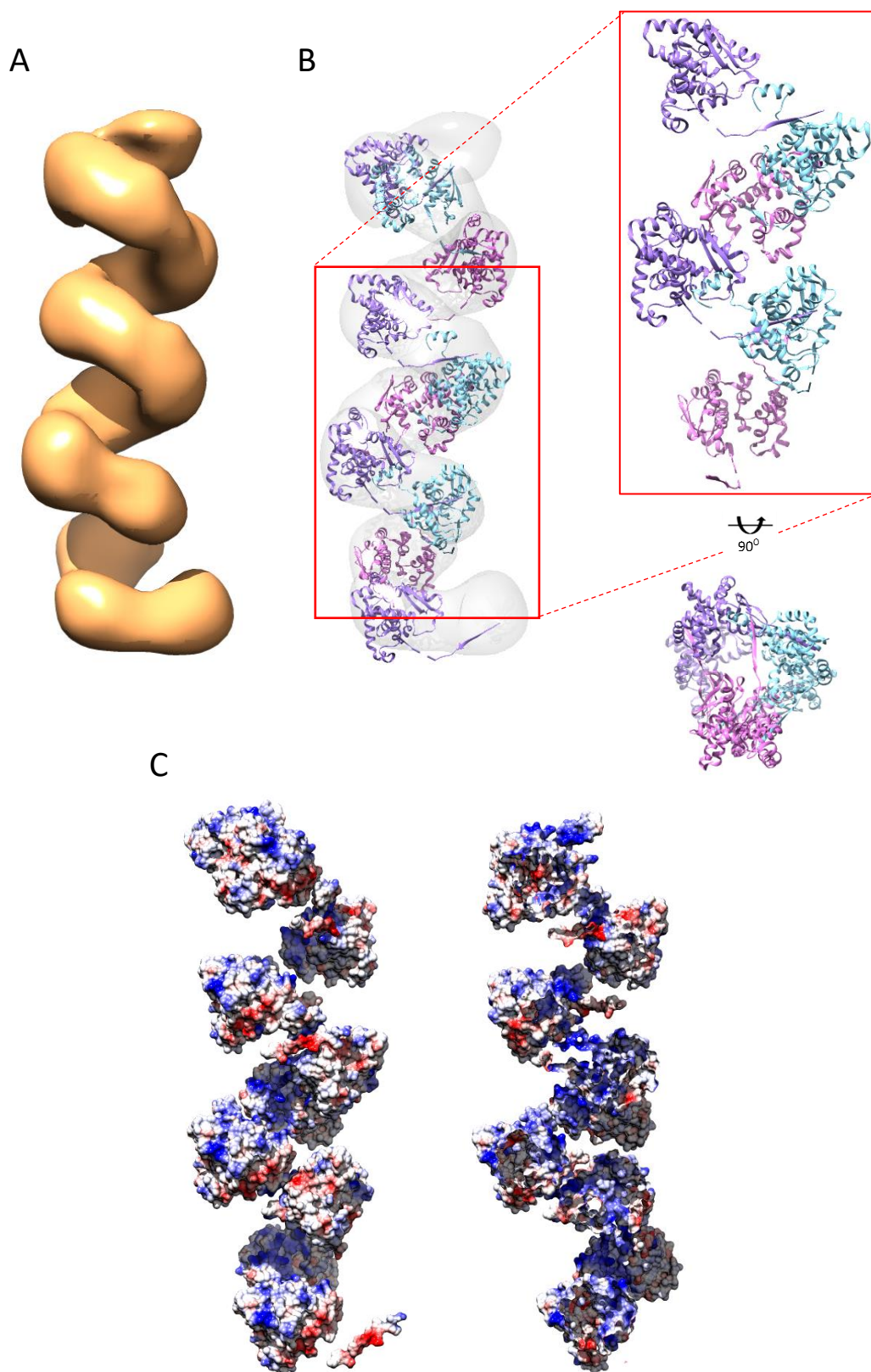


**Figure 4.18:** A 3D model of helical BUNV RNPs. **(A)** Analysis of cryo-EM data led to the generation of a 3D model with clear helical conformation. **(B)** NP crystal structures could be docked into the density in (A). The inset shows the regularity of subunits in a straight section of the helix. **(C)** Displaying the coulombic surface potential onto the docked crystal structures reveals a near-continuous area of positive charge (blue) running down the centre of the helix. Right = a clipped version of the left image.

## 4.6 Discussion

### 4.6.1 Strategies for EM analysis of highly flexible filaments

Producing a 3D model of an orthobunyavirus RNP the application of cryo-ET and STA was instrumental in confirming its helical organisation. For this, it was necessary to confirm the RNPs are indeed helical, which was accomplished via STA. Using this average as a reference, a range of helical parameters were tested, which allowed the generation of a helical average with individual NP monomers, in which NP crystal structures could be fitted. In this study the handedness of the helix was not empirically determined, and the handedness used was chosen from a previous helical RNP structure, derived from X-ray crystallography (Reguera et al., 2013). Using the same grid to collect movies for SPA and tilt series for tomography also provided a direct comparison which highlighted how the use of a Volta phase plate was important for this particular study.

Precedents for using an ensemble of different EM methods already exists, relying on a combination of cryo-ET with single particle cryo-EM. In a seminal paper from the Briggs group, the Gag protein shell of an immature retrovirus was reconstructed at a resolution of 8 Å (Bharat et al., 2012). Cryo-ET and STA was used to determine the helical parameters of individual, tubular virus-like particles (VLPs) and these parameters were then applied for helical reconstruction of the same tube using 2D cryo-EM data collected on film. This same methodology was also used to reconstruct the Gag shell of immature HIV-1 to 9 Å (Bharat et al., 2014). The approach of combining cryo-ET with 2D data allowed this group to overcome the problems posed by reconstructing helical complexes which had varying widths and were sometimes distorted, and allowed them to derive a structure of an average tube.

In this project the obstacle to a reconstruction was not that the helical complex had varying widths, but that it was extremely flexible. However, adopting a strategy

similar to that described above proved effective for reconstruction of an orthobunyavirus RNP. It is important to note that the 3D models presented here are an average model of the ideal helical stretches within the filament and that they do not capture the enormous flexibility and heterogeneity within the filaments, which were the main obstacles for data processing.

The work presented in chapter 3 confirmed that the RNP filaments were too wide to be a linear arrangement of monomers, and cryo-ET confirmed that this non-linear arrangement was helical. The low-resolution helical shape generated by STA provided a starting point for determining helical parameters which were improved by testing a series of different parameters around these. The parameters which were settled on for the final model were determined by using ideal helices to probe which values for twist and helical rise most closely fit the STA model. These parameters were then used to refine a large amount of high contrast negative stain data. Prominent artefacts were present in the first attempt at helical reconstruction which lessened as the helical parameters improved and were another factor when considering which helical parameters to apply to the final model.

Although a resolution could not be reached which allowed the unambiguous placement of crystal structures and the production of a pseudo-atomic model, the resolution achieved did permit the placement of NP structures in their approximate locations, and was enough to answer questions of the gross morphology of orthobunyavirus RNPs. The strategy of using cryo-ET and an STA model to refine large amounts of negative stain data proved to be effective at providing structural information on the nature of BUNV RNPs when single particle cryo-EM was unable to do so. The methods used here could potentially be an effective approach for determining the overall architecture of highly flexible filaments, applicable to a variety of other biological systems.

#### 4.6.2 Longitudinal NP interactions to stabilise the RNP helix

A key question in the formation of orthobunyavirus RNPs is if any interactions occur longitudinally between mirror image NP monomers to stabilise the helix. In the model produced here the distance between such monomers appears to be too large for protein-protein contacts and no obvious interactions can be determined. However, lack of clear longitudinal density between monomers may be due to the insufficiently high-resolution that was obtained. It is also possible that the gap between such monomers is elongated by the computational efforts to mitigate the missing wedge problem, and the longitudinal gap observed here has been exaggerated.

In the model presented in figure 4.13 the NP structures which have been fit to the EM model have been isolated from within the crystal structure of tetrameric NP. Thus, their C- and N-terminal oligomerisation arms are orientated in a particular angle which causes them to point directly into the core of their neighbour. It is unlikely that this would be sterically possible, and it is at odds with the binding sites of the C- and N-terminal arms identified in the tetrameric NP crystal structure (figure 4.19A).

An alternative way of modelling the arrangement of NP monomers is to isolate the globular core of a single monomer with the neighbouring oligomerisation arms bound to it, discarding the density of its own oligomerisation arms (figure 4.19B). In the resulting NP structure the oligomerisation arms are located in their likely binding sites on neighbouring monomers as determined by the tetrameric crystal structure. When this alternate NP structure is fit to the helical RNP model the resulting gap between a monomer's core and its arms could be accounted for by the amino acids missing in the crystal structure (figure 4.19D). These missing residues are likely to constitute a very dynamic linker region, hence their absence in the crystal structure, and the high flexibility of this linker could facilitate NP oligomerisation in the context of the RNP helix.

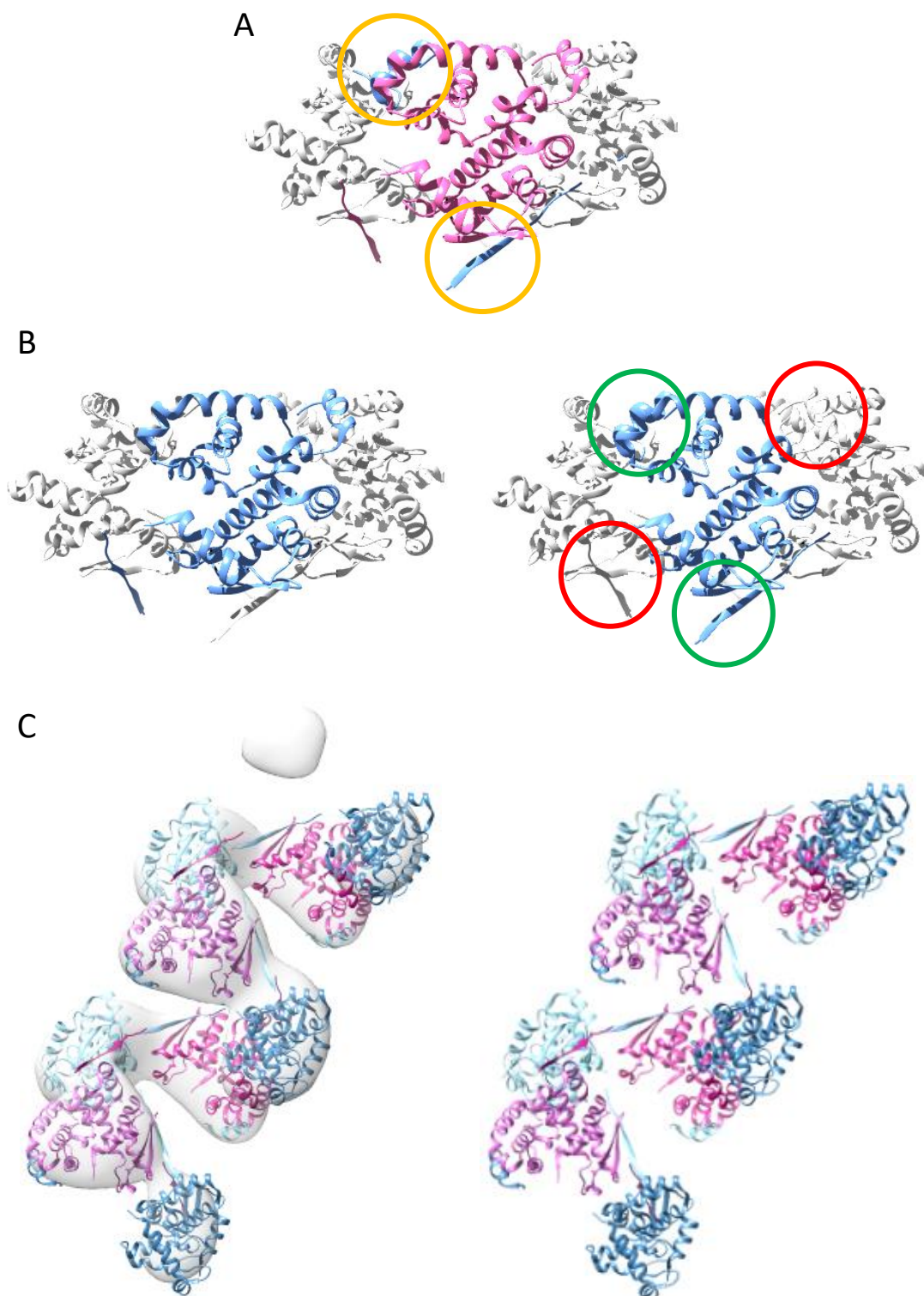


**Figure 4.19:** Longitudinal NP interactions in the BUNV RNP. **(A)** Binding sites of NP oligomerisation domains, as identified by crystallography are highlighted in orange. **(B)** The two different structures of NP fit to the EM density are compared. Left = structure in figure 4.13. Right = updated structure, compared to the left structure red indicates removed atoms and green indicates added atoms **(C)** RNP model with NP crystal structures fit which emphasise the position of N- and C-terminal oligomerisation arms.

In this model of the BUNV RNP which aims to more accurately place the oligomerisation domains of individual monomers, the longitudinal gap between rungs of the helix is unaffected (figure 4.19C) and so the question of what, if any longitudinal interactions exist within the RNP remains unanswered. It is likely that this question cannot be answered with the EM data presented here due to its resolution and a high-resolution, cryo-EM derived structure would be required, like that determined for HTNV (Arragain et al., 2019).

#### **4.6.3 RNA binding in the context of a helical RNP**

Another aspect of the orthobunyavirus RNP for which there is a lack of information in this model is the nature of RNA binding and encapsidation by NP. The resolution of the model presented here is too low to visualise RNA density within the RNA binding groove, as has been previously identified by crystallography (Ariza et al., 2013; Li, B. et al., 2013). However, the RNPs analysed here have been purified from virus samples and 260/280 ratios indicated the presence of RNA. Even though RNA density cannot be observed in the model it can be assumed that it is present and that NP accommodates RNA while adopting a helix. The RNA bound tetrameric crystal structure can be overlaid on the top down view of the filament which supports the theory that RNA can be accommodated in the helix (figure 4.13C). However, all available crystal structures of RNA bound orthobunyavirus NP only exhibit one or two unbound nucleotides between adjacent monomers. It is unlikely that the observed helical rise (figure 4.13A) can be bridged by only one or two nucleotides which raises the hypothesis that longer 'naked' stretches of RNA can be found between monomers. Indeed, this must be the case for the sections of filament which bend. The possibility of long, unbound stretches of RNA being present within the context of an RNP also raises the possibility of RNA structures being accommodated which may have a functional role, as has been observed and characterised recently for influenza (Dadonaite et al., 2019). These structures within the influenza genome facilitate both

intra- and inter-segment interactions which the authors propose are a mechanism of co-segregation during reassortment, and a similar mechanism existing within orthobunyaviruses is an exciting and as yet untested possibility.

#### **4.6.4 Future directions for cryo-EM analysis of orthobunyavirus RNPs**

If manual picking had continued then an estimated ~80000 particles could have been picked but this would have been an extremely arduous task. Collecting high-resolution data would require a better dataset and the ability to use autopicking. Since negative stain confirmed the very high purity of the RNPs, collecting better data would probably require more optimisation of grid making, with a focus on removing the electron-dense contaminants which were encountered and obtaining the straightest RNP filaments possible. Another aid to acquiring such high-resolution data would also be the use of a phase plate. Despite the recent discussion in the cryo-EM community about the efficacy of using the Volta phase plate, in this instance the increase in contrast would aid the autopicking, which is ultimately necessary to pick enough particles for high-resolution structure determination. Indeed, here it is very clear that when the phase plate was inserted for tomography data collection the RNPs were much easier to detect within the ice. The following section describes the processing which followed the collection of data with a phase plate inserted.

#### **4.6.5 Insights from phase plate data acquisition**

A final set of cryo-EM movies was collected to facilitate a single particle reconstruction of an orthobunyavirus RNP, and the initial processing of this data is described in section 4.5.3. As was hypothesised, the inclusion of the Volta phase plate generated enough contrast in the micrographs for Relion to quickly and reliably pick particles.

It is immediately striking that 2D classification of the particles picked from this cryo-EM data set produced classes with a strong resemblance to those produced

throughout the project. The step-wise, alternating pattern of monomers which is indicative of a helix is visible and the filaments are clearly the width of two NP monomers (figure 4.16). Similar validation of earlier results comes from the observation of a clear helical conformation when a simple cylinder was used as the reference for classification, precluding any bias which may be introduced by the use of the STA-derived model as a reference (figure 4.17).

The 3D classes produced from a STA-based reference exhibited more distinct features and a clearer helical appearance so were used for the workflow of classifications and refinements which resulted in the final model presented here (figure 4.18A). From this model the RNP appears not to have four monomers per turn. When a particularly straight section of the model is viewed from above the individual NP monomers resemble a trimer, suggesting a helix with three monomers per turn (4.18B, right). When the full model is viewed from the side the arrangement of NP appears less regular and suggests that the number of subunits per turn of the helix is not a whole number, but is between three and four (figure 4.18B, left). Although hantavirus RNPs differ from those of orthobunyaviruses (section 1.12.2) they are, to date, the only other source of structural information on RNPs within the *Bunyvirales* order and it is of interest that their RNPs form a helix with 3.6 subunits per turn (Arragain et al., 2019).

With this newer data set and the models produced from it, it is again possible to dock crystal structures of BUNV NP into the density corresponding to single monomers, and to do so with greater accuracy than the negative stain-derived model in figure 4.13, as determined by the correlation values output by UCSF Chimera. In the resulting pseudo-atomic model the oligomerisation arms of each monomer interact with their neighbouring monomer in a manner which would be much less susceptible to the steric clashes described in section 4.6.2, in which the arms protrude directly into the core of neighbouring monomers. In the newly proposed

model, the oligomerisation arms contact the surface of their neighbours in a manner which more closely resembles the binding observed in the tetrameric crystal structure. It is important to note that the position of the oligomerisation arms in the pseudo-atomic model presented here are fixed in the position determined in the crystal structure, and that this is unlikely to accurately represent their binding in the context of a helix. However, in the newer model the arms are better positioned to contact the binding sites illuminated in the crystal structure and it is likely that this could be accommodated by the high degree of flexibility of these arms.

From the fitted NP crystal structures it is possible to display the surfaces with the electrostatic potential illustrated by colour, indicating areas of positive or negative charge. The RNA binding groove of individual NP monomers is positively charged and in the model displayed in figure 4.18C these grooves are aligned relative to each other in such a way as to form a near-continuous channel that runs down the interior of the RNP helix and this particularly clear in a clipped view of the RNP (figure 4.18C, right). This illustrates that the proposed model of an orthobunyavirus RNP is compatible with its function of encapsidating the viral genomic RNA and could enwrap the vRNA in almost its entirety.

A very recent cryo-EM study into IAV RNPs found an enormous degree of heterogeneity within RNPs, with NP monomers adopting a wide range of conformations even while maintaining the overall double helix structure. The authors of this paper sorted their available particles into small classes of one to four thousand particles and took each class forwards individually for 3D reconstruction. They also utilised an ad hoc protocol for 3D refinement that involved iterations both with and without searches for helical symmetry. Although the nature of the heterogeneity in IAV RNPs is different to that encountered here in BUNV RNPs, and is not a product of extreme flexibility, these techniques may prove useful in the processing of BUNV cryo-EM data and are a starting point for developing similar workflows for the

processing of data from extremely heterogeneous filaments (Coloma et al., 2020). Future work to build on the research described in this thesis should begin with further processing of the final cryo-EM data set, utilising and continuing to improve upon the methods already applied and described in this chapter, and those applied to other viral RNPs such as IAV. With further refinements and an improved 3D model of the BUNV RNP, work can then move onto identifying the residues involved in the formation and maintenance of the helix and those involved in the conformational changes which must be required for successful transcription and replication of viral RNA.

## Chapter 5

### Concluding remarks

This thesis presents what is likely to be the most comprehensive characterisation of near-native orthobunyavirus RNPs to date (figure 5.1). This was possible because existing protocols for the purification of orthobunyaviruses and their RNPs were refined and subsequent protocols were developed to optimise how these RNPs were taken forwards for EM analysis. Despite the quality of negative stain data acquired and the collection of a cryo-EM dataset, a high resolution 3D structure of the orthobunyavirus RNP remains elusive. Such a structure would elucidate the specific homotypic interactions of NP monomers and interactions with RNA which facilitate RNP formation while still permitting essential access of replication machinery to the RNA. Structural information of this detail would in turn aid structure-based drug design, targeting a group of viruses which poses an increasing threat to human and livestock health and for which there is currently a paucity of available therapies. It is hoped that this work has laid the foundation for such high-resolution data to be collected and processed in the future.

A final cryo-EM data set collected at the end of this PhD project began the work towards producing a higher resolution model of the orthobunyavirus RNP, and demonstrated how a phase plate can aid in the cryo-EM analysis of difficult samples. The 3D model produced from the processing of this data appears better defined than the negative stain-derived model and importantly, is clearly helical even when no helices (such as the STA-derived model) are used as a reference, and when no helical symmetry is applied (figures 4.17 and 4.18). Interestingly, this newer model differs from the negative stain-derived model in the number of subunits per turn. The

negative-stain model had helical symmetry imposed based on the assumption of four subunits per turn, which came from a previous crystallography-derived model of a helical RNP (Reguera et al., 2013) and a hypothesis put forwards to describe the RNP architecture (Ariza et al., 2013; Reguera et al., 2013). Further processing of this data should focus on the application of helical symmetry based on the new observation of a number of subunits per turn between three and four. With the increase in resolution expected to be gained from this, and the subsequent fitting of crystal structures with more accuracy, a higher quality model of the RNP can be produced which can instruct further biochemical studies. Due to the extreme flexibility of these filaments it is likely that this newest cryo-EM data will not generate a model of high enough resolution to build the NP structure and produce a true atomic-resolution model of the RNP, as has been produced for hantaviruses (Arragain et al., 2019). It is also likely that such a model can never be produced from native S, M and L RNPs purified from viruses. Attempts to generate a structure of such resolution could employ reverse genetics to produce smaller synthetic RNPs with a more rigid structure, as was done for IAV (Coloma et al., 2009), or search for a method of cleaving an RNP while maintaining its helical architecture, on the basis that it would be easier to induce a linear filament to lie straight on an EM grid.

In the large number of RNPs which were visualised during the course of this project, no linear, 'beads on a string' type architecture was ever observed, despite previous observations by other groups and despite the likelihood that such an architecture is required at points in the viral replication cycle. Another expected observation which was not made, was of some sort of structure which would indicate the ends of the viral RNA segments. All discrete RNPs which were observed were circularised and maintained a consistent architecture around their entire length. The observed oligomeric rings and filament-type structures observed here may represent important parts of the assembly and disassembly processes.

Much work remains to be done in the field of BUNV RNPs, beginning with a continuation of the work presented here and the determination of a 3D structure of the NP-RNA filament. Future work should aim to characterise the mechanism of polymerase interaction with the filament, the structural mechanisms of RNA replication within the context of the RNP and the dynamics of how RNP filaments are assembled, in order to build a complete picture of the replication of these viruses. The field of segmented RNA virus replication has very recently seen exciting advances such as the solution of a helical hantavirus RNP structure (Arragain et al., 2019), the solution of arenavirus polymerase structures (Peng, R. et al., 2020), the

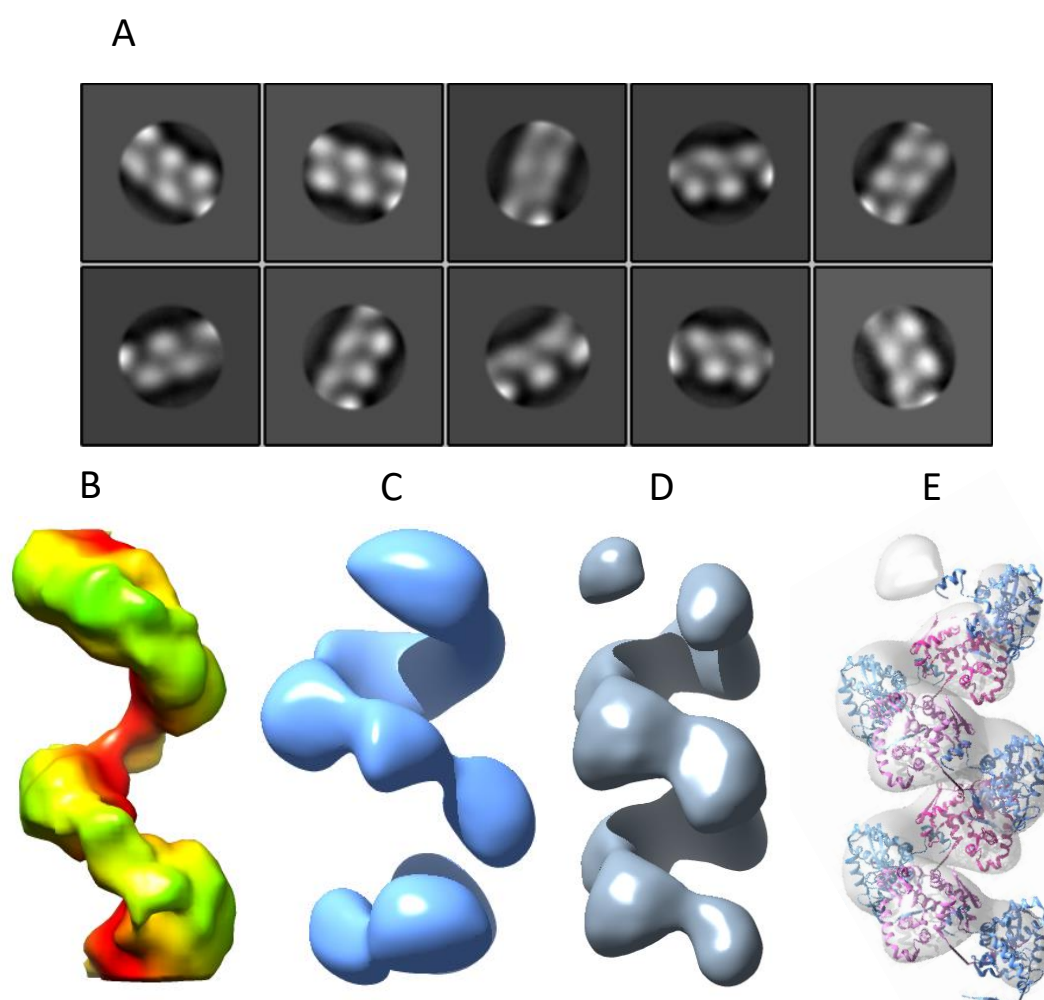


**Figure 5.1:** A summary of the structural information on BUNV RNPs presented in this thesis. **(A)** Top 2D class averages, **(B)** STA derived helical model **(C)** 3D refinement of negative stain data with no symmetry applied **(D)** helical reconstruction of negative stain data and **(E)** docking of NP crystal structures into the helical reconstruction derived map.

improvement in resolution of the IAV RNP model and new insights into heterogeneity of NP within the filament (Coloma et al., 2020) and the finding that IAV RNPs can accommodate RNA secondary structures to aid in packaging (Dadonaite et al., 2019).

It is hoped that the models presented in this thesis of the orthobunyavirus RNP are another important step in the progress of the field towards a complete understanding of segmented negative RNA viruses and their replication mechanisms.

## Chapter 6

### References

Abraham, G. & Pattnaik, A. K. (1983) Early RNA Synthesis in Bunyamwera Virus-Infected Cells. *Journal of General Virology*, 64, pp. 1277–1290.

Abudurexiti, A., Adkins, S., Alioto, D., Alkhovsky, S. V., Avšič-Županc, T., Ballinger, M. J., Bente, D. A., Beer, M., Bergeron, É., Blair, C. D., Briese, T., Buchmeier, M. J., Burt, F. J., Calisher, C. H., Cháng, C., Charrel, R. N., Choi, I. R., Clegg, J. C. S., La Torre, J. C. De, Lamballerie, X. De, Dèng, F., Serio, F. Di, Digiaro, M., Drebot, M. A., Duàn, X., Ebihara, H., Elbeaino, T., Ergünay, K., Fulhorst, C. F., Garrison, A. R., Gão, G. F., Gonzalez, J. P. J., Groschup, M. H., Günther, S., Haenni, A. L., Hall, R. A., Hepojoki, J., Hewson, R., Hú, Z., Hughes, H. R., Jonson, M. G., Junglen, S., Klempa, B., Klingström, J., Kòu, C., Laenen, L., Lambert, A. J., Langevin, S. A., Liu, D., Lukashovich, I. S., Luò, T., Lǔ, C., Maes, P., Souza, W. M. De, Marklewitz, M., Martelli, G. P., Matsuno, K., Mielke-Ehret, N., Minutolo, M., Mirazimi, A., Moming, A., Mühlbach, H. P., Naidu, R., Navarro, B., Nunes, M. R. T., Palacios, G., Papa, A., Pauvolid-Corrêa, A., Pawęska, J. T., Qiáo, J., Radoshitzky, S. R., Resende, R. O., Romanowski, V., Sall, A. A., Salvato, M. S., Sasaya, T., Shěn, S., Shí, X., Shirako, Y., Simmonds, P., Sironi, M., Song, J. W., Spengler, J. R., Stenglein, M. D., Sū, Z., Sūn, S., Táng, S., Turina, M., Wáng, B., Wáng, C., Wáng, H., Wáng, J., Wèi, T., Whitfield, A. E., Zerbini, F. M., Zhāng, J., Zhāng, L., Zhāng, Y., Zhang, Y. Z., Zhāng, Y., Zhou, X., Zhū, L. & Kuhn, J. H. (2019) Taxonomy of the Order Bunyavirales: Update 2019. *Archives of Virology*, 164, pp. 1949–1965.

Agirrezabala, X., Méndez-López, E., Lasso, G., Sánchez-Pina, M. A., Aranda, M. & Valle, M. (2015) The Near-Atomic CryoEM Structure of a Flexible Filamentous Plant Virus Shows Homology of Its Coat Protein with Nucleoproteins of Animal Viruses. *eLife*, 4, p. e11795.

Akashi, H. & Bishop, D. H. L. (1983) Comparison of the Sequences and Coding of La Crosse and Snowshoe Hare Bunyavirus S RNA Species. *Journal of Virology*, 45 (3), pp. 1155–1158.

Albertini, A. A. V., Wernimont, A. K., Muziol, T., Ravelli, R. B. G., Clapier, C. R., Schoehn, G., Weissenhorn, W. & Ruigrok, R. W. H. (2006) Crystal Structure of the Rabies Virus Nucleoprotein-RNA Complex. *Science*, 313 (5785), pp. 360–363.

Albornoz, A., Hoffmann, A. B., Lozach, P.-Y. & Tischler, N. D. (2016) Early Bunyavirus-Host Cell Interactions. *Viruses*, 8 (5), p. 143.

Alfadhli, A., Love, Z., Arvidson, B., Seeds, J., Willey, J. & Barklis, E. (2001) Hantavirus Nucleocapsid Protein Oligomerization. *Journal of Virology*, 75 (4), pp. 2019–2023.

Anderson Jr, G. W. & Smith, J. F. (1987) Immunoelectron Microscopy of Rift Valley Fever Viral Morphogenesis in Primary Rat Hepatocytes. *Virology*, 161, pp. 91–100.

- Area, E., Martín-Benito, J., Gastaminza, P., Torreira, E., Valpuesta, J. M., Carrascosa, J. L. & Ortín, J. (2004) 3D Structure of the Influenza Virus Polymerase Complex: Localization of Subunit Domains. *Proceedings of the National Academy of Sciences of the United States of America*, 101 (1), pp. 308–313.
- Ariza, A., Tanner, S. J., Walter, C. T., Dent, K. C., Shepherd, D. A., Wu, W., Matthews, S. V., Hiscox, J. a., Green, T. J., Luo, M., Elliott, R. M., Fooks, A. R., Ashcroft, A. E., Stonehouse, N. J., Ranson, N. A., Barr, J. N. & Edwards, T. A. (2013) Nucleocapsid Protein Structures from Orthobunyaviruses Reveal Insight into Ribonucleoprotein Architecture and RNA Polymerization. *Nucleic Acids Research*, 41 (11), pp. 5912–5926.
- Arragain, B., Reguera, J., Desfosses, A., Gutsche, I., Schoehn, G. & Malet, H. (2019) High Resolution Cryo-EM Structure of the Helical RNA-Bound Hantaan Virus Nucleocapsid Reveals Its Assembly Mechanisms. *eLife*, 8, p. e43075.
- Arranz, R., Coloma, R., Chichon, F. J., Conesa, J. J., Carrascosa, J. L., Valpuesta, J. M., Ortín, J. & Martín-Benito, J. (2012) The Structure of Native Influenza Virion Ribonucleoproteins. *Science*, 338 (6114), pp. 1634–1637.
- Atkinson, B. & Hewson, R. (2018) Emerging Arboviruses of Clinical Importance in Central Asia. *Journal of General Virology*, 99 (9), pp. 1172–1184.
- Baker, L. A. & Rubinstein, J. L. (2010) Radiation Damage in Electron Cryomicroscopy. *Methods in Enzymology*, 481, pp. 371–388.
- Baklouti, A., Goulet, A., Lichière, J., Canard, B., Charrel, R. N., Ferron, F., Coutard, B. & Papageorgiou, N. (2017) *Toscana Virus* Nucleoprotein Oligomer Organization Observed in Solution. *Acta Crystallographica Section D: Structural Biology*, 73 (8), pp. 650–659.
- Ballinger, M. J., Bruenn, J. A., Hay, J., Czechowski, D. & Taylor, D. J. (2014) Discovery and Evolution of Bunyavirids in Arctic Phantom Midges and Ancient Bunyavirid-Like Sequences in Insect Genomes. *Journal of Virology*, 88 (16), pp. 8783–8794.
- Baltimore, D. (1971) Expression of Animal Virus Genomes. *Bacteriological Reviews*, 35 (3), pp. 235–241.
- Barr, J. N. (2007) Bunyavirus mRNA Synthesis Is Coupled to Translation to Prevent Premature Transcription Termination. *RNA*, 13, pp. 731–736.
- Barr, J. N., Rodgers, J. W. & Wertz, G. W. (2005) The Bunyamwera Virus mRNA Transcription Signal Resides within Both the 3' and the 5' Terminal Regions and Allows Ambisense Transcription from a Model RNA Segment. *Journal of Virology*, 79 (19), pp. 12602–12607.
- Barr, J. N., Rodgers, J. W. & Wertz, G. W. (2006) Identification of the Bunyamwera Bunyavirus Transcription Termination Signal. *Journal of General Virology*, 87, pp. 189–198.
- Bartesaghi, A., Aguerrebere, C., Falconieri, V., Banerjee, S., Earl, L. A., Zhu, X., Grigorieff, N., Milne, J. L. S., Sapiro, G., Wu, X. & Subramaniam, S. (2018) Atomic Resolution Cryo-EM Structure of  $\beta$ -Galactosidase. *Structure*, 26, pp. 848–856.
- Battisti, A. J., Chu, Y.-K., Chipman, P. R., Kaufmann, B., Jonsson, C. B. & Rossmann, M. G. (2011) Structural Studies of Hantaan Virus. *Journal of Virology*, 85 (2), pp. 835–841.

Baylis, M. (2017) Potential Impact of Climate Change on Emerging Vector-Borne and Other Infections in the UK. *Environmental Health*, 16 (Suppl 1), p. 112.

Bharat, T. A. M., Castillo Menendez, L. R., Hagen, W. J. H., Lux, V., Igonet, S., Schorb, M., Schur, F. K. M., Kraüsslich, H.-G. & Briggs, J. A. G. (2014) Cryo-Electron Microscopy of Tubular Arrays of HIV-1 Gag Resolves Structures Essential for Immature Virus Assembly. *Proceedings of the National Academy of Sciences of the United States of America*, 111 (22), pp. 8233–8238.

Bharat, T. A. M., Davey, N. E., Ulbrich, P., Riches, J. D., Marco, A. De, Rumlova, M., Sachse, C., Ruml, T. & Briggs, J. A. G. (2012) Structure of the Immature Retroviral Capsid at 8 Å Resolution by Cryo-Electron Microscopy. *Nature*, 487 (7407), pp. 385–389.

Bishop, D. H. L., Gay, M. E. & Matsuoko, Y. (1983) Nonviral Heterogeneous Sequences Are Present at the 5' Ends of One Species of Snowshoe Hare Bunyavirus S Complementary RNA. *Nucleic Acids Research*, 11 (18), pp. 6409–6418.

Blakqori, G., Knippenberg, I. Van & Elliott, R. M. (2009) Bunyamwera Orthobunyavirus S-Segment Untranslated Regions Mediate Poly(A) Tail-Independent Translation. *Journal of Virology*, 83 (8), pp. 3637–3646.

Blakqori, G., Lowen, A. C. & Elliott, R. M. (2012) The Small Genome Segment of Bunyamwera Orthobunyavirus Harbours a Single Transcription-Termination Signal. *Journal of General Virology*, 93, pp. 1449–1455.

Blijleven, J. S., Boonstra, S., Onck, P. R., Giessen, E. Van Der & Oijen, A. M. Van (2016) Mechanisms of Influenza Viral Membrane Fusion. *Seminars in Cell and Developmental Biology*, 60, pp. 78–88.

Borucki, M. K., Kempf, B. J., Blitvich, B. J., Blair, C. D. & Beaty, B. J. (2002) La Crosse Virus: Replication in Vertebrate and Invertebrate Hosts. *Microbes and Infection*, 4, pp. 341–350.

Bowden, T. A., Bitto, D., McLees, A., Yeromonahos, C., Elliott, R. M. & Huisken, J. T. (2013) Orthobunyavirus Ultrastructure and the Curious Tripodal Glycoprotein Spike. *PLoS Pathogens*, 9 (5), p. e1003374.

Bowen, M. D., Trappier, S. G., Sanchez, A. J., Meyer, R. F., Goldsmith, C. S., Zaki, S. R., Dunster, L. M., Peters, C. J., Ksiazek, T. G. & Nichol, S. T. (2001) A Reassortant Bunyavirus Isolated from Acute Hemorrhagic Fever Cases in Kenya and Somalia. vol. 291.

Bridgen, A. & Elliott, R. M. (1996) Rescue of a Segmented Negative-Strand RNA Virus Entirely from Cloned Complementary DNAs. *Proceedings of the National Academy of Sciences of the United States of America*, 93, pp. 15400–15404.

Briese, T., Bird, B., Kapoor, V., Nichol, S. T. & Lipkin, W. I. (2006) Batai and Ngari Viruses: M Segment Reassortment and Association with Severe Febrile Disease Outbreaks in East Africa. *Journal of Virology*, 80 (11), pp. 5627–5630.

Brunotte, L., Kerber, R., Shang, W., Hauer, F., Hass, M., Gabriel, M., Lelke, M., Busch, C., Stark, H., Svergun, D. I., Betzel, C., Perbandt, M. & Günther, S. (2011) Structure of the Lassa Virus Nucleoprotein Revealed by X-Ray Crystallography, Small-Angle X-Ray Scattering, and Electron Microscopy. *Journal of Biological Chemistry*, 286 (44), pp. 38748–38756.

- Campbell, M. G., Kearney, B. M., Cheng, A., Potter, C. S., Johnson, J. E., Carragher, B. & Veessler, D. (2014) Near-Atomic Resolution Reconstructions Using a Mid-Range Electron Microscope Operated at 200 kV. *Journal of Structural Biology*, 188, pp. 183–187.
- Carter, S. D., Surtees, R., Walter, C. T., Ariza, A., Bergeron, É., Nichol, S. T., Hiscox, J. A., Edwards, T. A. & Barr, J. N. (2012) Structure, Function, and Evolution of the Crimean-Congo Hemorrhagic Fever Virus Nucleocapsid Protein. *Journal of Virology*, 86 (20), pp. 10914–10923.
- Cassidy, L. F. & Patterson, J. L. (1989) Mechanism of La Crosse Virus Inhibition by Ribavirin. *Antimicrobial Agents and Chemotherapy*, 33 (11), pp. 2009–2011.
- Charlton, F. W., Hover, S., Fuller, J., Hewson, R., Fontana, J., Barr, J. N. & Mankouri, J. (2019) Cellular Cholesterol Abundance Regulates Potassium Accumulation within Endosomes and Is an Important Determinant in Bunyavirus Entry. *Journal of Biological Chemistry*, 294, pp. 7335–7347.
- Cheng, Y., Grigorieff, N., Penczek, P. A. & Walz, T. (2015) A Primer to Single-Particle Cryo-Electron Microscopy. *Cell*, 161 (3), pp. 438–449.
- Cimica, V., Dalrymple, N. A., Roth, E., Nasonov, A. & Mackow, E. R. (2014) An Innate Immunity-Regulating Virulence Determinant Is Uniquely Encoded within the Andes Virus Nucleocapsid Protein. *mBio*, 5 (1), pp. e01088-13.
- Coloma, R., Arranz, R., la Rosa-trevín, J. M. De, Sorzano, C. O. S., Munier, S., Carlero, D., Naffakh, N., Ortín, J. & Martín-Benito, J. (2020) Structural Insights into Influenza A Virus Ribonucleoproteins Reveal a Processive Helical Track as Transcription Mechanism. *Nature Microbiology*.
- Coloma, R., Valpuesta, J. M., Arranz, R., Carrascosa, J. L., Ortín, J. & Martín-Benito, J. (2009) The Structure of a Biologically Active Influenza Virus Ribonucleoprotein Complex. *PLoS Pathogens*, 5 (6), p. e1000491.
- Dadonaite, B., Gilbertson, B., Knight, M. L., Trifkovic, S., Rockman, S., Laederach, A., Brown, L. E., Fodor, E. & Bauer, D. L. V. (2019) The Structure of the Influenza A Virus Genome. *Nature Microbiology*, 4 (11), pp. 1781–1789.
- Danev, R. & Baumeister, W. (2016) Cryo-EM Single Particle Analysis with the Volta Phase Plate. *eLife*, 5, p. e13046.
- Devignot, S., Bergeron, E., Nichol, S., Mirazimi, A. & Weber, F. (2015) A Virus-Like Particle System Identifies the Endonuclease Domain of Crimean-Congo Hemorrhagic Fever Virus. *Journal of Virology*, 89 (11), pp. 5957–5967.
- Deyde, V. M., Rizvanov, A. A., Chase, J., Otteson, E. W. & Jeor, S. C. St. (2005) Interactions and Trafficking of Andes and Sin Nombre Hantavirus Glycoproteins G1 and G2. *Virology*, 331, pp. 307–315.
- Dias, A., Bouvier, D., Crépin, T., McCarthy, A. A., Hart, D. J., Baudin, F., Cusack, S. & Ruigrok, R. W. H. (2009) The Cap-Snatching Endonuclease of Influenza Virus Polymerase Resides in the PA Subunit. *Nature*, 458, pp. 914–918.
- DiMaio, F., Chen, C.-C., Yu, X., Frenz, B., Hsu, Y.-H., Lin, N.-S. & Egelman, E. H. (2015) The Molecular Basis for Flexibility in the Flexible Filamentous Plant Viruses. *Nature Structural & Molecular Biology*, 22 (8), pp. 642–644.

- Donchet, A., Oliva, J., Labaronne, A., Tengo, L., Miloudi, M., Gerard, F. C. A., Mas, C., Schoehn, G., Ruigrok, R. W. H., Ducatez, M. & Crépin, T. (2019) The Structure of the Nucleoprotein of Influenza D Shows That All *Orthomyxoviridae* Nucleoproteins Have a Similar NP<sub>CORE</sub>, with or without a NP<sub>TAIL</sub> for Nuclear Transport. *Scientific Reports*, 9 (1), p. 600.
- Dong, H., Li, P., Böttcher, B., Elliott, R. M. & Dong, C. (2013) Crystal Structure of Schmallenberg Orthobunyavirus Nucleoprotein–RNA Complex Reveals a Novel RNA Sequestration Mechanism. *RNA*, 19 (8), pp. 1129–1136.
- Dong, H., Li, P., Elliott, R. M. & Dong, C. (2013) Structure of Schmallenberg Orthobunyavirus Nucleoprotein Suggests a Novel Mechanism of Genome Encapsidation. *Journal of Virology*, 87 (10), pp. 5593–5601.
- Drebot, M. (2015) Emerging Mosquito-Borne Bunyaviruses in Canada. *Canada Communicable Disease Report*, 41 (6), pp. 117–123.
- Dutuze, M. F., Nzayirambaho, M., Mores, C. N. & Christofferson, R. C. (2018) A Review of Bunyamwera, Batai, and Ngari Viruses: Understudied *Orthobunyaviruses* With Potential One Health Implications. *Frontiers in Veterinary Science*, 5 (69).
- Edwards, J. F., Livingston, C. W., Chung, S. I. & Collisson, E. C. (1989) Ovine Arthrogryposis and Central Nervous System Malformations Associated with *in Utero* Cache Valley Virus Infection: Spontaneous Disease. *Veterinary Pathology*, 26, pp. 33–39.
- Egelman, E. H. (2007) The Iterative Helical Real Space Reconstruction Method: Surmounting the Problems Posed by Real Polymers. *Journal of Structural Biology*, 157, pp. 83–94.
- Eifan, S. A. & Elliott, R. M. (2009) Mutational Analysis of the Bunyamwera Orthobunyavirus Nucleocapsid Protein Gene. *Journal of Virology*, 83 (21), pp. 11307–11317.
- Elliott, R. M. (1989a) Nucleotide Sequence Analysis of the Large (L) Genomic RNA Segment of Bunyamwera Virus, the Prototype of the Family Bunyaviridae. *Virology*, 173, pp. 426–436.
- Elliott, R. M. (1989b) Nucleotide Sequence Analysis of the Small (S) RNA Segment of Bunyamwera Virus, the Prototype of the Family Bunyaviridae. *Journal of General Virology*, 170, pp. 1281–1285.
- Elliott, R. M. (2014) Orthobunyaviruses: Recent Genetic and Structural Insights. *Nature Reviews Microbiology*, 12 (10), pp. 673–685.
- Endalew, A. D., Faburay, B., Wilson, W. C. & Richt, J. A. (2019) Schmallenberg Disease—A Newly Emerged Culicoides-Borne Viral Disease of Ruminants. *Viruses*, 11 (11), p. 1065.
- European Food Safety Authority (2013) “*Schmallenberg*” Virus: Analysis of the Epidemiological Data (May 2013) [Online]. vol. EN-429. Available from: <<http://www.efsa.europa.eu/en/supporting/pub/429e.htm>>.
- Evans, A. B., Winkler, C. W. & Peterson, K. E. (2019) Differences in Neuropathogenesis of Encephalitic California Serogroup Viruses. *Emerging Infectious Diseases*, 25 (4), pp. 728–738.

- Fan, H., Walker, A. P., Carrique, L., Keown, J. R., Serna Martin, I., Karia, D., Sharps, J., Hengrung, N., Pardon, E., Steyaert, J., Grimes, J. M. & Fodor, E. (2019) Structures of Influenza A Virus RNA Polymerase Offer Insight into Viral Genome Replication. *Nature*, 573 (7773), pp. 287–290.
- Fazakerley, J. K., Gonzalez-Scarano, F., Strickler, J., Dietzschold, B., Karush, F. & Nathanson, N. (1988) Organization of the Middle RNA Segment of Snowshoe Hare Bunyavirus. *Virology*, 167 (2), pp. 422–432.
- Fernández-García, Y., Reguera, J., Busch, C., Witte, G., Sánchez-Ramos, O., Betzel, C., Cusack, S., Günther, S. & Reindl, S. (2016) Atomic Structure and Biochemical Characterization of an RNA Endonuclease in the N Terminus of Andes Virus L Protein. *PLoS Pathogens*, 12 (6), p. e1005635.
- Ferron, F., Li, Z., Danek, E. I., Luo, D., Wong, Y., Coutard, B., Lantéz, V., Charrel, R., Canard, B., Walz, T. & Lescar, J. (2011) The Hexamer Structure of the Rift Valley Fever Virus Nucleoprotein Suggests a Mechanism for Its Assembly into Ribonucleoprotein Complexes. *PLoS Pathogens*, 7 (5), p. e1002030.
- Fodor, E. (2013) The RNA Polymerase of Influenza A Virus: Mechanisms of Viral Transcription and Replication. *Acta Virologica*, 57, pp. 113–122.
- Fontana, J., López-Montero, N., Elliott, R. M., Fernández, J. J. & Risco, C. (2008) The Unique Architecture of Bunyamwera Virus Factories around the Golgi Complex. *Cellular Microbiology*, 10 (10), pp. 2012–2028.
- Freiberg, A. N., Sherman, M. B., Morais, M. C., Holbrook, M. R. & Watowich, S. J. (2008) Three-Dimensional Organization of Rift Valley Fever Virus Revealed by Cryoelectron Tomography. *Journal of Virology*, 82 (21), pp. 10341–10348.
- Ganaie, S. S., Haque, A., Cheng, E., Bonny, T. S., Salim, N. N. & Mir, M. A. (2014) Ribosomal Protein S19-Binding Domain Provides Insights into Hantavirus Nucleocapsid Protein-Mediated Translation Initiation Mechanism. *Biochemical Journal*, 464, pp. 109–121.
- Ge, P., Tsao, J., Schein, S., Green, T. J., Luo, M. & Zhou, Z. H. (2010) Cryo-EM Model of the Bullet-Shaped Vesicular Stomatitis Virus. *Science*, 327 (5966), pp. 689–693.
- Gerlach, P., Malet, H., Cusack, S. & Reguera, J. (2015) Structural Insights into Bunyavirus Replication and Its Regulation by the vRNA Promoter. *Cell*, 161 (6), pp. 1267–1279.
- Gerrard, S. R., Li, L., Barrett, A. D. & Nichol, S. T. (2004) Ngari Virus Is a Bunyamwera Virus Reassortant That Can Be Associated with Large Outbreaks of Hemorrhagic Fever in Africa. *Journal of Virology*, 78 (16), pp. 8922–8926.
- Goller, K. V., Höper, D., Schirrmeier, H., Mettenleiter, T. C. & Beer, M. (2012) Schmallenberg Virus as Possible Ancestor of Shamonda Virus. *Emerging Infectious Diseases*, 18 (10), pp. 1644–1646.
- Goodbourn, S., Didcock, L. & Randall, R. E. (2000) Interferons: Cell Signalling, Immune Modulation, Antiviral Responses and Virus Countermeasures. *Journal of General Virology*, 81, pp. 2341–2364.
- Gould, E. A. & Higgs, S. (2009) Impact of Climate Change and Other Factors on Emerging Arbovirus Diseases. *Transactions of the Royal Society of Tropical Medicine and Hygiene*, 103 (2), pp. 109–121.

Gowen, B. B., Wong, M.-H., Jung, K.-H., Sanders, A. B., Mendenhall, M., Bailey, K. W., Furuta, Y. & Sidwell, R. W. (2007) *In Vitro* and *In Vivo* Activities of T-705 against Arenavirus and Bunyavirus Infections. *Antimicrobial Agents and Chemotherapy*, 51 (9), pp. 3168–3176.

Grady, L. J., Sanders, M. L. & Campbell, W. P. (1987) The Sequence of the M RNA of an Isolate of La Crosse Virus. *Journal of General Virology*, 68, pp. 3057–3071.

Green, T. J., Zhang, X., Wertz, G. W. & Luo, M. (2006) Structure of the Vesicular Stomatitis Virus Nucleoprotein-RNA Complex. *Science*, 313, pp. 357–360.

Grimstad, P. R., Barrett, C. L., Humphrey, R. L. & Sinsko, M. J. (1984) Serologic Evidence for Widespread Infection with La Crosse and St. Louis Encephalitis Viruses in the Indiana Human Population. *American Journal of Epidemiology*, 119 (6), pp. 913–930.

Guardado-Calvo, P., Atkovska, K., Jeffers, S. A., Grau, N., Backovic, M., Pérez-Vargas, J., Boer, S. M. De, Tortorici, M. A., Pehau-Arnaudet, G., Lepault, J., England, P., Rottier, P. J., Bosch, B. J., Hub, J. S. & Rey, F. A. (2017) A Glycerophospholipid-Specific Pocket in the RVFV Class II Fusion Protein Drives Target Membrane Insertion. *Science*, 358 (6363), pp. 663–667.

Guardado-Calvo, P., Bignon, E. A., Stettner, E., Jeffers, S. A., Pérez-Vargas, J., Pehau-Arnaudet, G., Tortorici, M. A., Jestin, J.-L., England, P., Tischler, N. D. & Rey, F. A. (2016) Mechanistic Insight into Bunyavirus-Induced Membrane Fusion from Structure-Function Analyses of the Hantavirus Envelope Glycoprotein Gc. *PLoS Pathogens*, 12 (10), p. e1005813.

Guo, Y., Wang, W., Ji, W., Deng, M., Sun, Y., Zhou, H., Yang, C., Deng, F., Wang, H., Hu, Z., Lou, Z. & Rao, Z. (2012) Crimean–Congo Hemorrhagic Fever Virus Nucleoprotein Reveals Endonuclease Activity in Bunyaviruses. *Proceedings of the National Academy of Sciences of the United States of America*, 109 (13), pp. 5046–5051.

Guo, Y., Wang, W., Sun, Y., Ma, C., Wang, X., Wang, X., Liu, P., Shen, S., Li, B., Lin, J., Deng, F., Wang, H. & Lou, Z. (2016) Crystal Structure of the Core Region of Hantavirus Nucleocapsid Protein Reveals the Mechanism for Ribonucleoprotein Complex Formation. *Journal of Virology*, 90 (2), pp. 1048–1061.

Gutsche, I., Desfosses, A., Effantin, G., Ling, W. L., Haupt, M., Ruigrok, R. W. H., Sachse, C. & Schoehn, G. (2015) Near-Atomic Cryo-EM Structure of the Helical Measles Virus Nucleocapsid. *Science*, 348 (6235), pp. 704–707.

Halldorsson, S., Behrens, A.-J., Harlos, K., Huiskonen, J. T., Elliott, R. M., Crispin, M., Brennan, B. & Bowden, T. A. (2016) Structure of a Phleboviral Envelope Glycoprotein Reveals a Consolidated Model of Membrane Fusion. *Proceedings of the National Academy of Sciences of the United States of America*, 113 (26), pp. 7154–7159.

Halldorsson, S., Li, S., Li, M., Harlos, K., Bowden, T. A. & Huiskonen, J. T. (2018) Shielding and Activation of a Viral Membrane Fusion Protein. *Nature Communications*, 9, p. 349.

Haque, A. & Mir, M. A. (2010) Interaction of Hantavirus Nucleocapsid Protein with Ribosomal Protein S19. *Journal of Virology*, 84 (23), pp. 12450–12453.

- Hastie, K. M., Liu, T., Li, S., King, L. B., Ngo, N., Zandonatti, M. A., Woods, V. L., La Torre, J. C. De & Saphire, E. O. (2011) Crystal Structure of the Lassa Virus Nucleoprotein–RNA Complex Reveals a Gating Mechanism for RNA Binding. *Proceedings of the National Academy of Sciences of the United States of America*, 108 (48), pp. 19365–19370.
- Hechinger, S., Wernike, K. & Beer, M. (2014) Single Immunization with an Inactivated Vaccine Protects Sheep from Schmallenberg Virus Infection. *Veterinary Research*, 45, p. 79.
- Hellert, J., Aebischer, A., Wernike, K., Haouz, A., Brocchi, E., Reiche, S., Guardado-Calvo, P., Beer, M. & Rey, F. A. (2019) Orthobunyavirus Spike Architecture and Recognition by Neutralizing Antibodies. *Nature Communications*, 10.
- Henderson, R. (1995) The Potential and Limitations of Neutrons, Electrons and X-Rays for Atomic Resolution Microscopy of Unstained Biological Molecules. *Quarterly Reviews of Biophysics*, 28 (2), pp. 171–193.
- Hepojoki, J., Strandin, T., Wang, H., Vapalahti, O., Vaheri, A. & Lankinen, H. (2010) Cytoplasmic Tails of Hantavirus Glycoproteins Interact with the Nucleocapsid Protein. *Journal of General Virology*, 91, pp. 2341–2350.
- Herzik Jr, M. A., Wu, M. & Lander, G. C. (2017) Achieving better-than-3-Å Resolution by single-Particle cryo-EM at 200 keV. *Nature Methods*, 14 (11), pp. 1075–1078.
- Heymann, J. B., Chagoyen, M. & Belnap, D. M. (2005) Common Conventions for Interchange and Archiving of Three-Dimensional Electron Microscopy Information in Structural Biology. *Journal of Structural Biology*, 151, pp. 196–207.
- Hoffmann, B., Scheuch, M., Höper, D., Jungblut, R., Holsteg, M., Schirrmeier, H., Eschbaumer, M., Goller, K. V., Wernike, K., Fischer, M., Breithaupt, A., Mettenleiter, T. C. & Beer, M. (2012) Novel Orthobunyavirus in Cattle, Europe, 2011. *Emerging Infectious Diseases*, 18 (3), pp. 469–472.
- Hofmann, H., Li, X., Zhang, X., Liu, W., Kühl, A., Kaup, F., Soldan, S. S., González-Scarano, F., Weber, F., He, Y. & Pöhlmann, S. (2013) Severe Fever with Thrombocytopenia Virus Glycoproteins Are Targeted by Neutralizing Antibodies and Can Use DC-SIGN as a Receptor for pH-Dependent Entry into Human and Animal Cell Lines. *Journal of Virology*, 87 (8), pp. 4384–4394.
- Holm, T., Kopicki, J.-D., Busch, C., Olschewski, S., Rosenthal, M., Uetrecht, C., Günther, S. & Reindl, S. (2018) Biochemical and Structural Studies Reveal Differences and Commonalities among Cap-Snatching Endonucleases from Segmented Negative-Strand RNA Viruses. *Journal of Biological Chemistry*, 293 (51), pp. 19686–19698.
- Hover, S., Foster, B., Fontana, J., Kohl, A., Goldstein, S. A. N., Barr, J. N. & Mankouri, J. (2018) Bunyavirus Requirement for Endosomal K<sup>+</sup> Reveals New Roles of Cellular Ion Channels during Infection. *PLoS Pathogens*, 14 (1), p. e1006845.
- Howley, P. M., Knipe, D. M., Whelan, S. (2020). *Fields virology: Emerging Diseases*. Philadelphia: Lippincott Williams & Wilkins.
- Hubálek, Z. (2008) Mosquito-Borne Viruses in Europe. *Parasitology Research*, 103, pp. S29–S43.

Huiskonen, J. T., Hepojoki, J., Laurinmäki, P., Vaheri, A., Lankinen, H., Butcher, S. J. & Grünewald, K. (2010) Electron Cryotomography of Tula Hantavirus Suggests a Unique Assembly Paradigm for Enveloped Viruses. *Journal of Virology*, 84 (10), pp. 4889–4897.

Huiskonen, J. T., Överby, A. K., Weber, F. & Grünewald, K. (2009) Electron Cryo-Microscopy and Single-Particle Averaging of Rift Valley Fever Virus: Evidence for G<sub>N</sub>-G<sub>C</sub> Glycoprotein Heterodimers. *Journal of Virology*, 83 (8), pp. 3762–3769.

Jacoby, D. R., Cooke, C., Prabakaran, I., Boland, J., Nathanson, N. & Gonzalez-Scarano, F. (1993) Expression of the La Crosse M Segment Proteins in a Recombinant Vaccinia Expression System Mediates PH-Dependent Cellular Fusion. *Virology*, 193, pp. 993–996.

Jeeva, S., Cheng, E., Ganaie, S. S. & Mir, M. A. (2017) Crimean-Congo Hemorrhagic Fever Virus Nucleocapsid Protein Augments mRNA Translation. *Journal of Virology*, 91 (15), pp. e00636-17.

Jiang, X., Huang, Q., Wang, W., Dong, H., Ly, H., Liang, Y. & Dong, C. (2013) Structures of Arenaviral Nucleoproteins with Triphosphate dsRNA Reveal a Unique Mechanism of Immune Suppression. *Journal of Biological Chemistry*, 288 (23), pp. 16949–1659.

Jiao, L., Ouyang, S., Liang, M., Niu, F., Shaw, N., Wu, W., Ding, W., Jin, C., Peng, Y., Zhu, Y., Zhang, F., Wang, T., Li, C., Zuo, X., Luan, C.-H., Li, D. & Liu, Z.-J. (2013) Structure of Severe Fever with Thrombocytopenia Syndrome Virus Nucleocapsid Protein in Complex with Suramin Reveals Therapeutic Potential. *Journal of Virology*, 87 (12), pp. 6829–6839.

Jin, H. & Elliott, R. M. (1993) Characterization of Bunyamwera Virus S RNA That Is Transcribed and Replicated by the L Protein Expressed from Recombinant Vaccinia Virus. *Journal of Virology*, 67 (3), pp. 1396–1404.

Jorba, N., Area, E. & Ortín, J. (2008) Oligomerization of the Influenza Virus Polymerase Complex *in Vivo*. *Journal of General Virology*, 89, pp. 520–524.

Jorba, N., Coloma, R. & Ortín, J. (2009) Genetic *trans*-Complementation Establishes a New Model for Influenza Virus RNA Transcription and Replication. *PLoS Pathogens*, 5 (5), p. e1000462.

Kascsak, R. J. & Lyons, M. J. (1977) Bunyamwera Virus I. The Molecular Complexity of the Virion RNA. *Virology*, 82, pp. 37–47.

Kaukinen, P., Kumar, V., Tulimäki, K., Engelhardt, P., Vaheri, A. & Plyusnin, A. (2004) Oligomerization of Hantavirus N Protein: C-Terminal  $\alpha$ -Helices Interact To Form a Shared Hydrophobic Space. *Journal of Virology*, 78 (24), pp. 13669–13677.

Kim, G., Azmi, L., Jang, S., Jung, T., Hebert, H., Roe, A. J., Byron, O. & Song, J.-J. (2019) Aldehyde-Alcohol Dehydrogenase Forms a High-Order Spirosome Architecture Critical for Its Activity. *Nature Communications*, 10, p. 4527.

Kim, Y.-H., Kweon, C.-H., Tark, D.-S., Lim, S. I., Yang, D.-K., Hyun, B.-H., Song, J.-Y., Hur, W. & Park, S. C. (2011) Development of Inactivated Trivalent Vaccine for the Teratogenic Aino, Akabane and Chuzan Viruses. *Biologicals*, 39, pp. 152–157.

- Kirchdoerfer, R. N., Saphire, E. O. & Ward, A. B. (2019) Cryo-EM Structure of the Ebola Virus Nucleoprotein–RNA Complex. *Acta Crystallographica Section F: Structural Biology Communications*, 75, pp. 340–347.
- Koster, A. J., Grimm, R., Typke, D., Hegerl, R., Stoschek, A., Walz, J. & Baumeister, W. (1997) Perspectives of Molecular and Cellular Electron Tomography. *Journal of Structural Biology*, 120, pp. 276–308.
- Kranzusch, P. J., Schenk, A. D., Rahmeh, A. A., Radoshitzky, S. R., Bavari, S., Walz, T. & Whelan, S. P. J. (2010) Assembly of a Functional Machupo Virus Polymerase Complex. *Proceedings of the National Academy of Sciences of the United States of America*, 107 (46), pp. 20069–20074.
- Kremer, J. R., Mastronarde, D. N. & McIntosh, J. R. (1996) Computer Visualization of Three-Dimensional Image Data Using IMOD. *Journal of Structural Biology*, 116, pp. 71–76.
- Kühlbrandt, W. (2014) The Resolution Revolution. *Science*, 343 (6178), pp. 1443–1444.
- Kurogi, H., Inaba, Y., Goto, Y., Miura, Y., Takahashi, H., Sato, K., Omori, T. & Matumoto, M. (1975) Serologic Evidence for Etiologic Role of Akabane Virus in Epizootic Abortion-Arthrogryposis-Hydranencephaly in Cattle in Japan, 1972-1974. *Archives of Virology*, 47, pp. 71–83.
- Lappin, D. F., Nakitare, G. W., Palfreyman, J. W. & Elliott, R. M. (1994) Localization of Bunyamwera Bunyavirus G1 Glycoprotein to the Golgi Requires Association with G2 but Not with NSm. *Journal of General Virology*, 75, pp. 3441–3451.
- Lees, J. F., Pringle, C. R. & Elliott, R. M. (1986) Nucleotide Sequence of the Bunyamwera Virus M RNA Segment: Conservation of Structural Features in the Bunyavirus Glycoprotein Gene Product. *Virology*, 148, pp. 1–14.
- Li, B., Wang, Q., Pan, X., Fernández de Castro, I., Sun, Y., Guo, Y., Tao, X., Risco, C., Sui, S.-F. & Lou, Z. (2013) Bunyamwera Virus Possesses a Distinct Nucleocapsid Protein to Facilitate Genome Encapsidation. *Proceedings of the National Academy of Sciences of the United States of America*, 110 (22), pp. 9048–9053.
- Li, S., Sun, Z., Pryce, R., Parsy, M.-L., Fehling, S. K., Schlie, K., Siebert, C. A., Garten, W., Bowden, T. A., Strecker, T. & Huiskonen, J. T. (2016) Acidic PH-Induced Conformations and LAMP1 Binding of the Lassa Virus Glycoprotein Spike. *PLoS Pathogens*, 12 (2), p. e1005418.
- Liang, B., Li, Z., Jenni, S., Rahmeh, A. A., Morin, B. M., Grant, T., Grigorieff, N., Harrison, S. C. & Whelan, S. P. J. (2015) Structure of the L Protein of Vesicular Stomatitis Virus from Electron Cryomicroscopy. *Cell*, 162 (2), pp. 314–327.
- Lievaart-Peterson, K., Lutikholt, S., Peperkamp, K., Brom, R. Van den & Vellema, P. (2015) Schmallenberg Disease in Sheep or Goats: Past, Present and Future. *Veterinary Microbiology*, 181, pp. 147–153.
- Liu-Helmersson, J., Quam, M., Wilder-Smith, A., Stenlund, H., Ebi, K., Massad, E. & Rocklöv, J. (2016) Climate Change and Aedes Vectors: 21st Century Projections for Dengue Transmission in Europe. *EBioMedicine*, 7, pp. 267–277.
- López-Montero, N. & Risco, C. (2011) Self-Protection and Survival of Arbovirus-Infected Mosquito Cells. *Cellular Microbiology*, 13 (2), pp. 300–315.

- Lowen, A. C., Noonan, C., McLees, A. & Elliott, R. M. (2004) Efficient Bunyavirus Rescue from Cloned CDNA. *Virology*, 330, pp. 493–500.
- Major, L., Linn, M. La, Slade, R. W., Schroder, W. A., Hyatt, A. D., Gardner, J., Cowley, J. & Suhrbier, A. (2009) Ticks Associated with Macquarie Island Penguins Carry Arboviruses from Four Genera. *PLoS ONE*, 4 (2), p. e4375.
- Martín-Benito, J., Area, E., Ortega, J., Llorca, O., Valpuesta, J. M., Carrascosa, J. L. & Ortín, J. (2001) Three-Dimensional Reconstruction of a Recombinant Influenza Virus Ribonucleoprotein Particle. *EMBO Reports*, 2 (4), pp. 313–317.
- Mattei, S., Tan, A., Glass, B., Müller, B., Kräusslich, H.-G. & Briggs, J. A. G. (2018) High-Resolution Structures of HIV-1 Gag Cleavage Mutants Determine Structural Switch for Virus Maturation. *Proceedings of the National Academy of Sciences of the United States of America*, 115 (40), pp. E9401–E9410.
- McMullan, G., Chen, S., Henderson, R. & Faruqi, A. R. (2009) Detective Quantum Efficiency of Electron Area Detectors in Electron Microscopy. *Ultramicroscopy*, 109 (9), pp. 1126–1143.
- Melin, L., Persson, R., Andersson, A., Bergström, A., Rönholm, R. & Pettersson, R. F. (1995) The Membrane Glycoprotein G1 of Uukuniemi Virus Contains a Signal for Localization to the Golgi Complex. *Virus Research*, 36, pp. 49–66.
- Merk, A., Bartesaghi, A., Banerjee, S., Falconieri, V., Rao, P., Davis, M. I., Pragani, R., Boxer, M. B., Earl, L. A., Milne, J. L. S. & Subramaniam, S. (2016) Breaking Cryo-EM Resolution Barriers to Facilitate Drug Discovery. *Cell*, 165 (7), pp. 1698–1707.
- Moeller, A., Kirchdoerfer, R. N., Potter, C. S., Carragher, B. & Wilson, I. A. (2012) Organization of the Influenza Virus Replication Machinery. *Science*, 338 (6114), pp. 1631–1634.
- Mohl, B.-P. & Barr, J. N. (2009) Investigating the Specificity and Stoichiometry of RNA Binding by the Nucleocapsid Protein of Bunyamwera Virus. *RNA*, 15, pp. 391–399.
- Monteiro, J. T., Schön, K., Ebbecke, T., Goethe, R., Ruland, J., Baumgärtner, W., Becker, S. C. & Lepenies, B. (2019) The CARD9-Associated C-Type Lectin, Mincle, Recognizes La Crosse Virus (LACV) but Plays a Limited Role in Early Antiviral Responses against LACV. *Viruses*, 11 (3), p. 303.
- Morin, B., Coutard, B., Lelke, M., Ferron, F., Kerber, R., Jamal, S., Frangeul, A., Baronti, C., Charrel, R., Lamballerie, X. De, Vonrhein, C., Lescar, J., Bricogne, G., Günther, S. & Canard, B. (2010) The N-Terminal Domain of the Arenavirus L Protein Is an RNA Endonuclease Essential in mRNA Transcription. *PLoS Pathogens*, 6 (9), p. e1001038.
- Murillo, J. L., Cabral, A. D., Uehara, M., Silva, V. M. da, Santos, J. V. dos, Muniz, J. R. C., Estrozi, L. F., Fenel, D., Garcia, W. & Sperança, M. A. (2018) Nucleoprotein from the Unique Human Infecting *Orthobunyavirus* of Simbu Serogroup (*Oropouche Virus*) Forms Higher Order Oligomers in Complex with Nucleic Acids *in Vitro*. *Amino Acids*, 50 (6), pp. 711–721.
- Ng, A. K.-L., Lam, M. K.-H., Zhang, H., Liu, J., Au, S. W.-N., Chan, P. K.-S., Wang, J. & Shaw, P.-C. (2012) Structural Basis for RNA Binding and Homo-Oligomer Formation by Influenza B Virus Nucleoprotein. *Journal of Virology*, 86 (12), pp. 6758–6767.

Nguyen, N. L., Zhao, G., Hull, R., Shelly, M. A., Wong, S. J., Wu, G., George, K. St., Wang, D. & Menegus, M. A. (2013) Cache Valley Virus in a Patient Diagnosed with Aseptic Meningitis. *Journal of Clinical Microbiology*, 51 (6), pp. 1966–1969.

Nicastro, D., Schwartz, C., Pierson, J., Gaudette, R., Porter, M. E. & McIntosh, J. R. (2006) The Molecular Architecture of Axonemes Revealed by Cryoelectron Tomography. *Science*, 313, pp. 944–948.

Niu, F., Shaw, N., Wang, Y. E., Jiao, L., Ding, W., Li, X., Zhu, P., Upur, H., Ouyang, S., Cheng, G. & Liu, Z.-J. (2013) Structure of the Leanyer Orthobunyavirus Nucleoprotein–RNA Complex Reveals Unique Architecture for RNA Encapsidation. *Proceedings of the National Academy of Sciences of the United States of America*, 110 (22), pp. 9054–9059.

Novoa, R. R., Calderita, G., Cabezas, P., Elliott, R. M. & Risco, C. (2005) Key Golgi Factors for Structural and Functional Maturation of Bunyamwera Virus. *Journal of Virology*, 79 (17), pp. 10852–10863.

Objieski, J. F., Bishop, D. H. L., Palmer, E. L. & Murphy, F. A. (1976) Segmented Genome and Nucleocapsid of La Crosse Virus. *Journal of Virology*, 20 (3), pp. 664–675.

Olal, D. & Daumke, O. (2016) Structure of the Hantavirus Nucleoprotein Provides Insights into the Mechanism of RNA Encapsidation. *Cell Reports*, 14, pp. 2092–2099.

Olal, D., Dick, A., Woods, V. L., Liu, T., Li, S., Devignot, S., Weber, F., Sapphire, E. O., Daumke, O. & Delbr, M. (2014) Structural Insights into RNA Encapsidation and Helical Assembly of the Toscana Virus Nucleoprotein. *Nucleic Acids Research*, 42 (9), pp. 6025–6037.

Orlova, E. V. & Saibil, H. R. (2011) Structural Analysis of Macromolecular Assemblies by Electron Microscopy. *Chemical Reviews*, 111, pp. 7710–7748.

Överby, A. K., Pettersson, R. F., Grünwald, K. & Huisken, J. T. (2008) Insights into Bunyavirus Architecture from Electron Cryotomography of Uukuniemi Virus. *Proceedings of the National Academy of Sciences of the United States of America*, 105 (7), pp. 2375–2379.

Överby, A. K., Pettersson, R. F. & Neve, E. P. A. (2007) The Glycoprotein Cytoplasmic Tail of Uukuniemi Virus (*Bunyaviridae*) Interacts with Ribonucleoproteins and Is Critical for Genome Packaging. *Journal of Virology*, 81 (7), pp. 3198–3205.

Patterson, J. L., Holloway, B. & Kolakofsky, D. (1984) La Crosse Virions Contain a Primer-Stimulated RNA Polymerase and a Methylated Cap-Dependent Endonuclease. *Journal of Virology*, 52 (1), pp. 215–222.

Patterson, J. L. & Kolakofsky, D. (1984) Characterization of La Crosse Virus Small-Genome Transcripts. *Journal of Virology*, 49 (3), pp. 680–685.

Paul, D. & Bartenschlager, R. (2015) Flaviviridae Replication Organelles: Oh, What a Tangled Web We Weave. *Annual Review of Virology*, 2, pp. 289–310.

Peng, R., Xu, X., Jing, J., Wang, M., Peng, Q., Liu, S., Wu, Y., Bao, X., Wang, P., Qi, J., Gao, G. F. & Shi, Y. (2020) Structural Insight into Arenavirus Replication Machinery. *Nature*, 579, pp. 615–619.

- Pettersen, E. F., Goddard, T. D., Huang, C. C., Couch, G. S., Greenblatt, D. M., Meng, E. C. & Ferrin, T. E. (2004) UCSF Chimera—A Visualization System for Exploratory Research and Analysis. *Journal of Computational Chemistry*, 25 (13), pp. 1605–1612.
- Pettersson, R. F. & Bonsdorff, C.-H. Von (1975) Ribonucleoproteins of Uukuniemi Virus Are Circular. *Journal of Virology*, 15 (2), pp. 386–392.
- Pflug, A., Guilligay, D., Reich, S. & Cusack, S. (2014) Structure of Influenza A Polymerase Bound to the Viral RNA Promoter. *Nature*, 516 (7531), pp. 355–360.
- Piper, M. E., Sorenson, D. R. & Gerrard, S. R. (2011) Efficient Cellular Release of Rift Valley Fever Virus Requires Genomic RNA. *PLoS ONE*, 6 (3), p. e18070.
- Plotch, S. J., Bouloy, M., Ulmanen, I. & Krug, R. M. (1981) A Unique Cap(m<sup>7</sup>GpppXm)-Dependent Influenza Virion Endonuclease Cleaves Capped RNAs to Generate the Primers That Initiate Viral RNA Transcription. *Cell*, 23, pp. 847–858.
- Pons, M. W., Schulze, I. T., Hirst, G. K. & Hauser, R. (1969) Isolation and Characterization of the Ribonucleoprotein of Influenza Virus. *Virology*, 39, pp. 250–259.
- Punch, E. K., Hover, S., Blest, H. T. W., Fuller, J., Hewson, R., Fontana, J., Mankouri, J. & Barr, J. N. (2018) Potassium Is a Trigger for Conformational Change in the Fusion Spike of an Enveloped RNA Virus. *Journal of Biological Chemistry*, 293 (26), pp. 9937–9944.
- Pythoud, C., Rodrigo, W. W. S. I., Pasqual, G., Rothenberger, S., Martínez-Sobrido, L., La Torre, J. C. De & Kunz, S. (2012) Arenavirus Nucleoprotein Targets Interferon Regulatory Factor-Activating Kinase IKK. *Journal of Virology*, 86 (15), pp. 7728–7738.
- Qi, X., Lan, S., Wang, W., Schelde, L. M., Dong, H., Wallat, G. D., Ly, H., Liang, Y. & Dong, C. (2010) Cap Binding and Immune Evasion Revealed by Lassa Nucleoprotein Structure. *Nature*, 468 (7325), pp. 779–783.
- Raju, R. & Kolakofsky, D. (1987) Translational Requirement of La Crosse Virus S-MRNA Synthesis: In Vivo Studies. *Journal of Virology*, 61 (1), pp. 96–103.
- Ravkov, E. V., Nichol, S. T. & Compans, R. W. (1997) Polarized Entry and Release in Epithelial Cells of Black Creek Canal Virus, a New World Hantavirus. *Journal of Virology*, 71 (2), pp. 1147–1154.
- Raymond, D. D., Piper, M. E., Gerrard, S. R., Skiniotis, G. & Smith, J. L. (2012) Phleboviruses Encapsidate Their Genomes by Sequestering RNA Bases. *Proceedings of the National Academy of Sciences of the United States of America*, 109 (47), pp. 19208–19213.
- Raymond, D. D., Piper, M. E., Gerrard, S. R. & Smith, J. L. (2010) Structure of the Rift Valley Fever Virus Nucleocapsid Protein Reveals Another Architecture for RNA Encapsidation. *Proceedings of the National Academy of Sciences of the United States of America*, 107 (26), pp. 11769–11774.
- Reguera, J., Gerlach, P. & Cusack, S. (2016) Towards a Structural Understanding of RNA Synthesis by Negative Strand RNA Viral Polymerases. *Current Opinion in Structural Biology*, 36, pp. 75–84.

- Reguera, J., Gerlach, P., Rosenthal, M., Gaudon, S., Coscia, F., Günther, S. & Cusack, S. (2016) Comparative Structural and Functional Analysis of Bunyavirus and Arenavirus Cap-Snatching Endonucleases. *PLoS Pathogens*, 12 (6), p. e1005636.
- Reguera, J., Malet, H., Weber, F. & Cusack, S. (2013) Structural Basis for Encapsidation of Genomic RNA by La Crosse Orthobunyavirus Nucleoprotein. *Proceedings of the National Academy of Sciences of the United States of America*, 110 (18), pp. 7246–7251.
- Reguera, J., Weber, F. & Cusack, S. (2010) *Bunyaviridae* RNA Polymerases (L-Protein) Have an N-Terminal, Influenza-Like Endonuclease Domain, Essential for Viral Cap-Dependent Transcription. *PLoS Pathogens*, 6 (9), p. e1001101.
- Reich, S., Guilligay, D., Pflug, A., Malet, H., Berger, I., Crépin, T., Hart, D., Lunardi, T., Nanao, M., Ruigrok, R. W. H. & Cusack, S. (2014) Structural Insight into Cap-Snatching and RNA Synthesis by Influenza Polymerase. *Nature*, 516 (7531), pp. 361–366.
- Reynard, S., Russier, M., Fizet, A., Carnec, X. & Baize, S. (2014) Exonuclease Domain of the Lassa Virus Nucleoprotein Is Critical To Avoid RIG-I Signaling and To Inhibit the Innate Immune Response. *Journal of Virology*, 88 (23), pp. 13923–13927.
- Ribeiro, D., Borst, J. W., Goldbach, R. & Kormelink, R. (2009) Tomato Spotted Wilt Virus Nucleocapsid Protein Interacts with Both Viral Glycoproteins Gn and Gc *in Planta*. *Virology*, 383, pp. 121–130.
- Roberts, A., Rossier, C., Kolakofsky, D., Nathanson, N. & Gonzalez-Scarano, F. (1995) Completion of the La Crosse Virus Genome Sequence and Genetic Comparisons of the L Proteins of the Bunyaviridae. *Virology*, 206 (1), pp. 742–745.
- Rudolph, M. G., Kraus, I., Dickmanns, A., Eickmann, M., Garten, W. & Ficner, R. (2003) Crystal Structure of the Borna Disease Virus Nucleoprotein. *Structure*, 11, pp. 1219–1226.
- Russier, M., Reynard, S., Carnec, X. & Baize, S. (2014) The Exonuclease Domain of Lassa Virus Nucleoprotein Is Involved in Antigen-Presenting-Cell-Mediated NK Cell Responses. *Journal of Virology*, 88 (23), pp. 13811–13820.
- Sachse, C., Chen, J. Z., Coureux, P.-D., Stroupe, M. E., Fändrich, M. & Grigorieff, N. (2007) High-Resolution Electron Microscopy of Helical Specimens: A Fresh Look at Tobacco Mosaic Virus. *Journal of Molecular Biology*, 371, pp. 812–835.
- Sakkas, H., Bozidis, P., Franks, A. & Papadopoulou, C. (2018) Oropouche Fever: A Review. *Viruses*, 10 (4), p. 175.
- Salanueva, I. J., Novoa, R. R., Cabezas, P., López-Iglesias, C., Carrascosa, J. L., Elliott, R. M. & Risco, C. (2003) Polymorphism and Structural Maturation of Bunyamwera Virus in Golgi and Post-Golgi Compartments. *Journal of Virology*, 77 (2), pp. 1368–1381.
- Santos, R. I. M., Rodrigues, A. H., Silva, M. L., Mortara, R. A., Rossi, M. A., Jamur, M. C., Oliver, C. & Arruda, E. (2008) Oropouche Virus Entry into HeLa Cells Involves Clathrin and Requires Endosomal Acidification. *Virus Research*, 138, pp. 139–143.
- Scarff, C. A., Fuller, M. J. G., Thompson, R. F. & Iadanza, M. G. (2018) Variations on Negative Stain Electron Microscopy Methods: Tools for Tackling Challenging Systems. *Journal of Visualized Experiments*, 132, p. e57199.

- Schindelin, J., Arganda-Carreras, I., Frise, E., Kaynig, V., Longair, M., Pietzsch, T., Preibisch, S., Rueden, C., Saalfeld, S., Schmid, B., Tinevez, J.-Y., White, D. J., Hartenstein, V., Eliceiri, K., Tomancak, P. & Cardona, A. (2012) Fiji: An Open-Source Platform for Biological-Image Analysis. *Nature Methods*, 9 (7), pp. 676–682.
- Serna Martin, I., Hengrung, N., Renner, M., Sharps, J., Martínez-Alonso, M., Masiulis, S., Grimes, J. M. & Fodor, E. (2018) A Mechanism for the Activation of the Influenza Virus Transcriptase. *Molecular Cell*, 70, pp. 1101–1110.
- Shepherd, D. A., Ariza, A., Edwards, T. A., Barr, J. N., Stonehouse, N. J. & Ashcroft, A. E. (2014) Probing Bunyavirus N Protein Oligomerisation Using Mass Spectrometry. *Rapid Communications in Mass Spectrometry*, 28, pp. 793–800.
- Sherman, M. B., Freiberg, A. N., Holbrook, M. R. & Watowich, S. J. (2009) Single-Particle Cryo-Electron Microscopy of Rift Valley Fever Virus. *Virology*, 387 (1), pp. 11–15.
- Shi, X., Botting, C. H., Li, P., Niglas, M., Brennan, B., Shirran, S. L., Szemiel, A. M. & Elliott, R. M. (2016) Bunyamwera Orthobunyavirus Glycoprotein Precursor Is Processed by Cellular Signal Peptidase and Signal Peptide Peptidase. *Proceedings of the National Academy of Sciences of the United States of America*, 113 (31), pp. 8825–8830.
- Shi, X., Kohl, A., Léonard, V. H. J., Li, P., McLees, A. & Elliott, R. M. (2006) Requirement of the N-Terminal Region of Orthobunyavirus Nonstructural Protein NSm for Virus Assembly and Morphogenesis. *Journal of Virology*, 80 (16), pp. 8089–8099.
- Shi, X., Lappin, D. F. & Elliott, R. M. (2004) Mapping the Golgi Targeting and Retention Signal of Bunyamwera Virus Glycoproteins. *Journal of Virology*, 78 (19), pp. 10793–10802.
- Smithburn, K. C., Haddow, A. J. & Mahaffy, A. F. (1946) A Neurotropic Virus Isolated from *Aedes* Mosquitoes Caught in the Semliki Forest. *The American Journal of Tropical Medicine and Hygiene*, s1-26 (2), pp. 189–208.
- Snippe, M., Willem Borst, J., Goldbach, R. & Kormelink, R. (2007) Tomato Spotted Wilt Virus Gc and N Proteins Interact *in Vivo*. *Virology*, 357, pp. 115–123.
- Strandin, T., Hepojoki, J. & Vaheri, A. (2013) Cytoplasmic Tails of Bunyavirus Gn Glycoproteins—Could They Act as Matrix Protein Surrogates? *Virology*, 437, pp. 73–80.
- Subramaniam, S., Bartesaghi, A., Liu, J., Bennett, A. E. & Sougrat, R. (2007) Electron Tomography of Viruses. *Current Opinion in Structural Biology*, 17, pp. 596–602.
- Sugita, Y., Matsunami, H., Kawaoka, Y., Noda, T. & Wolf, M. (2018) Cryo-EM Structure of the Ebola Virus Nucleoprotein–RNA Complex at 3.6 Å Resolution. *Nature*, 563 (7729), pp. 137–140.
- Sun, Y., Li, J., Gao, G. F., Tien, P. & Liu, W. (2018) Bunyavirales Ribonucleoproteins: The Viral Replication and Transcription Machinery. *Critical Reviews in Microbiology*, 44 (5), pp. 522–540.
- Surtees, R., Ariza, A., Punch, E. K., Trinh, C. H., Dowall, S. D., Hewson, R., Hiscox, J. A., Barr, J. N. & Edwards, T. A. (2015) The Crystal Structure of the Hazara Virus Nucleocapsid Protein. *BMC Structural Biology*, 15 (24).

- Tan, Y. Z., Aiyer, S., Mietzsch, M., Hull, J. A., McKenna, R., Grieger, J., Samulski, R. J., Baker, T. S., Agbandje-McKenna, M. & Lyumkis, D. (2018) Sub-2 Å Ewald Curvature Corrected Structure of an AAV2 Capsid Variant. *Nature Communications*, 9 (1), p. 3628.
- Tawar, R. G., Duquerroy, S., Vorrhein, C., Varela, P. F., Damier-Piolle, L., Castagne, N., MacLellan, K., Bedouelle, H., Bricogne, G., Bhella, D., Eléouët, J.-F. & Rey, F. A. (2009) Crystal Structure of a Nucleocapsid-Like Nucleoprotein-RNA Complex of Respiratory Syncytial Virus. *Science*, 326 (5957), pp. 1279–1283.
- The Approved List of Biological Agents: Advisory Committee on Dangerous Pathogens* [Online]. Available from: <<https://www.hse.gov.uk/pubns/misc208.pdf>>.
- Thompson, R. F., Iadanza, M. G., Hesketh, E. L., Rawson, S. & Ranson, N. A. (2019) Collection, Pre-Processing and on-the-Fly Analysis of Data for High-Resolution, Single-Particle Cryo-Electron Microscopy. *Nature Protocols*, 14, pp. 100–118.
- Thompson, R. F., Walker, M., Siebert, C. A., Muench, S. P. & Ranson, N. A. (2016) An Introduction to Sample Preparation and Imaging by Cryo-Electron Microscopy for Structural Biology. *Methods*, 100, pp. 3–15.
- Thompson, W. H., Kalfayan, B. & Anslow, R. O. (1965) Isolation of California Encephalitis Group Virus from a Fatal Human Illness. *American Journal of Epidemiology*, 81 (2), pp. 245–253.
- Wallat, G. D., Huang, Q., Wang, W., Dong, H., Ly, H., Liang, Y. & Dong, C. (2014) High-Resolution Structure of the N-Terminal Endonuclease Domain of the Lassa Virus L Polymerase in Complex with Magnesium Ions. *PLoS ONE*, 9 (2), p. e87577.
- Wan, W., Kolesnikova, L., Clarke, M., Koehler, A., Noda, T., Becker, S. & Briggs, J. A. G. (2017) Structure and Assembly of the Ebola Virus Nucleocapsid. *Nature*, 551 (7680), pp. 394–397.
- Wang, X., Li, B., Guo, Y., Shen, S., Zhao, L., Zhang, P., Sun, Y., Sui, S.-F., Deng, F. & Lou, Z. (2016) Molecular Basis for the Formation of Ribonucleoprotein Complex of Crimean-Congo Hemorrhagic Fever Virus. *Journal of Structural Biology*, 196, pp. 455–465.
- Wang, Y., Dutta, S., Karlberg, H., Devignot, S., Weber, F., Hao, Q., Tan, Y. J., Mirazimi, A. & Kotaka, M. (2012) Structure of Crimean-Congo Hemorrhagic Fever Virus Nucleoprotein: Superhelical Homo-Oligomers and the Role of Caspase-3 Cleavage. *Journal of Virology*, 86 (22), pp. 12294–12303.
- Wernike, K., Nikolin, V. M., Hechinger, S., Hoffmann, B. & Beer, M. (2013) Inactivated Schmallenberg Virus Prototype Vaccines. *Vaccine*, 31, pp. 3558–3563.
- West, B. R., Hastie, K. M. & Saphire, E. O. (2014) Structure of the LCMV Nucleoprotein Provides a Template for Understanding Arenavirus Replication and Immunosuppression. *Acta Crystallographica Section D: Structural Biology*, 70, pp. 1764–1769.
- Wichgers Schreur, P. J. & Kortekaas, J. (2016) Single-Molecule FISH Reveals Non-Selective Packaging of Rift Valley Fever Virus Genome Segments. *PLoS Pathogens*, 12 (8), p. e1005800.
- Willensky, S., Bar-Rogovsky, H., Bignon, E. A., Tischler, N. D., Modis, Y. & Dessau, M. (2016) Crystal Structure of Glycoprotein C from a Hantavirus in the Post-Fusion Conformation. *PLoS Pathogens*, 12 (10), pp. 1–25.

- Wolf, Y. I., Kazlauskas, D., Iranzo, J., Lucía-Sanz, A., Kuhn, J. H., Krupovic, M., Dolja, V. V. & Koonin, E. V. (2018) Origins and Evolution of the Global RNA Virome. *mBio*, 9 (6), pp. e02329-18.
- Yanase, T., Kato, T., Aizawa, M., Shuto, Y., Shirafuji, H., Yamakawa, M. & Tsuda, T. (2012) Genetic Reassortment between Sathuperi and Shamonda Viruses of the Genus *Orthobunyavirus* in Nature: Implications for Their Genetic Relationship to Schmallenberg Virus. *Archives of Virology*, 157 (8), pp. 1611–1616.
- Ye, Q., Krug, R. M. & Tao, Y. J. (2006) The Mechanism by Which Influenza A Virus Nucleoprotein Forms Oligomers and Binds RNA. *Nature*, 444 (7122), pp. 1078–1082.
- York, A., Hengrung, N., Vreede, F. T., Huiskonen, J. T. & Fodor, E. (2013) Isolation and Characterization of the Positive-Sense Replicative Intermediate of a Negative-Strand RNA Virus. *Proceedings of the National Academy of Sciences of the United States of America*, 110 (45), pp. E4238–E4245.
- Yuan, P., Bartlam, M., Lou, Z., Chen, S., Zhou, J., He, X., Lv, Z., Ge, R., Li, X., Deng, T., Fodor, E., Rao, Z. & Liu, Y. (2009) Crystal Structure of an Avian Influenza Polymerase PA<sub>N</sub> Reveals an Endonuclease Active Site. *Nature*, 458, pp. 909–913.
- Zhang, P. (2019) Advances in Cryo-Electron Tomography and Subtomogram Averaging and Classification. *Current Opinion in Structural Biology*, 58, pp. 249–258.
- Ziegler, C. M., Eisenhauer, P., Bruce, E. A., Beganovic, V., King, B. R., Weir, M. E., Ballif, B. A. & Botten, J. (2016) A Novel Phosphoserine Motif in the LCMV Matrix Protein Z Regulates the Release of Infectious Virus and Defective Interfering Particles. *Journal of General Virology*, 97 (9), pp. 2084–2089.
- Zivanov, J., Nakane, T., Forsberg, B. O., Kimanius, D., Hagen, W. J. H., Lindahl, E. & Scheres, S. H. W. (2018) New Tools for Automated High-Resolution Cryo-EM Structure Determination in RELION-3. *eLife*, 7, p. e42166.